# INTERFEROMETRIC MONITOR FOR GREENHOUSE GASES (IMG)
# PROJECT TECHNICAL REPORT

March 30, 1999
IMG Mission Operation & Verification Committee
CRIEPI

Edited: Hirokazu Kobayashi
Central Research Institute of Electric Power Industry
Komae Research Laboratory
Atmospheric Science Department

2-11-1 Iwato-kita, Komae-shi, Tokyo
E-mail: koba@criepi.denken.or.jp

# IMG MISSION OPERATION & VERIFICATION COMMITTEE MEMBERS IN FY 1998

The IMG mission operation & verification committee in fiscal year 1998 was composed of following members.

Chairman:
T. Ogawa, National Space Development Agency of Japan

Member:
T. Aoki, Meteorological Research Institute
M. Hayashi, NIRE
R. Imasu, National Institute for Resources & Environment (NIRE)
N. Iwakami, Tokyo University
R. Matsuoka, Kokusai Kogyo Co.
N. Nakajima, Japan Resources Observation System Organization (JAROS)
T. Nakajima, Tokyo University
S. Nishinomiya, Central Research Institute of Electric Power Industry (CRIEPI)
H. Shimoda, Tokai Univ. Research & Information Center
M. Suzuki, National Space Development Agency of Japan
S. Taguchi, Earth Remote Sensing Data Analysis Center (ERSDAC)
F. Watanabe, Japan Meteorological Agency
T. Yokota, National Institute for Environmental Studies

Secretariat:
H. Kobayashi, CRIEPI
S. Kadokura, CRIEPI
A. Shimoda, CRIEPI

Observer:
T. Agawa, Ministry of International Trade and Industry (MITI)
M. Inoue, MITI
M. Tomoda, MITI
K. Asakura, CRIEPI

# TABLE OF CONTENTS

# FOREWORD

It was 1988 that under the initiative of the Ministry of International Trade and Industry of Japanese government we started a feasibility study on the instrument to be on board the ADEOS satellite to measure atmospheric greenhouse gases. The nadir observation of greenhouse gases from a satellite seemed to be promising, because greenhouse gases are mainly distributed in the troposphere, the lowest part of the atmosphere. We preferred the nadir observation partly because the limb observation of atmospheric trace gases was planned in several preceding satellite projects of the United States and Europe, although they mainly aimed at measuring stratospheric profiles of trace gases. The thermal infrared is the most suitable spectral region to make the nadir observation to measure atmospheric greenhouse gases, because there are a lot of vibration-rotation absorption lines of greenhouse gas molecules in the thermal infrared.

A high spectral resolution was thought to be necessary for the instrument to detect any spectral signatures of greenhouse gas molecules imbedded in the outgoing thermal infrared atmospheric/terrestrial radiation. Moreover, a high radiometric accuracy is necessary to detect the spatial variation of greenhouse gases, since their variations are expected to be small under atmospheric mixing processes because of their long atmospheric residence time. A Fourier Transform Spectrometer (FTS) using a Michelson interferometer seemed most promising for the optical part of the instrument because of a wide coverage of the spectral region with a high spectral resolution and a large optical throughput. A spacecraft-borne FTS had been already developed by JPL/NASA with respect to low spectral resolution, but there was no preceding spacecraft-borne FTS with high spectral resolution at that time. A FTS of such a high spectral resolution could be fabricated in Japan at that time, but it was applicable only to the laboratory use.

The name of this instrument, “Interferometric Monitor of Greenhouse Gases (IMG)” represents our desire directly. Since monitoring of greenhouse gases is not an easy task, it is said that the name of IMG represents its long-term goal. It was a technical challenge to develop the spacecraft-borne FTS of high spectral resolution and high optical sensitivity. The most significant portion of the instrument was the mirror drive device which employs magnetic bearing and linear motor drive. The adoption of optical aperture of 10 cm diameter was also ambitious to maximize the optical sensitivity, requiring optical flatness of higher precision. We were obliged to use plane mirrors despite a contemporary way of using corner cube mirrors. As a result, a high precision of an order of magnitude of $1x10^{-4}$ degrees was required to the optical alignment of the moving mirror. Finally that precision was attained by adopting a feedback system of alignment to control magnetic bearing using the signal on the interference fringe of a laser light.

We decided the whole optical system to be operated under the satellite ambient temperature. We had to established a careful calibration procedure to eliminate the thermal radiation within the optics. This procedure was developed in our project and implemented in the data analysis system to produce a calibrated spectrum.

In the area of data analysis we have to develop the retrieval procedure to solve an inversion problem in which atmospheric temperature and water vapor and trace gas concentrations are simultaneously calculated from the measured spectrum of outgoing atmospheric radiation. There was no experience in the world at the initiation of the IMG project to treat the retrieval from a spectral radiance of high spectral resolution. We have developed the retrieval algorithm in collaboration with the domestic and international community of investigators. We will present the results in this report, but the results are not satisfactory as compared with those expected from the excellent quality of the IMG spectrum. We, in collaboration with worldwide investigators, will continue the study to refine the retrieval system.

In closing the IMG project, let me emphasize that the objectives set for IMG was scientifically sane and that they were partly demonstrated by the data obtained by IMG. The IMG data are the best spectral quality ever obtained in space with respect to the outgoing atmospheric/terrestrial thermal infrared radiation, and they will remain so for the time being.

Monitoring of greenhouse gases is our final goal. I hope that the study on the data obtained by IMG will be continued and that the development of the follow-on instrument of IMG will be launched.

March 1999

Toshihiro OGAWA

# 1. INTRODUCTION

The global increase of greenhouse gas concentrations is ongoing. It has been determined that human activities are the cause of this phenomenon; nevertheless, our knowledge of the global cyclical mechanisms and the behavior of these gases in the atmosphere is still limited.

Satellite-derived data are essential to obtain a global view of the atmospheric parameters. This requirement has led to the development of the Interferometric Monitor for Greenhouse gases, IMG, by the Japan Resources Observation System Organization (JAROS) under contract to the Ministry of International Trade and Industry (MITI), in 1989. The IMG was placed on board the Advanced Earth Observing Satellite (ADEOS), which was launched by the National Space Development Agency of Japan (NASDA) on Aug. 17, 1996.

The earth's surface and atmosphere emit thermal infrared radiation. It is well known that detailed radiation spectra include absorption and emission signatures of many atmospheric gases. From these detailed spectra, we can obtain the atmospheric concentrations of water vapor and greenhouse gases. A high-resolution spectrometer operating in space can measure variations in the concentrations of these gases, and thus, global and regional distributions of anthropogenic sources can be mapped. This information will be helpful in clarifying the scientific and social aspects of global warming problems and constituent density profiles of $CH_4$, $H_2O$, $N_2O$ and $CO_2$ and the total ozone mixing ratios of the troposphere.

The IMG was the precursor of the high-resolution Fourier Transform Infrared Radiometer (FTIR) based on the Michelson interferometer boarded on the satellite for earth observation. However the IMG sensor ceased operating after 8 months due to satellite failure as a result of the break up of the solar paddle, however, the high-resolution thermal infrared spectra obtained, provided substantial information on various global atmospheric phenomena. This report is intended to summarize the IMG project, and to introduce the IMG sensor characteristics to scientific users along with the data analysis algorithms developed for the IMG data and information system (IMGDIS) to manufacture standardized products.

# 2. COMMENCEMENT OF THE IMG PROJECT

In 1989, considering the global warming program, the MITI decided to consider NASDA's invitation to place sensors in the ADEOS satellite with the IMG. MITI requested a Japanese science team to recommend a feasible sensor to observe the atmospheric greenhouse gases in the troposphere. At that time, the feasible sensing methods considered were (1) correlation spectroscopy (2) grating spectroscopy, and (3) interferometric spectroscopy using a Michelson interferometer. The science team indicated that Interferometric spectroscopy was most suitable for nadir observation, however, it was very difficult to develop a sensor among the three candidates [1].

At the commencement of the IMG feasibility study, only the National Aeronautics and Space Administration (NASA) had experience of FTIR operation in space. They had developed the Infrared interferometric interferometer (IRIS) of the NIMBUS III and IV for earth observations, however, the following FTIR sensors were oriented for planet probing. No previous space FTIR had the high-resolution power of the IMG. It was also considered that nadir observation of the tropospheric constituents was difficult and that observation of greenhouse gases was not so significant at the commencement of the feasibility study of the IMG.

Eventually, MITI adopted the development of a Michelson interferometer. It selected a company developing the sensor, TOSHIBA. JAROS had supervised the sensor development. Subsequently, MITI selected the Central Research Institute of Electric Power Industry (CRIEPI) as a consignor for the IMG software system development. It was the beginning of the challenge.

## 2.1 SCIENTIFIC FEASIBILITY STUDY

The science team estimated the spectral resolution requirement of 0.1 $cm^{-1}$ to fulfill the objectives of the IMG to extract spectral signatures of atmospheric trace gases. An apodized spectral resolution of 0.1 $cm^{-1}$ can be realized by an interferometer with a 10 cm optical path difference, which means the moving mirror travels a distance of 10 cm, and with an assurance of optical alignment within an angle of 0.0001° during the scanning. The sensor hardware development team agreed with this requirement.

Detectability of the deviations in greenhouse gas concentration was another basic requirement for the IMG. Table 1 shows the preliminary analysis carried out by the science team. The table gives possible changes in atmospheric irradiance resulting from the gas concentration changes, and has become the baseline for the radiometric design of the IMG [2]. The hardware design team initiated the study of detector configuration such as detector selection and spectral range partitioning.

The principal aspect of the IMG data analysis is the retrieval process of vertical distributions of greenhouse gas concentrations, atmospheric temperature and humidity. The science team decided to apply the linear simultaneous physical/statistical inversion method [3]. The 0.1 $cm^{-1}$ resolution of atmospheric thermal radiance spectra can separate many rotational lines of various trace gases from each other. From the preliminary analysis of the vertical

Table 2.1.1. Estimated changes in atmospheric irradiance due to the change in mixing ratios of greenhouse gases. Mixing ratio changes are based on the tropospheric difference between northern and southern hemispheres, calculated for the IMG radiometric design.

| species | change in mixing ratio (%) | wavenumber (cm$^{-1}$) | wavelength (mm) | change in radiance (mW/cm$^2$ sr cm$^{-1}$) |
|---|---|---|---|---|
| $CO_2$ | 2 | 718 | 14.0 | 0.03 |
| | | 2320 | 4.3 | 0.00013 |
| $CH_4$ | 8 | 1277 | 7.8 | 0.03 |
| | | 3000 | 3.3 | 0.0002 |
| $N_2O$ | 1 | 1278 | 7.8 | 0.006 |
| | | 2220 | 4.5 | 0.001 |
| CO | 50 | 2180 | 4.6 | 0.04 |
| $O_3$ | 1 | 1010 | 9.9 | 0.02 |
| $H_2O$ | 10 | 1590 | 6.3 | 0.02 |

resolution functions of temperature, using $CO_2$ 4.3 $\mu$m band, the science team indicated that a vertical resolution was 1 - 2 km in the troposphere

According to the analogous analysis, the vertical resolution was better for water vapor in the 5 - 6 $\mu$m band that for the $CO_2$ 4.3 $\mu$m in the lower and middle troposphere because the weighting function distributes in a narrower altitude range for $H_2O$ than for $CO_2$. A preliminary result from a retrieval simulation also exhibits the retrieval error of atmospheric temperature to be ~ 1 K and that of water vapor to be 10 - 20 % in the troposphere. These results appeared satisfactory for the requirements, however, the results showed that there was a tradeoff in the retrieval tolerance between the $CO_2$ retrieval and the temperature retrieval because both may use the same $CO_2$ bands.

## 2.2 HARDWARE DESIGN POLICY

As mentioned previously, the sensor needed to distinguish each absorption line in the atmospheric radiation spectrum with the spectral resolution of 0.1 cm$^{-1}$, and now we are understanding that a 0.1 cm$^{-1}$ resolution can fulfill these requirements [4], [ 5]. When using double-sided interferograms, this 0.1 cm$^{-1}$ resolution can be achieved with the 10 cm optical path difference. This means that the moving mirror must travel 10 cm in a space-level vacuum, and must be operated continuously throughout the expected lifetime of the instrument of greater than three years. Another notable design requirement was that the optical system required a sufficient signal-to-noise ratio (S/N) to allow retrieval of vertical profiles of atmospheric constituents from a spectrum. At that time, there was no commercial FTIR that satisfied the required S/N.

To maximize the optical throughput, the design team decided to adopt a 10-cm-diameter optical aperture. This unprecedented FTIR aperture size was developed using a flat mirror after a feasibility study for some model designs including the corner cube system. The optical system using flat mirrors is very simple, however, special effort was required in the manufacturing of the optical components. For example, with this enhancement in optical design, a large potassium bromide (KBr) beam splitter was prepared. Since KBr is a soft, deliquescent material, a special technique was required to make it sufficiently flat for use as the substrate for the Ge pellicle. A KBr surface flatness of 0.37 $\lambda$ ($\lambda$ is 633 nm which is the wavelength of the HeNe laser), defined as the difference between the peak and valley, was achieved. The design policy for the IMG was to make simple morphologies and enduring components with maximum flexibility derived from the distributed control circuit/processors and ground commands.

## 2.3 HARDWARE DESIGN GOAL

Figure 2.3.1 shows a schematic of the IMG optical system. The heart of the IMG is the magnetically suspended moving mirror system. The design team studied a bearing system for the linearly moving mirror which had an expected lifetime of three years, and selected to develop a magnetic suspension/drive system in order to avoid problems caused by lubrication of the mechanism in vacuum. Since the IMG adopted a pair of moving and fixed flat mirrors for the interferometer, the magnetic suspension system not only had to suspend the 10-cm-diameter mirror attached to the armature, but also enable alignment control in the x- and y-directions of the armature moving in the z-direction to maintain accurate parallelism. The magnetic circuit of the moving mirror armature was composed of an inner yoke, a drive coil fixed to the optics bench, inner permanent magnets at the end of the armature, and the outer armature itself. Eight other suspension

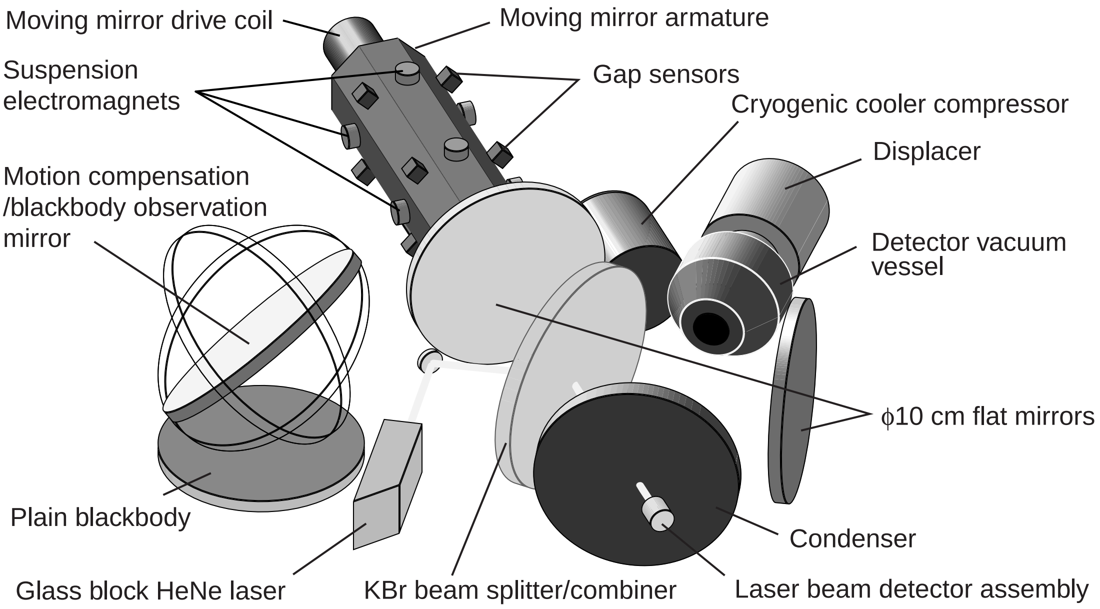

Fig. 2.3.1. Schematic of IMG optical system. The optical aperture of the interferometer is 10 cm in diameter. The interferometer was composed of flat mirrors and a large KBr beam splitter. The moving mirror was suspended magnetically, and the alignment was controlled dynamically using a HeNe laser interferogram detected with four Si detectors. The optical system did not have an intermediate cold field stop.

electromagnets with eight eddy-current-type detection gap sensors were used to suspend and control the armature alignment.

An interferometer requires a reference laser to measure the optical path difference from the number of interference wave fringes counted. The design team adopted a HeNe laser which can maintain wavelength accurately in the absence of external control systems, and the laser-diode pumped yttrium aluminum garnet (YAG) laser was listed as an alternative to the HeNe laser. The YAG system is smaller and consumes less power than the HeNe system, however, the environmental temperature must be very stable to sustain wavelength accuracy for the YAG system.

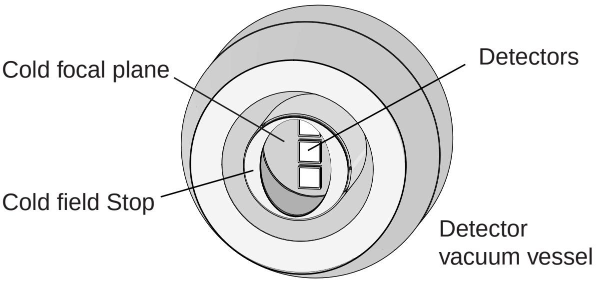

Fig. 2.3.2. Outline of the detector component. The vacuum vessel contained the cold shield and the cold focal plane upon which were placed three detectors and band-pass filters. The cold finger of the cryogenic cooler displacer was attached to the back of the vessel.

To satisfy the wavelength accuracy requirement of less than $3 \times 10^{-7}$ in the ratio at 25 ±5 °C for three years, the newly designed HeNe laser made of a glass block with an ultralow thermal expansion coefficient (less than $\pm 5 \times 10^{-8}$/K) was used. The laser beam was expanded and injected into the interferometer, and light interference was detected with four Si detectors positioned circumferentially in order to detect the position and the inclination of the moving mirror.

The IMG used three bands with two PV-type InSb detectors for the shorter wavelength range and one PC-type HgCdTe (MCT) detector for the longer wavelength range to cover the required wavelengths between 3.3 $\mu$m and 14 $\mu$m. The MCT detector is well known to have a nonlinear relation between the input power and the output signal. The ground test showed that nonlinearity arose when the sensor target temperature was higher than 280 K. This effect was compensated for by a quadratic equation at the processing stage of the interferograms in the ground system. The coefficients of the quadratic equation were defined from the results of ground tests. The cold components, detector focal plane and the shield attached for eliminating the background radiation from the warm optical system, were placed in the vacuum vessel, and were thermally combined with the cryogenic cooler displacer. The field of view (FOV) was defined by the size of the detectors as 8 km by 8 km at the ground. Figure 3 shows the outline of the detector component.

Considering the configuration of the detectors' electronic circuits and the oval hole of the cold field stop, designed from the perspective of the beamsplitter, the three detectors were aligned. This detector arrangement provided a simple focal-plane design and an efficient thermal design for the detector vessel, however, for observations of a partially clouded surface, careful data analysis was required.

A preliminary study on future scientific applications that require the use of multiple spectrum bands, especially in the retrieval of atmospheric constituents, was performed. As a result, we determined that quality control of the data should be performed using information obtained from data for partially clouded surfaces; then this arrangement would not introduce severe data corruption. The cloud information can be obtained from the OCTS (ocean color and temperature sensor, on board the ADEOS as an IMG) or the IMG spectrum itself.

The internal blackbody was flat and coated with black paint on its v-shaped grooved surface. This blackbody did not have its own temperature control system and was equipped with three platinum temperature sensors to monitor the blackbody temperature. An ideal emissivity of 1 for a flat blackbody cannot, in general, be achieved. The design team attempted to raise the emissivity (the emissivity of the blackbody was 0.95~0.97 at the wavenumber of 700~2000 $cm^{-1}$) and to control the reflected radiation from the internal temperature-monitoring components to obtain an effectively high emissivity for the calibration. The ground evaluation for the blackbody showed that it could satisfy the required radiometric accuracy. The results of IMG thermal design showed that the entire optical system, except for the detector components, would operate at ambient temperature, i.e., about 273~308 K in space.

The image motion compensation mirror (IMC) was designed to orient the optical axis for the blackbody / deep-space / earth observations by means of a one-axis stepping motor for this spectrum calibration, and also to compensate the motion of the image of the surface of the earth due to satellite movement, by means of two-axis gimbal support. The microprocessor unit (MPU) for the IMC controlled the mirror movement. The IMC was also designed to make an angled observation in order to monitor earth surface phenomena that do not occur at the satellite nadir position.

Figure 2.3.3 shows the moving mirror alignment and suspension control system diagram. The control system maintained the parallelism of the two mirrors to within $1.9 \times 10^{-4}$ degrees (0-peak) throughout the 10 cm length of the moving mirror path. An additional 3 seconds were required for the mirror to return. The alignment control system had double control loops. The basic control loop was controlled by the gap sensors to sustain the initial alignment bias obtained during the startup alignment modes. The second control loop supports the dynamic alignment mechanism that maintains the defined parallelism throughout each observation. The control system was also designed to accept the predefined alignment bias which could be modified by the ground command. This alignment bias defined the offset angle of the moving mirror.

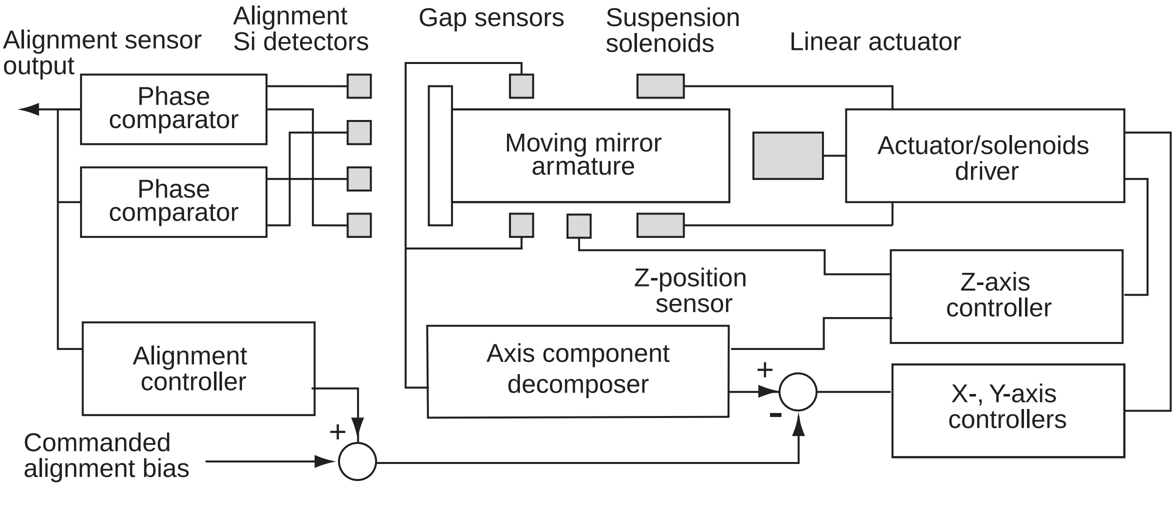

Fig. 2.3.3. Moving mirror alignment and control system diagram. The control system had double control loops. In the basic loop, the moving mirror armature was suspended and the parallelism was sustained with a predefined alignment bias. The second loop supported the dynamic alignment throughout the observation, using the interference signal of the HeNe laser.

## 2.4 DEVELOPMENT OF PROTO-FLIGHT MODEL

Following the negotiations with the NASDA, The operational/physical/electrical interface between the IMG and the satellite bus was defined. The principal characteristics of the proto-flight model (PFM) are shown in Table 2.4.1. Figure 2.4.1 shows an outside view of the IMG. The IMG covers wavelengths between 3.3 $\mu$m and 14 $\mu$m with three separate bands. Aluminum honeycomb enclosures were used to minimize IMG weight; the total instrument weight was 130 kg. For band 1, interferogram sampling was performed, once every two laser fringes, and once every three laser fringes for bands 2 and 3 respectively. Onboard data compression was not adopted. The restriction of the data transmission rate defined the sampling number of the interferogram.

To calibrate the spectrum, two observations were made repeatedly: one internal blackbody observation for the higher temperature reference and one deep-space observation as a lower temperature reference. Figure 2.4.2 shows the observation/calibration cycle of the IMG in the observation mode.

The IMG observed the infrared radiation of a fixed observation area for 10 seconds. The traveling mirror traveled 10 cm during this observation period of 10 seconds. The observation cycle and foot print on the ground is shown in Figure 2.4.3.

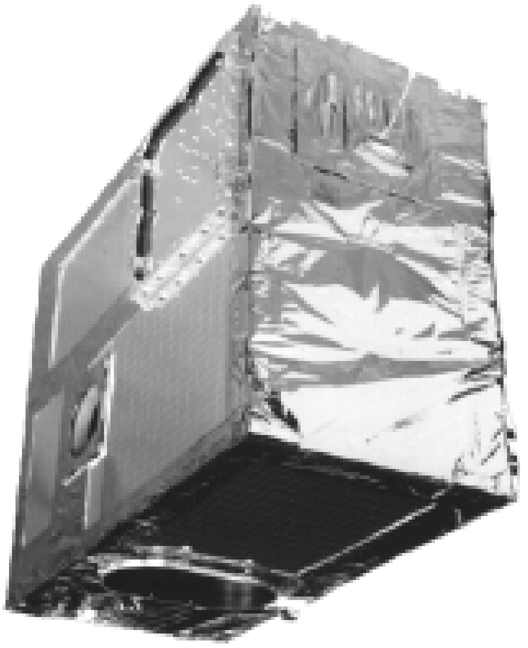

Fig. 2.4.1. Outside view of the IMG. the aluminum honeycomb enclosures was covered by the thermal insulator. The oval shape aperture of the lower panel is the inlet of the interferometer.

Table 2.4.1. Principal characteristics of the IMG PFM.

| | |
|---|---|
| Spectral range | 714 ~ 3030 cm$^{-1}$ (3.3 ~ 14 $\mu$m) |
| Number of bands<br>Range of band 1<br>Range of band 2<br>Range of band 3 | 3<br>2325 ~ 3030 cm$^{-1}$ (3.3 ~ 4.3 $\mu$m)<br>2000 ~ 2500 cm$^{-1}$ (4.0 ~ 5.0 $\mu$m)<br>714 ~ 2000 cm$^{-1}$ (5.0 ~ 14 $\mu$m) |
| Number of samplings | band 1: 1.6 x 10$^5$<br>band 2 & 3: 1.0 x 10$^5$ |
| Data rate | 882 kbps |
| Power consumption | 149 W |
| Weight | 129.7 kg (except remote interface unit) |
| Dimensions | 1150 x 930 x 650 mm |

## 3. OPERATION EXPERIENCE AND HARDWARE EVALUATION

The ADEOS satellite was a large bus intended for observations of the earth using multiple sensors, in a sun-synchronous, 41-day recurrent polar orbit, at an altitude of 800 km. The IMG operated continuously day and night, but, was under the basic schedule of 4 days operation and 10 days standby. Before the start of the System Initial Checkout, the launch locks for movable parts of the IMG, such as the traveling mirror, were released on September 5, 1996. The Initial Checkout on the IMG unit was performed between September 20 and October 10, 1996. After the functional tests, the first observation was performed on October 10, 1996. ADEOS System 1 & 2 Operation Tests were completed on November 5. The functions and the characteristics of the IMG performances were confirmed to be comparable with results obtained by the ground test.

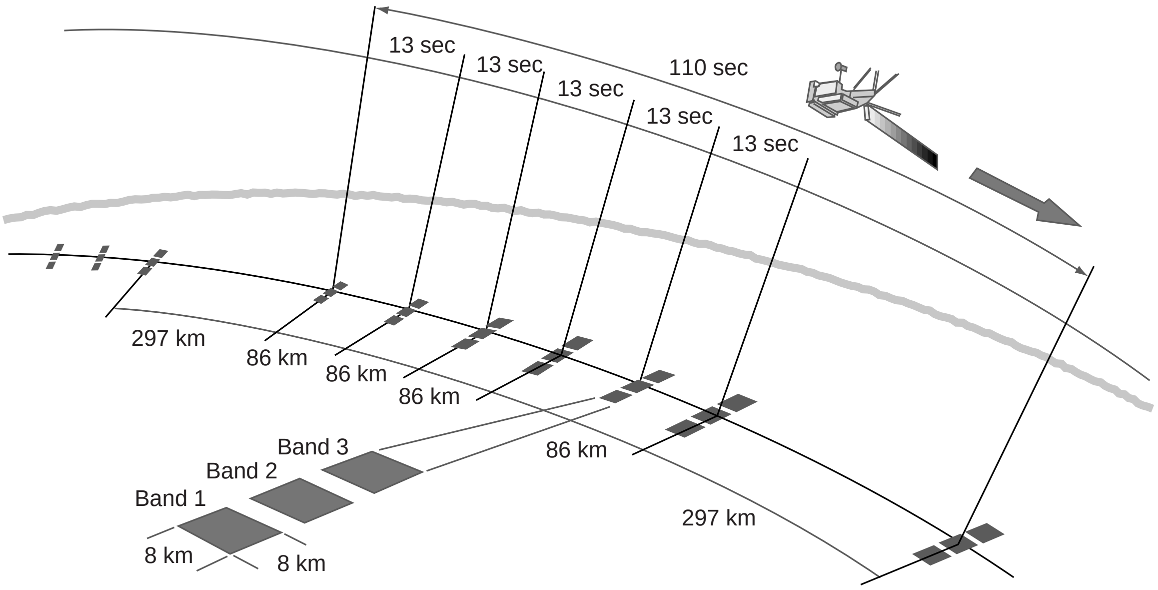

Fig. 2.4.2. The operation pattern of the observation/calibration cycle of the IMG in the observation mode.

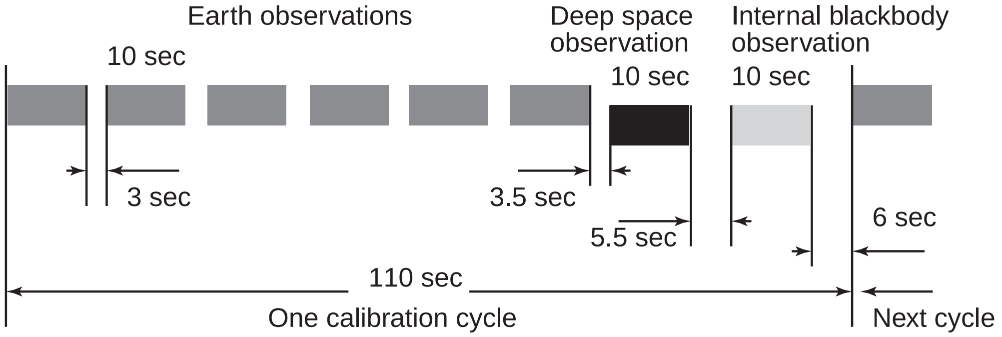

Fig. 2.4.3. Observation cycle and footprint.

## 3.1 TROUBLE SHOOTING

Routine ADEOS/IMG operations began on November 26, 1996. At the beginning of the operation, the moving mirror alignment system occasionally stuck at an anomalous alignment position, resulting in unacceptable degradation of the interferogram. After troubleshooting, it was found that when the moving mirror vibrated, the dynamic alignment system slipped. It was determined that such vibration was induced by the control system's insufficient gain which was defined in the ground test in which zero gravity was simulated. The slippage of the dynamic alignment system, which introduced the degradation of data performance (reproducibility, NESR), occurred randomly. Occasionally, the slippage was followed by sticking and caused fatal alignment deviation. It was anticipated that such anomalies could be reduced by adjusting the moving mirror alignment control bias, because the control bias was related to the slippage margin. Fortunately, this control bias could be preset through commands given from the ground. Trials to identify the optimum bias continued during the routine operations until the end of June 1997, when satellite failure occurred.

Table 3.1.1 summarized the IMG operation period, where REQQ is the ADEOS operation unit (sensor operation request file which was the interface between the satellite operator and the each sensor operator) defined by NASDA.

Because the IMG observations are aligned with the satellite orbits, the unexpected occasional IMG failures introduced an inhomogeneous global observation pattern. From the global monitoring perspective, we should design the IMG successors

Table. 3.1.1. The IMG operation period and the corresponding REQQ period. The schedule of 4 days operation and 10 days standby was the basic IMG operation, and sometimes the longer continuous operation was performed.

|  | IMG operation date | Remarks | Satellite operation status | REQQ period |
|---|---|---|---|---|
| 1 | 96/10/04, 96/10/10 |  | Initial checkout | 96/10/04-96/10/10 |
| 2 | 96/10/15-96/10/18 |  | SYS-1 | 96/10/15-96/10/29 |
| 3 | 96/10/30-96/11/02 | sensor alignment error | REQQ-1 | 96/10/30-96/11/26 |
| 4 | 96/11/06-96/11/30 | continuous operation for the IMG field campaign with daily alignment command | REQQ-2 | 96/11/27-96/12/24 |
| 5 | 96/12/11-96/12/14 | alignment command transmission |  |  |
| 6 | 96/12/25-96/12/28 | serial magnitude command transmission for the alignment offset angle change | REQQ-3 | 96/12/25-97/01/21 |
| 7 | 97/01/08-97/01/11 | ditto till the REQQ-9 |  |  |
| 8 | 97/01/25-97/01/28 |  | REQQ-4 | 97/01/22-97/02/18 |
| 9 | 97/02/08-97/02/11 |  |  |  |
| 10 | 97/02/22-97/02/25 |  | REQQ-5 | 97/02/19-97/03/18 |
| 11 | 97/03/08-97/03/11 |  |  |  |
| 12 | 97/03/22-97/03/25 |  | REQQ-6 | 97/03/09-97/04/15 |
| 13 | 97/04/01-97/04/10 | ADEOS campaign period |  |  |
| 14 | 97/04/21-97/04/24 |  | REQQ-7 | 97/04/16-97/05/13 |
| 15 | 97/05/05-97/05/08 |  |  |  |
| 16 | 97/05/19-97/05/22 |  | REQQ-8 | 97/05/14-97/06/10 |
| 17 | 97/06/02-97/06/05 |  |  |  |
| 18 | 97/06/16-97/06/19 |  | REQQ-9 | 97/06/11-97/07/04 |

to observe the surface by the push-broom-like method, involving the observation of points in a zigzag manner.

## 3.2 EVALUATION OF THE HARDWARE IN SPACE

The radiometric characteristics, wavenumber resolution, and the reproducibility of measurements and data trends were evaluated using mission and housekeeping data from the IMG. Hardware evaluation is necessary not only for the standard products of the IMG derived from the raw data but also to validate the hardware design for future IMG sensors.

### 3.2.1 REPRODUCIBILITY

Even when the interferometer was settled in a quiet condition, such as the ground test when the entire instrument was mounted on an antivibration bed, and was operated in a vacuum chamber, each repeatedly obtained interferogram has some variance. On the IMG, this fluctuation affected the calibration accuracy of the earth observation spectra because the radiometric calibration was performed with two blackbody observations performed before and after six earth observations. We defined this discrepancy as the “reproducibility,” and expressed it in terms of the spectrum, not the interferogram. The degradation of reproducibility was mainly caused by fluctuation of the alignment due to internal/external disturbance and was related to the presettable alignment bias. In the final ground tests,

Table 3.2.1.1. Reproducibility (1 sigma: K). The reproducibility was varied according to the X- and Y-offset angles of the moving mirror alignment control system. The offset angles was changed several times by the ground command to obtain the maximum stability of the moving mirror.

| | wavenumber ($cm^{-1}$) | band 1 | | | band 2 | | | | band 3 | | | | |
|---|---|---|---|---|---|---|---|---|---|---|---|---|---|
| | | 3000 | 2600 | 2400 | 2400 | 2300 | 2200 | 2000 | 2000 | 1500 | 1000 | 800 | 750 |
| X and Y offset(degree) | nominal | 2.65 | 0.35 | 0.18 | 0.55 | 0.44 | 0.41 | 0.26 | 0.41 | 0.38 | 0.31 | 0.37 | 0.33 |
| | -0.000375 | 2.56 | 0.86 | 0.25 | 1.18 | 1.00 | 0.70 | 0.23 | 0.65 | 0.68 | 0.31 | 0.39 | 0.34 |
| | -0.0003 | 3.27 | 1.59 | 0.36 | 1.69 | 1.52 | 0.99 | 0.39 | 0.84 | 1.11 | 0.43 | 0.35 | 0.31 |
| | other | 2.67 | 0.62 | 0.35 | 0.70 | 0.63 | 0.45 | 0.28 | 0.52 | 0.47 | 0.24 | 0.26 | 0.25 |

the reproducibility could not satisfy the initial requirement of 0.1 K (1 sigma) because the moving mirror vibration frequency was outside the control frequency range, and the required specification of the reproducibility was waived.

The reproducibility was given as the equivalent temperature of the standard deviation of a blackbody observation spectral data set in one orbit, where the spectra were calculated using a smaller 210 data number of the interferogram to reduce effects from noise. Under the nominal alignment conditions, the reproducibility in orbit was almost the same as the results of the ground test. The nominal offset angle (X= -0.00062 degrees, Y= -0.00069 degrees) was determined in order to achieve the best signal level and reproducibility during the ground tests. However, the alignment offset angle was related to the probability of alignment system slippage. To reduce the slippage of alignment, the offset values were changed. The offset angle and the fluctuation of the alignment angle during observation affected the modulation efficiency (interferometric efficiency), and the reproducibility of the spectra was degraded. Table 3.2.1.1 shows the results of analysis for various offset angles.

The magnetic suspension system for the moving mirror has, generally, relatively low stiffness and is easily affected by the inner/outer perturbations. In the IMG design process, we considered that the initial requirement of 0.1 K was achievable target, however, the massive moving mirror introduced the reduction of the design margins. The next sensor should adopt a lightweight moving mirror made of a material other than aluminum alloy.

Table 3.2.2.1. NESR ( $mW/cm^2/sr/cm^{-1}$). The reference blackbody temperature was 300 K, and the NESR data in orbit were estimated from the observations of the on-board blackbody whose temperature was 270 K.

| Band | Wavelength ( $\mu$m) | Initial scientific request | Designed specification | PFT | Results in orbit | |
|---|---|---|---|---|---|---|
| | | | | room-temperature condition | initial check-out period | offset angle -0.000375 deg. ('96/12/28) |
| Band 3 | 14 | <0.03 | <0.035 | 0.032 | 0.027 | 0.031 |
| | 10 | <0.02 | <0.025 | 0.023 | 0.020 | 0.021 |
| | 8 | <0.03 | <0.03 | 0.023 | 0.021 | 0.012 |
| | 7 | <0.02 | <0.03 | 0.028 | 0.025 | 0.027 |
| Band 2 | 4.7 | <0.04 | <0.004 | 0.002 | 0.002 | 0.002 |
| | 4.5 | <0.001 | <0.0025 | 0.002 | 0.002 | 0.002 |
| Band 1 | 4.3 | <0.00013 | <0.002 | 0.0012 | 0.002 | 0.002 |
| | 3.3 | <0.0002 | not defined | 0.0016 | 0.003 | 0.004 |

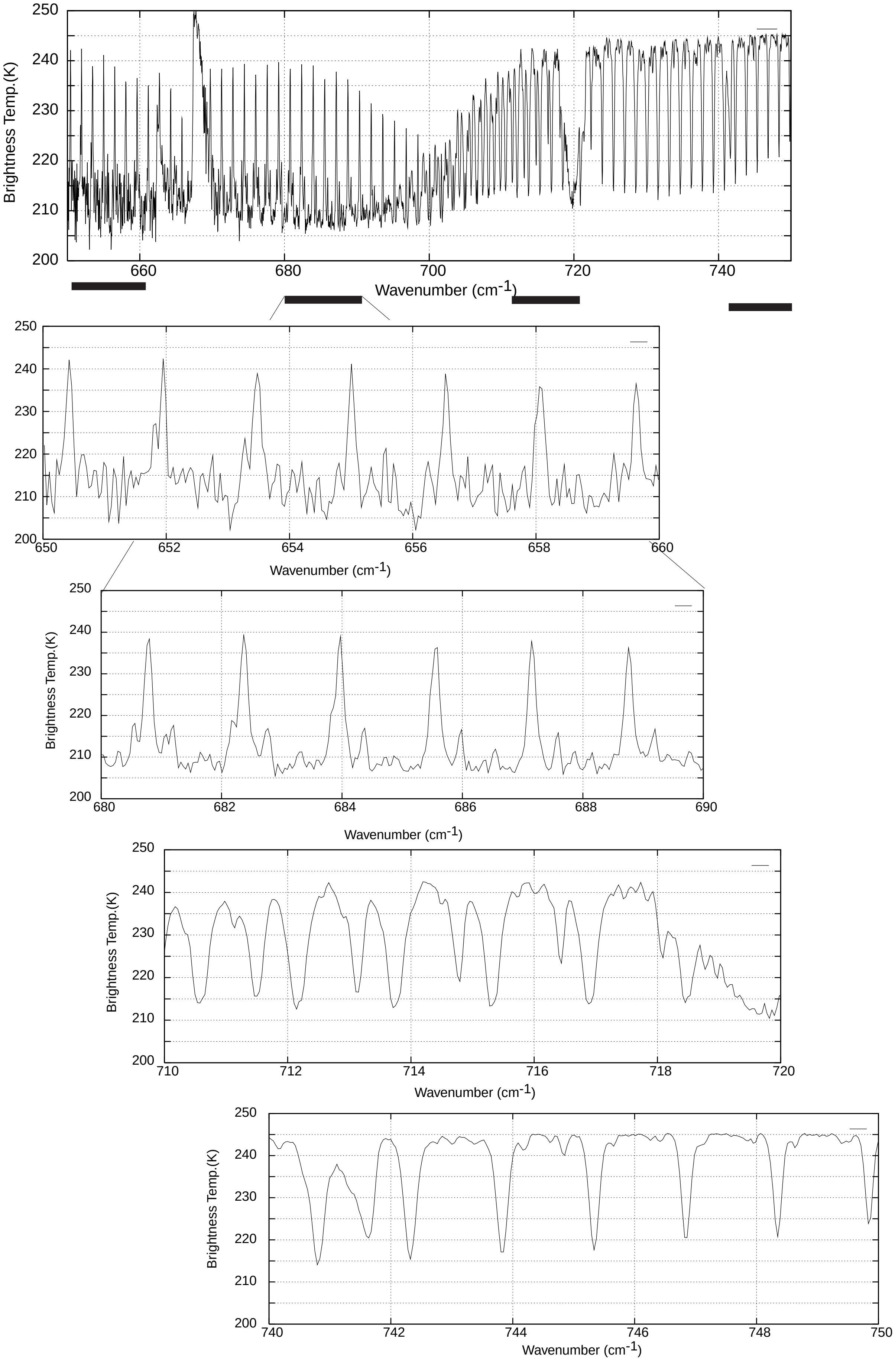

Fig. 3.2.2.1. A sample of the IMG-observed band 3 spectra. The range definition of band 3 was expanded after the data evaluation. The most upper figure is a lower wavenumber end part of the sample, and the lower four figures are close-up of this spectrum.

### 3.2.2 NESR

Noise levels of the spectrum, expressed as the noise equivalent spectral radiance (NESR), were the same as in the results of the ground tests (thermal vacuum test of proto-flight test (PFT)), and the signal levels of the spectra were almost the same as the results of the ground tests. The NESR was calculated from the ratio of the noise (standard deviation of the residual of raw spectrum minus the smoothed spectrum using the smaller 210 data number of the interferogram for the calculation) and the signal (the smoothed spectrum) of a blackbody observation spectrum. The following table shows the mean value of the NESR in the ground tests, in the Initial Checkout process (nominal offset angle), and under an additional condition (offset angle was -0.00375 degrees).

On the spectral range, the longer wavelength region was expanded after the evaluation of data in orbit. The range of band 3 was redefined to 667 ~ 2000 $cm^{-1}$ on the basis of the evaluation results of data in orbit, because the S/N was sufficient to enhance the definition. Figure 3.2.2.1 shows a close up of the lower end of the band 3 sample spectrum. S/N improvement was obtained with lower detector temperature (75 K after the Initial Checkout process) attainment.

The IMG NESR for bands 2 and 3 satisfied the scientific and designed specifications in most cases as shown in Table 3. For band 1, the NESR values satisfied the designed target, however, there are large discrepancies between the achieved NESRs and initial scientific requests. In the next IMG, the NESR can be enhanced by the several techniques, such as band partitioning that could not be adopted for the IMG because of the limited weight and power resources.

### 3.2.3 WAVENUMBER ACCURACY

The accuracy of the spectrum was related only to the accuracy and stability of the onboard HeNe laser wavenumber, and precise estimation for the onboard laser is difficult. Thus, we compared the observed spectra with a theoretically calculated one. Figure 3.2.3.1 shows a close-up of the atmospheric radiation spectra for some regions in which the representative atmospheric constituent absorption lines are included. The figures show IMG-observed spectra and the calculated spectrum using a line-by-line atmospheric radiative transfer model, FASCODE [6]

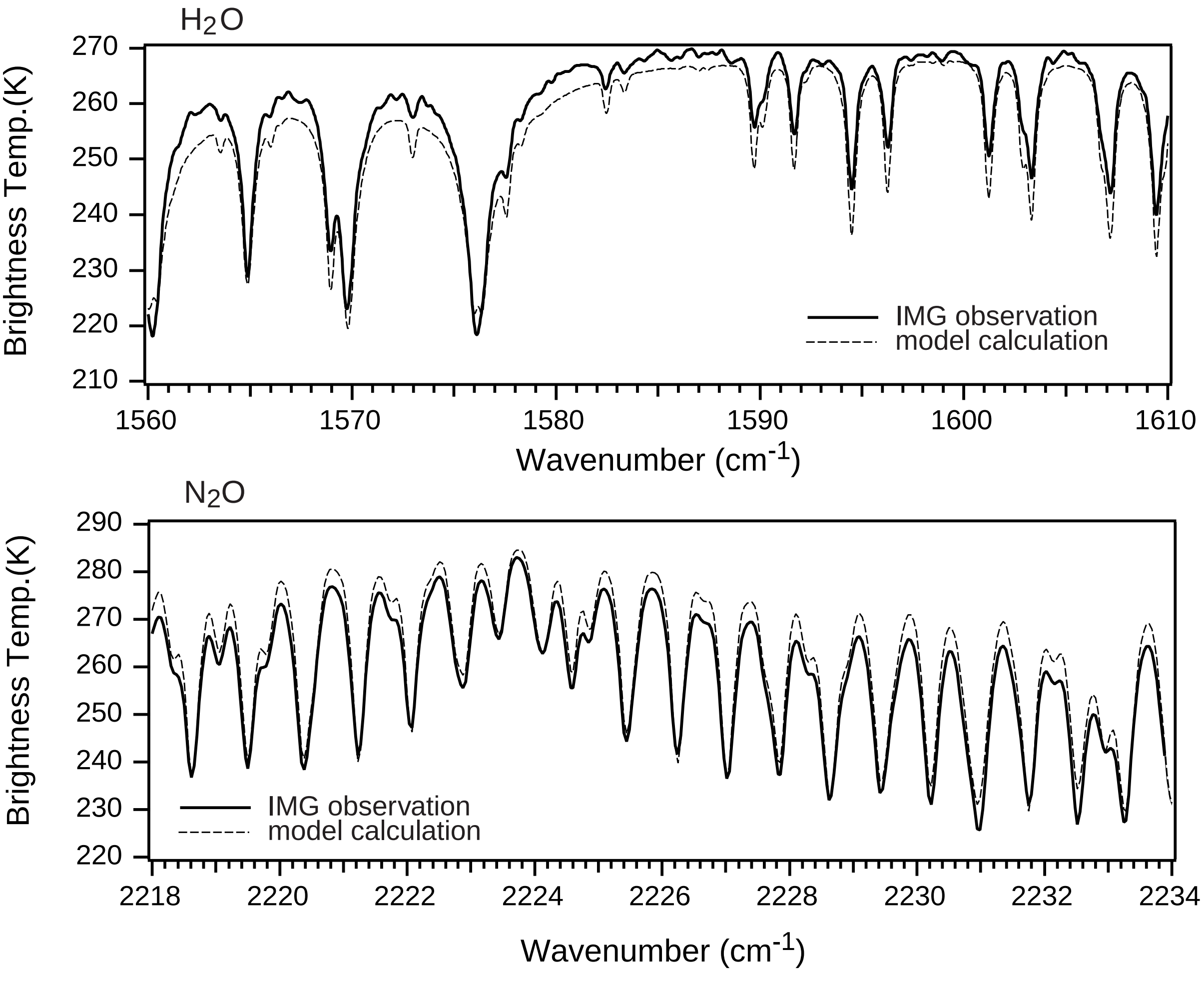

Fig. 3.2.3.1. IMG-observed and calculated atmospheric spectral radiances. The solid line is the IMG-observed and the dashed line is the theoretically calculated spectra. The model used for this calculation is FASCODE 3 with the line database HITRAN 92.

version 3. The FASCODE calculation uses interpolated objective analysis temperature/humidity profiles at the point and time of IMG observation and the FASCODE-equipped constituent gases profiles, but does not take aerosols into consideration. In the figure, we see good agreement between the observed and calculated atmospheric emissions and the gas absorption line spectra in terms of the wavenumber accuracy. We can see differences between the two spectra in terms of the radiance. These discrepancies can be explained generally by the fact that the atmospheric constituent profiles used in this simulation were different from the actual profiles observed by the IMG. We can retrieve amounts of atmospheric constituents from the residuals obtained from the observed spectrum minus the estimated spectrum calculated using the initial-guessed temperature and other gas profiles.

As mentioned in the previous section, the detectors were aligned. This arrangement affected the scaling coefficients for defining the wavenumber of the spectra. The ground segment processed spectra (Level 1) using the analytically obtained coefficients.

minimizing the residuals of two spectra.

Generally, the instrument function of a FTIR is affected by not only the detector size, shape, and position, but also other instrument parameters such as alignment conditions and inhomogeneity of the detector material. The differences shown in the Table 4 can be explained by considering that the analytically calculated values were the theoretical target of the IMG design. Since theoretical estimation of the instrument function is difficult in general, we should define a test method to estimate the resolution for the evaluation of the FTIR sensors for earth atmosphere observation.

## 4. SPECTRAL CALIBRATION ALGORITHM

All ADEOS downloaded data have been archived at the NASDA earth observation center (EOC). The EOC had formulated basic data processing such as data formatting, and distributed the IMG data to our ground segment of the IMG, IMGDIS, with the D-1 (large cassette type digital media) tapes. The IMGDIS produced the standard products from the raw data (Level 0 data) to the spectral data (Level 1 data), and retrieved physical data (Level 2 data).

Table 3.2.4.1. Spectrum resolution (half maximum full width; HMFW).

| band | band 2 | | | band 3 | | | |
|---|---|---|---|---|---|---|---|
| wavenumber ($cm^{-1}$) | 2000 | 2100 | 2200 | 700 | 1000 | 1500 | 1800 |
| resolution ($cm^{-1}$) analytically calculated | 0.10 | 0.10 | 0.10 | 0.10 | 0.14 | 0.21 | 0.25 |
| resolution ($cm^{-1}$) estimated by FASCOD3 | 0.10 | 0.10 | 0.10 | 0.12 | 0.16 | 0.18 | 0.21 |

### 3.2.4 SPECTRUM RESOLUTION

The design-based spectrum resolution of IMG is 0.1 $cm^{-1}$ taking into consideration the detector size and shape, however, there is some degradation in the spectra of bands 1 and 3. The degradation of the resolution was caused by the detector size and arrangement (the band 2 detector was at the center of the field of view, and the band 1 and 3 detectors were positioned on either side of detector 2). The resolution data obtained both analytically and by the FASCOD3 simulation are shown in the following table. The FASCOD3 simulation was processed using the following steps: 1) selection of sample spectra from the IMG Level-1 data, 2) preparation of simulated spectra at several resolutions using FASCOD3 with rectangular instrument function and appropriate temperature/humidity profiles, 3) estimation of the spectrum resolution for the specified wavenumber using the criterion of

### 4.1 DEVELOPMENT OF FLIGHT SIMULATOR OF THE IMG

As previously mentioned, IMG transmitted all the raw interferograms to the ground. In the IMGDIS process, the raw interferograms were Inverse-Fourier transformed and radiometrically calibrated. On the raw interferograms of band 3, they were collected with the amplitude by the nonlinearity compensation equation as mentioned in section 3.

Prior to the launch of the ADEOS, we developed the airborne FTIR called the tropospheric infrared interferometric sounder (TIIS) to simulate the IMG. TIIS was developed in 1993 by CRIEPI/JASCO corp. The first flight was carried out in the winter of 1994. The objective of using TIIS was to develop a calibration algorithm for IMG, and to validate the atmospheric constituents retrieval algorithm that was developed by the IMG science team. The main specifications of IMG and TIIS are shown in Table 1. TIIS makes use of the Michelson interferometer as the IMG and has 3 bands covering the same bandwidth as IMG. TIIS, keeping in mind that it is loaded on board an aircraft, has a corner-cube moving mirror and an optical input aperture diameter of 2.5 cm. IMG and TIIS have almost 0.1 $cm^{-1}$ spectral resolution. TIIS has two blackbodies, one kept at ambient temperature and one cooled by liquid nitrogen ($LN_2$). By adjusting the front-end mirror, TIIS can be used to observe the down-welling atmospheric emission on the ground.

Sometimes the interferogram from the FTIR is asymmetrical around the zero path difference. The asymmetry is said to be due to radiations from the internal optics, and the beam splitter, and sampling error of the optical path difference [3], [4]. Tto compensate foe the error due to these causes, the sampling of the double-sided interferograms are generally adopted. Assuming a linear relationship between the incident spectral radiance and the output spectrum, we can represent the obtained spectrum as

$$C = r(L + L_0)\,, \tag{4.1}$$

where

r : the response function,

L : the incident spectral radiance,

$L_0$ : the background spectral radiance from an instrument.

To cancel the phase error on the spectrum described above, C, the magnitude spectrum from a complex Fourier transformation, is used. In the same way, the obtained spectra of the blackbodies with temperatures $T_c$ and $T_h$ ($T_c<T_h$) are represented by

$$C_c = r(B_c + L_0) \tag{4.2}$$
$$C_h = r(B_h + L_0)\,, \tag{4.3}$$

where B is the Planck radiance.

In these equations, emittances from blackbodies are assumed to be 1. Eqs. (4.1), (4.2), and (4.3) yield the following calibration relationship.

$$L = [(C-C_c)/(C_h-C_c)](B_h - B_c) + B_c \tag{4.4}$$

Furthermore, taking the anomalous phase response associated with the background radiance into consideration, Revercomb et al. [6] presented the calibration method using a complex spectrum from the complex Fourier transformation represented by Eq. (4.5), instead of Eq. (4.1),

$$C' = r[L + L_0 \exp(i\phi_0)] \exp(i\phi)\,, \tag{4.5}$$

where

$\exp(i\phi_0)$ : the anomalous phase response of the background,

$\exp(i\phi)$ : the normal phase response of the instrument.

By this method, C, $C_c$ and $C_h$ in Eq. (4.4) for the calibration relationship are related to the complex spectra. To apply this relationship, sampling points with the same optical path difference on interferograms obtained from the measurement of blackbodies for reference and from the measurement of the observation target, must be identified.

Since TIIS, like the IMG, was not equipped with any function, such as white light to identify the optical path difference, we had to develop a method for determining the points with the same optical path difference. Now, the calibrated spectrum derived from the calibration relationship using the complex spectra can be expressed as

$$L = |L| \exp[i\phi_L], \tag{4.6}$$

where $\phi L$ is the retained phase. Assuming the stability of the anomalous phase response and the normal phase response of the instrument shown in Eq. (4.5), the phase term of a calibrated spectrum, which is represented as the arc tangent of the ratio of the imaginary part to the real part, should be completely canceled. In actual practice, the phase term does not become zero due to noise and instability. Furthermore, the calibration using interferograms, which are not assigned the same optical path difference at each point on each interferogram, yields the phase term of the calibrated spectrum. In other words, the phase term should be minimum or ideally zero, if an appropriate optical path difference is assigned to the interferograms. Therefore we established a criterion for determining the sampling points with the same optical path difference on each interferogram for calibration, expressed by

$$|\phi_L| = \text{minimum}. \tag{4.7}$$

The minimum phase term was obtained by iteration of the calibration procedure using only the center part of interferograms. Using the developed method, we carried out the calibration of the measurement.

## 4.2 SPECTRAL CALIBRATION OF THE IMG

IMG has the same specifications as the TIIS, as well as an advanced signal-to-noise ratio as a result of the large optical input aperture diameter of 10 cm. Also, the surface of detectors are treated with antireflection coating to reduce reverse radiation. The calibration can be performed using the method described in the previous section, however, the calibration scheme must include special steps. IMG produces interferogram sampling with an interval of three He-Ne laser fringes to reduce the volume of the data stream from the satellite to the ground while satisfying the minimum necessary range of spectra obtained from the interferograms. We required three interferograms, one from the ambient-temperature IMG internal blackbody, one obtained from the observation of deep space as a cold-temperature reference, and one from atmospheric observation. The three interferograms should have sampling points with the same optical path difference, however, not all IMG observations satisfy this criterion. That is why the starting points of sampling for individual observations are not fixed at the position with the same optical path difference. Because of this, we had to interpolate an interferogram at one-third of the sampling interval. Further interpolation between the laser fringes was not adopted in order to save processing time. The interpolation of the interferogram was performed using

$$\mathrm{n} = \mathrm{InverseFourier}\{\,|\,\mathrm{C}\,|\,\exp[-\mathrm{i}(\phi \mathrm{L}+\delta\phi_{\mathrm{n}})]\} \tag{4.8}$$

$$\delta\phi_{\mathrm{n}}(\mathrm{l}) = 2\pi \mathrm{n}\lambda_{\mathrm{l}}/\lambda, \tag{4.9}$$

where

I : interferogram
$\lambda$ : wavelength
$\lambda_{\mathrm{l}}$ : wavelength of He-Ne laser
n : 0,1,2.

## 5. RETRIEVAL ALGORITHM OF THE PHYSICAL PARAMETERS

The L2-processing consists of the calculation process of the radiative transfer model and the inversion process. The inversion process retrieves the temperature profile, water vapor profile, surface pressure, and the greenhouse gases profiles simultaneously, based on the most likelihood method. We termed these profiles as the "physical parameters." For the radiative transfer calculation, we developed the rapid calculation algorithm.

### 5.1 THEORETICAL BASIS

There are several approaches to obtain atmospheric parameters acquired from remote sensed data, and the IMG data analysis requires solving of the inversion program.

### 5.1.1 INVERSION SCHEME

We adopted the maximum likelihood method which takes into account the statistical prior knowledge into the least squares method. In the maximum likelihood method, the estimator is expressed as follows.

$$\hat{\mathbf{x}} - \mathbf{x_0} = \mathbf{R}^{-1}\mathbf{A}^{\mathbf{T}}\mathbf{E}^{-1}(\mathbf{y} - \mathbf{y_0}) \tag{5.1}$$

$$\mathbf{R} = \mathbf{Q} + \mathbf{S}^{-1}, \quad \mathbf{Q} = \mathbf{A}^{\mathbf{T}}\mathbf{E}^{-1}\mathbf{A} \qquad (5..2)$$

where

$\hat{\mathbf{x}}$ ; vector to be solved (estimator). It has components as many as the number of analytical physical parameters, $\mathrm{M}$ .

$\mathbf{x_0}$ ; initial guess for $\hat{\mathbf{x}}$ . It may be obtained from the analysis of climatological data set.

$\mathbf{y}$ ; vector of observations (radiance). It has as many rows as the number of channels used, $\mathrm{N}$ .

$\mathbf{y_0}$ ; vector of radiance which is associated with $\mathbf{x_0}$ $(= f(\mathbf{x_0}))$ .

$\mathbf{A}$ ; the Jacobian matrix for N channels and M parameters.

$$= \frac{\partial \mathbf{f}}{\partial \mathbf{x}} = \left(\vec{\mathbf{a}}_1, \vec{\mathbf{a}}_2, \cdots, \vec{\mathbf{a}}_{\mathbf{N}}\right)^{\mathbf{T}}, \qquad \vec{\mathbf{a}}_{\mathbf{i}} = \left(a_{i,1}, a_{i,2}, \cdots, a_{i,M}\right)$$

$\mathbf{E}$ ; the error covariance matrix. It includes observed noise and forward model error.

$\mathbf{S}$ ; the covariance matrix of $\mathbf{x_0}$

Equation (5.1) is derived by minimizing the bilinear form,

$$\mathbf{e}_y^T\mathbf{E}^{-1}\mathbf{e}_y + \mathbf{e}_x^T\mathbf{S}^{-1}\,\mathbf{e}_x$$

where, $\mathbf{e}_y = (\mathbf{y} - \mathbf{y_0}) - \mathbf{A}(\mathbf{x} - \mathbf{x_0})$ , $\mathbf{e_x} = (\mathbf{x} - \mathbf{x_0})$

(5.3)

$f(\mathbf{x})$ is the forward function of x and it derives the radiation which is assumed to be observed by the IMG. The forward model is deeply connected in the retrieval process. The function is expressed according to the atmospheric radiative transfer model. While the calculation of the model is highly time consuming, we had to execute the analysis in the short time corresponding to the IMG observation time. Some ideas were adopted for rapid calculation, and they will be referred to in the following section.

Actually, since the infrared spectrum is affected by geophysical parameters in a nonlinear way, in Eq. (5.1) it is assumed that $\mathbf{y}$ can be linearized around $\mathbf{x_0}$ .

$$\mathbf{y}-\mathbf{y_0}=\mathbf{A}(\mathbf{x}-\mathbf{x_0}) \tag{5.4}$$

Therefore, it is important to establish an initial guess near the true vector of unknown parameters $\mathbf{x_{true}}$ in which the linearization is acceptable. An iterative calculation is also effective, so that the estimator $\hat{\mathbf{x}}$ will converge to the global minimum point of error curve Eq. (5.3). In an iterative method, the k-th estimator $\hat{\mathbf{x}}_\mathbf{k}$ is used as the linearization point for the next iteration. $\hat{\mathbf{x}}_\mathbf{k+1}$ is expressed as follows.

$$\hat{\mathbf{x}}_\mathbf{k+1}-\hat{\mathbf{x}}_\mathbf{k}=\mathbf{C}_k(\mathbf{y}-\mathbf{y_k})+(\mathbf{I}-\mathbf{C}_k\mathbf{A}_k)(\mathbf{x_0}-\hat{\mathbf{x}}_\mathbf{k}) \tag{5.5}$$

$$\mathbf{C}_k=\mathbf{R}_k{}^{-1}\mathbf{A}_k{}^{\mathbf{T}}\mathbf{E}_k{}^{-1} \tag{5.6}$$

where $\mathbf{C}_k, \mathbf{R}_k$ , $\mathbf{A}_k$, *and* $\mathbf{E}_k$ are calculated using $\hat{\mathbf{x}}_\mathbf{k}$ . Iteration can reduce the nonlinearity effects, and the final estimation is obtained when sufficient convergence is achieved.

## 5.1.2 TOLERANCE ERROR

The number of parameters, M, to be retrieved and the number of channels, N, entering the matrixes of Eq (5.1), are also factors to be considered. In our measurement system, a large number of channels were obtained , and hundreds of parameters had to be retrieved (N >> M).

Using the inversion analysis method for measurement, results in an increase in the number of channels, which results in higher accuracy. However , this increase in accuracy is accompanied by an increase in the cost of computational resources. Furthermore, to solve the parameters with good accuracy, consideration of the estimation errors is required.

For the sake of simplicity, Eq. (5.4) is rewritten as

$$\mathbf{y}=\mathbf{Ax} \tag{5.7}$$

where, $\mathbf{x}=\hat{\mathbf{x}}-\mathbf{x_0}$, $\mathbf{y}=\mathbf{y}-\mathbf{y_0}$ and $\mathbf{A}$ is the Jacobian matrix, that is the sensitivity of the observed data for each unknown parameter.

The observed vector $\mathbf{y}$ can be written as

$$\mathbf{y}=\mathbf{A}\cdot\mathbf{x_{true}}-\mathbf{e_y} \tag{5.8}$$

where $\mathbf{x_{true}}$ is true of $\mathbf{x}$ , $\mathbf{e_y}$ is observation error. Then, estimation error $\mathbf{e_x}$ is written as

$$\begin{aligned}\mathbf{e_x}&=\hat{\mathbf{x}}-\mathbf{x_{true}}\\&=\mathbf{R}^{-1}\mathbf{A}^{\mathbf{T}}\mathbf{E}^{-1}\left(\mathbf{A}\cdot\mathbf{x_{true}}+\mathbf{e_y}\right)-\mathbf{x_{true}}\\&=\mathbf{R}^{-1}\mathbf{A}^{\mathbf{T}}\mathbf{E}^{-1}\mathbf{e_y}\end{aligned} \tag{5.9}$$

Arranging the covariance of estimation error $\mathbf{E_x}$ using Eq. (5.9), we found that the covariance of estimation errors was equal to $\mathbf{R}^{-1}$ .

$$\begin{aligned}\mathbf{E_x}&=\mathbf{e_x}\cdot\mathbf{e_x}^T\\&=\left(\mathbf{R}^{-1}\mathbf{A}^{\mathbf{T}}\mathbf{E}^{-1}\mathbf{e_y}\right)\cdot\left(\mathbf{R}^{-1}\mathbf{A}^{\mathbf{T}}\mathbf{E}^{-1}\mathbf{e_y}\right)^T\\&=\mathbf{R}^{-1}\mathbf{A}^{\mathbf{T}}\mathbf{E}^{-1}\mathbf{e_y}\mathbf{e_y}^T\left(\mathbf{E}^{-1}\right)^T A\left(\mathbf{R}^{-1}\right)^T\\&=\mathbf{R}^{-1}\mathbf{A}^{\mathbf{T}}\mathbf{E}^{-1}\mathbf{A}\mathbf{R}^{-1}\\&=\mathbf{R}^{-1}\mathbf{R}\mathbf{R}^{-1}\\&=\mathbf{R}^{-1}\end{aligned} \tag{5.10}$$

Now, if the "tolerance error" is defined as a consistent value with regard to the observation error, and the matrix $\mathbf{A}$ is normalized by the tolerance error, all eigenvalues of $\mathbf{E_x}$ may be near 1.0. Moreover, the maximum eigenvalue of $\mathbf{E_x}$ must be less than 1.0 in order to maintain the tolerance error for all unknown parameters. This is consistent with the fact that the minimum eigenvalue of $\mathbf{R}$ must be over 1.0.

If the tolerance error is defined inadequately, the eigenvalues of $\mathbf{E_x}$ will have various ordered values. Matrix $\mathbf{C}_k$ is termed as "generalized inverse," and it is expanded with the singular-value decomposition as follows.

$$\begin{aligned}&\mathbf{C}_k=\mathbf{V}\Lambda^{-1}\mathbf{W}^{\mathbf{T}}\\&\mathbf{V}=\left(v_1,v_2,\cdots,v_M\right)\quad\mathbf{W}=\left(w_1,w_2,\cdots,w_N\right)\end{aligned} \tag{5.11}$$

where $\mathbf{V}$ and $\mathbf{W}$ are normalized orthogonal basic matrixes, and $\Lambda^{-1}$ is written as

$$\Lambda^{-1} = \begin{bmatrix} \lambda_1^{-1} & & & & & \\ & \lambda_2^{-1} & & & 0 & \\ & & \ddots & & & \\ & & & \lambda_M^{-1} & & \\ & & & & 0 & \\ & 0 & & & & \ddots \\ & & & & & 0 \end{bmatrix}$$

$$(\lambda_1 > \lambda_2 > \cdots > \lambda_M) \qquad (5.12)$$

where $\lambda_1, \lambda_2, \cdots, \lambda_M$ are eigenvalues of matrix $\mathbf{R^{-1}}$, which is a symmetrical matrix because $\mathbf{R}$ is expressed by Eq. (5.1.2). The small eigenvalues may increase the observation error beyond the expected value when $\lambda_m / \lambda_1 \to 0.0$. The solution for such an ill-conditioned matrix is to examine the value $\lambda_m / \lambda_1$ (m<M) and to replace the smaller eigenvalues to zero, as $\lambda_i = 0\ (m < i < M)$.

## 5.1.3 CHANNEL SELECTION METHOD

Generally speaking, the solution of Eq. (5.7) is nonunique when the eigenvectors of matrix $\mathbf{A}$ are not orthogonal to each other. Let $\mathbf{A}$ be the set of sensitive increment vectors on radiation, which is normalized by the "tolerance error" described above.

$$\mathrm{A} = \frac{\partial \mathrm{y}}{\partial \mathrm{x}} = \left(\vec{\mathrm{a}}_1, \vec{\mathrm{a}}_2, \cdots, \vec{\mathrm{a}}_J\ \right)^{\mathrm{T}},$$

$$\vec{\mathrm{a}}_j = \left(a_{j,1}, a_{j,2}, \cdots, a_{j,M}\right) = \left(\frac{\partial \mathrm{y}_j}{\partial \mathrm{x}_1}, \frac{\partial \mathrm{y}_j}{\partial \mathrm{x}_2}, \cdots, \frac{\partial \mathrm{y}_j}{\partial \mathrm{x}_M}\right) \qquad (5.13)$$

$\partial \mathbf{x}_m$ : the target error of m - th parameter

Here, we should find the minimum number of channel sets under the condition that their eigencomponents are orthogonal to each other and the minimum eigenvalue of $\mathbf{R^{-1}}$ is above 1.0. However, this requires lengthy procedures to obtain the optimum channel sets (strict solution) because the number of combinations for channel sets is

$$\left|\{J\}\right| = 2^{N_{\max}} \qquad (5.14)$$

where $N_{\max}$ is the number of all observed channels ( over 50000 for the IMG). We have developed a method to obtain almost the proper number of channel sets with a reasonable number of steps. Below, we denote the outline of the operation flow to select the channels.

Step 1) Determine initial channel set J

$$\mathbf{A}_J = \left\{\mathbf{a}_1, \mathbf{a}_2, \cdots, \mathbf{a}_J\right\}$$

Step 2) Principal component analysis for

$$\mathbf{R}_J^{\mathbf{-1}} = (\mathbf{A}_J^{\mathbf{T}} \mathbf{E}_J^{-1} \mathbf{A}_J^{\mathbf{T}} + \mathbf{S}^{-1})^{-1}$$

$\left\{\lambda_{i,i=1,m}\right\}$ : eigen value, $(\lambda_1 > \lambda_2 > \cdots > \lambda_m > 0)$

$\left\{\upsilon_{i,i=1,m}\right\}$ : eigen vector

Step 3) If $\lambda_m > 1.0$, accomplish the selection.

Step 4) Select j, which gives the maximum value of

$$\left(\left(\mathbf{a}_j e_j^{-1}\right)^T \cdot \upsilon_m\right)^2, \ (\forall j \notin J)$$

$e_j$ : observation error for $j - th$ channel

Step 5) Join channel j to the channel set J

Step 6) Repeat step 1) ~ step 5) until end at step 3

As a prerequisite for these steps, we have to warrant that the minimum eigenvalue of $\mathbf{R^{-1}}$ is over 1.0 with all channels. This means that all unknown parameters can be retrieved within their tolerance errors using all channels.

At Step 4 , we adopted the evaluation function which involves some approximations. Theoretically, we can select j by the same evaluation as step 2 , but this requires eigenvalue analysis ($\mathrm{N_{max}}$-J) times. To serve computational resources, a interpretation is accepted as follows. The minimum eigenvalue which is less than 1.0 means that channel set J has insufficient number of the component $\upsilon_m$. An increase of the $\lambda_m$ due to adding channel j can be estimated as the power contained in the component. Thus, an appropriate channel set is selected by adding the channel which has the maximum norm for the minimum eigenvector until all eigenvalues are over 1.0.

## 5.1.4 PARAMETER REDUCTION METHOD

The same logic is applicable for the determination of parameters to be retrieved. The products for the Level 2 consist of 8 kinds of geophysical parameters for 54 layers. (See Section 5.1). But it was impossible to retrieve them keeping their tolerance errors, because we found that there were about 40~50 eigenvalues which were over 1.0 among about 400 eigenvalues. That is, we have 40~50 parameters to be retrieved at best, independently keeping their tolerance errors. Here, it is required to deduce the number of parameters so that all unknown parameters independently have sufficient accuracy. The adjacent parameters have to be merged for each geophysical parameter until all eigenvalues of covariance $\mathbf{E_x}$ become less than 1.0. A reasonable step for parameter merging is introduced.

Step 1) Assign 'minimum depth $D_{i,l}$ for each geophysical target i, (Temp., $H_2O$ etc.) ,

and Sub-layer l $(1 < l < 54)$ .

Initial value : $D_{i,l} = 1$

Step 2) Determine the boundary of the layer for the i-th target $\{L_i(k)\}_k$ , so that

$$D_{i,l} \le L_i(k) - L_i(k-1) \quad (\forall l : L_i(k-1) < l \le L_i(k))$$

where $L_i(k)$ is the maximum sub-layer number for k-th layer ( $1 < k < K_i$ )

Step 3) Combine each Jacobian element according to $L_i(k)$ .

$m$ is the total number of unknown parameters

$$\left\{\vec{\mathbf{a}}_{j,\{i,k\}}\right\}_{j=1,N} = \left\{ \sum_{l=L_i(k-1)+1}^{L_i(k)} a_{j,\{i,l\}} \right\}_{j=1,N} ,$$

$$m = \sum_i K_i$$

Step 4) Principal component Analysis for $\mathbf{R}_m^{-1} = (\mathbf{A}_m^{\mathbf{T}} \mathbf{E}^{-1} \mathbf{A}_m^{\mathbf{T}} + \mathbf{S}_m{}^{-1})^{-1}$

$\{\lambda_{i,i=1,m}\}$ : eigen value, $(\lambda_1 > \lambda_2 > \cdots > \lambda_m > 0)$

$\{\upsilon_{i,i=1,m}\}$ : eigen vector

Step 5) If $\lambda_m > 1.0$ , accomplish the deduction.

Step 6) Select i' and k', which gives the maximum value of $\left(\mathbf{a}^t \cdot \mathbf{A}_m \mathbf{E}^{-1} \upsilon_m\right)^2$

Step 7) Change $\{D_{i',l'}\}$

$$D_{i',l'} = \{L_{i'}(k) - L_{i'}(k-1)\} + 1 \quad (\forall l : L_{i'}(k-1) < l' \le L_{i'}(k))$$

Step 8) repeat step 2)~step 7) until end at step 4

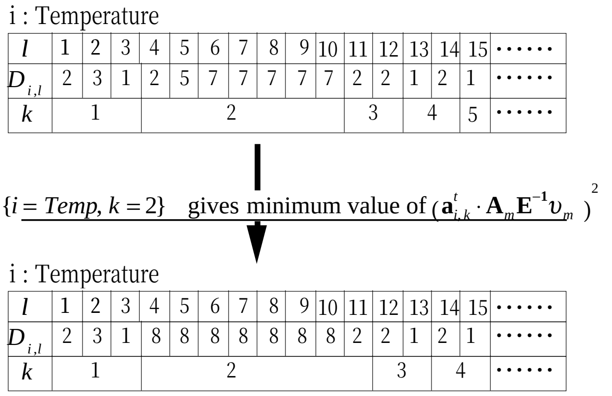

i : Temperature

| $l$ | 1 | 2 | 3 | 4 | 5 | 6 | 7 | 8 | 9 | 10 | 11 | 12 | 13 | 14 | 15 | …… |
|---|---|---|---|---|---|---|---|---|---|---|---|---|---|---|---|---|
| $D_{i,l}$ | 2 | 3 | 1 | 2 | 5 | 7 | 7 | 7 | 7 | 7 | 2 | 2 | 1 | 2 | 1 | …… |
| $k$ | 1 | | | 2 | | | | | | | 3 | | 4 | | 5 | …… |

$\{i = Temp, k = 2\}$ gives minimum value of $(\mathbf{a}_{i,k}^t \cdot \mathbf{A}_m \mathbf{E}^{-1} \upsilon_m)^2$

i : Temperature

| $l$ | 1 | 2 | 3 | 4 | 5 | 6 | 7 | 8 | 9 | 10 | 11 | 12 | 13 | 14 | 15 | …… |
|---|---|---|---|---|---|---|---|---|---|---|---|---|---|---|---|---|
| $D_{i,l}$ | 2 | 3 | 1 | 8 | 8 | 8 | 8 | 8 | 8 | 8 | 2 | 2 | 1 | 2 | 1 | …… |
| $k$ | 1 | | | 2 | | | | | | | | 3 | | 4 | | …… |

Fig. 5.1.4.1. Parameter reduction example.

## 5.2 FORWARD MODEL

The radiation at wavenumber w is given by Eq. (5.15) according to the radiative transfer equation.

$$I_W = B_W(t_s) \cdot Tr_{w,s} + \int B_W(t) \cdot \frac{Tr_w}{dy} dy \tag{5.15}$$

where $B_W(t)$ is the Planck function at temperature $t$ and $Tr_w$ is the transmittance at w . "s" in Eq (5.15) denotes 'surface'. $Tr_w$ is expressed with the optical depth $\tau_w$ , and $\tau_w$ is the product of the absorption coefficient $\sigma_w$ and atmospheric density $d$

$$Tr_w = \exp(-\tau_w), \quad \tau_w = \sigma_w \cdot d \tag{5.16}$$

In the forward model, it computes Eq. (5.15) by scattering pressure into 54 layers. $Tr_{w,l}$ is a transmittance function between the underside boundary of the l-th layer and the satellite.

$$I_W = B_W(t_s) \cdot Tr_{w,s} + \sum_{l=1}^{54} B_W(t_l) \cdot \Delta Tr_{w,l}$$

$$\Delta Tr_{w,s} = Tr_{w,l+1} - Tr_{w,l} \tag{5.17}$$

$Tr_w$ is mean transmittance between $\Delta w$, which is related to the spectral resolution, and is written as

$$Tr_{w,l} = \frac{1}{\Delta w}\int_{\Delta w} \exp(-\tau_{w,l})dw \tag{5.18}$$

where $\tau_{w,l}$ is the optical depth from l-th layer to the satellite, so that $\tau_{w,l}$ is arranged as a summation equation referring to Eq. (5.16)

$$\tau_{w,l} = \sum_{j=l}^{54}\sum_{i=1}^{8}\{\sigma_{w,j,i} \cdot d_{j,i}\} \tag{5.19}$$

where $\sigma_{w,l,i}$ and $d_{l,i}$ are, respectively, the absorption coefficient and column density of the i-th absorber at the pressure level l. In our forward model, eight main atmospheric constituents, $H_2O$, $CO_2$, $O_3$, $N_2O$, CO, $CH_4$, $HNO_3$ are considered, and the rest are included independently. The number of considered molecules is 8. The column density is independent on wave number.

## 5.2.1 RAPID CALCULATION

The absorption coefficient $\sigma$ can be calculated by a line-by-line method, but this requires enormous calculation time, hence a database of $\sigma$ is prepared.

The database of the absorption coefficient is prepared as described in section 5.3.3. FASCOD3P, which is one of the most widely used computer codes developed by Geophysics Directorate, Phillips Laboratory, Hanscom Air Force Base, is used to calculate the absorption cross section. HITRAN 1992 database was used for line parameter information. The treatment of the Voigt line shape in FASCOD3P is based on a linear combination of approximating functions. The characteristics of the database are tabulated in Table 5.2.1.

The shape of $\sigma$ is so complicated that approximation by a quadratic curve is adopted with short wavenumber intervals.

Now, the interval $\Delta w$ in Eq (5.18) is expressed as the total of the spectral narrow intervals $\Delta w'_k$, where $\sigma$ can be approximated by a quadratic curve,

$$\Delta w = \sum_{k=1}^{K} \Delta w'_k \tag{5.20}$$

$$\sigma_{k,i,l} = a_{k,i,l}w'^2 + b_{k,i,l}w' + c_{k,i,l} \quad (w' < \Delta w'_k) \tag{5.21}$$

Table 5.2.1. The characteristics of database of absorption coefficient.

| Contents | Sets of coefficients for quadratic curve. |
|---|---|
| wave number range | 710 - 3030 $cm^{-1}$ |
| atmospheric constituents | $H_2O$, $CO_2$, $O_3$, $N_2O$, CO, $CH_4$, $HNO_3$, and the rest |
| pressure range | 1013 -0.1 hPa (See Table) |
| Temperature range | 160 K -330 K |
| approximation interval | 5 K for temperature 0.1 $cm^{-1}$/32 (minimum interval) for wavenumber |
| volume | 17 GB (all region)4 GB<br>(Selected 4000 channels) |
| Searching key | temperature, pressure, wavenumber, gas |
| Resources | Spectral line parameters : HITRAN 1992Cross section calculator : FASCOD3P |

then, Eq. (5.18) is expanded as

$$
\begin{aligned}
Tr_{w,l} &= \frac{1}{\Delta w}\int_{\Delta w} \exp\left(-\tau_{w,l}\right)dw \\
&= \frac{1}{\Delta w}\sum_{k=1}^{K}\left\{\int_{\Delta w_k} \exp\left(-\tau_{k,l,}\right)dw\right\}
\end{aligned}
\tag{5.22}
$$

Also, Eq. (5.19) is rewritten as

$$
\begin{aligned}
\tau_{k,l,} &= \sum_{j=l}^{54}\sum_{i=1}^{8}\left\{\sigma_{k,j,i}\cdot d_{j,i}\right\} \\
&= \sum_{j=l}^{54}\sum_{i=1}^{8}\left\{(a_{j,i}w'^2 + b_{j,i}w' + c_{,j,i})\cdot d_{j,i}\right\}
\end{aligned}
\tag{5.23}
$$

Here, a, b, and c are defined newly as follows,

$$
\begin{aligned}
a_{j,l} &\equiv \sum_{j=l}^{54}\sum_{i=1}^{8} a_{j,i}d_{j,i}, \\
b_{j,l} &\equiv \sum_{j=l}^{54}\sum_{i=1}^{8} b_{j,i}d_{j,i}, \\
c_{j,l} &\equiv \sum_{j=l}^{54}\sum_{i=1}^{8} c_{j,i}d_{j,i}
\end{aligned}
\tag{5.24}
$$

then,

$$
\begin{aligned}
Tr_{w,l} &= \frac{1}{\Delta w}\int_{\Delta w} \exp\left(-\tau_{w,l}\right)dw \\
&= \frac{1}{\Delta w}\sum_{k=1}^{K}\left\{\int_{\Delta w_k} \exp\left(-\tau_{k,l,}\right)dw\right\} \\
&= \frac{1}{\Delta w}\sum_{k=1}^{K}\left\{\int_{\Delta w_k} \exp\left(-a_{k,l}w'^2 - b_{k,l}w' - c_{k,l}\right)dw'\right\}
\end{aligned}
\tag{5.25}
$$

In order to calculate the next reformed integral,

$$
\begin{aligned}
F &\equiv \int_{w_2}^{w_1} \exp\left(-aw^2 - bw - c\right)dw \\
&= \int_0^{w_1-w_2} \exp\left(-aw'^2 - bw' - c\right)dw'
\end{aligned}
\tag{5.26}
$$

we classified the coefficients into three cases to reduce the calculation time using error function.

case (a>0) :

$$
\begin{aligned}
F &= \frac{\sqrt{\pi}\exp\left(\frac{b}{4a} - c\right)}{2\sqrt{a}} \\
&\cdot\left\{erf\left(\sqrt{a}(w_1 - w_2) + \frac{b}{2\sqrt{a}}\right) - erf\left(\frac{b}{2\sqrt{a}}\right)\right\}
\end{aligned}
\tag{5.27}
$$

where, erf(x) is error function as follows

$$
erf(x) = \frac{2}{\sqrt{\pi}}\int_0^{\infty} e^{-t^2}dt \tag{5.28}
$$

When x is large enough, the complementary error function is used.

$$
erfc(x) = 1 - erf(x) = \frac{2}{\sqrt{\pi}}\int_x^{\infty} e^{-t^2}dt \tag{5.29}
$$

case (a=0 and b!=0) :

$$
\begin{aligned}
F &= \int_0^{w_1-w_2} \exp\left(-bw' - c\right)dw' \\
&= \frac{\exp(-c)}{b}\left\{1 - \exp\left(-b(w_1 - w_2)\right)\right\}
\end{aligned}
\tag{5.30}
$$

case (a=0 and b=0 ):

$$
F = \int_0^{w_1-w_2} \exp(-c)dw' = \exp(-c)(w_1 - w_2) \tag{5.31}
$$

case (a<0):

In this case, the square root of Eq. (2.27) is impossible to calculate, hence some replacement steps are performed.

$$
\begin{aligned}
&-aw'^2 - bw' - c = u^2 - 2xu - c \\
&y = \sqrt{a} \\
&x = b/2y \\
&u = y\cdot w' \\
&du = y\cdot dw'
\end{aligned}
\tag{5.32}
$$

As a conclusion, Eq. (5.27) can be rewritten as Eq. (5.33) using complex error function.

$$
\begin{aligned}
F &= \frac{1}{y}\int_0^{y(w_1-w_2)} \exp(\quad u^2 - 2xu - c)du \\
&= \frac{1}{y\cdot\exp(x^2+c)}\left\{ erfi(x) - erfi\left(x - y(w_1-w_2)\right)\right\} \\
&= \frac{1}{y\cdot\exp(c)} \\
&\cdot\left\{ erfi1(x) - \exp\left(-2xy(w_1-w_2) + y^2(w_1-w_2)^2\right)\cdot erfi1\left(x - y(w_1-w_2)\right)\right\}
\end{aligned}
\tag{5.33}
$$

$$
\begin{aligned}
erfi(x) &= \int_0^x \exp(t^2)dt \\
erfi1(x) &= \exp(-x^2)erfi(x)
\end{aligned}
\tag{5.34}
$$

## 5.2.2 DATABASE OF THE ABSORPTION CROSS SECTION

The database of absorption cross sections is required to represent the shapes of the absorption coefficients accurately, and should be of a reasonable size. The absorption coefficient of a molecule is dependent on temperature and pressure. In the forward model, it is applied with 54 pressure levels and 8 molecules, but it is required to represent the continuous function of temperature and wavenumber. Therefore, the absorption coefficient is calculated at the l-th pressure level for the i-th molecule, and then, it is approximated with a quadratic curve with the direction of temperature and wavenumber.

First , the absorption coefficient was modified by an approximation along the wave number. Each with a 0.1 $cm^{-1}$ pitch is approximated into a quadratic curve. In case this accumulated error is estimated to be large, the 0.1 $cm^{-1}$ pitch is divided into 0.1 $cm^{-1}/2$ and approximated again to reduce this error. If 1/2 (0.1 $cm^{-1}$) is not enough, this division of pitch is repeated into 1/4 (0.1 $cm^{-1}$), 1/8 (0.1 $cm^{-1}$) … to satisfy accuracy requirements. Thus, sufficient accuracy is obtained. This method accomplishes detailed sampling in a complicated structure region and rough sampling in a simple structure region.

Next, we use the same approximation at temperatures t, t+2.5 , t+5.0 in the wave number range. It is possible to change the direction from wave number to temperature. The approximation interval of 5 K is sufficient to represent it by a quadratic curve without loosing accuracy.

$$
\begin{aligned}
\sigma_t(w) &= a_t w^2 + b_t w + c_t \\
\sigma_{t+2.5}(w) &= a_{t+2.5} w^2 + b_{t+2.5} w + c_{t+2.5} \\
\sigma_{t+5.0}(w) &= a_{t+5.0} w^2 + b_{t+5.0} w + c_{t+5.0}
\end{aligned}
\tag{5.35}
$$

At the end point of the approximation, at the minimum point of the three values, these coefficients can be changed to coefficients along the temperature direction as follows.

$$
\begin{aligned}
a'_{\text{at w=w}_\text{n}} &= \frac{\sigma_{t+5.0}(w) - 2\sigma_{t+2.5}(w) + \sigma_t(w)}{2\Delta_t^2} \\
b'_{\text{at w=w}_\text{n}} &= \frac{\sigma_{t+2.5}(w) - \sigma_t(w)}{\Delta_t} - a_w\Delta_t \\
c'_{\text{at w=w}_\text{n}} &= \sigma_t(w)
\end{aligned}
\tag{5.36}
$$

where, $\Delta_t = \frac{(t+5.0)-t}{2} = 2.5$ .

At all the end and middle points on the wavenumber, coefficient sets (,,) are calculated, and are stored into the database. Also, information of sampling points on wavenumber is stored in the database considering the access to the database and size of the database. This approximation is performed for each pressure and each molecule, covering the IMG spectral range and possible temperatures.

## 5.2.3 DIFFERENTIAL CALCULUS

From Eq. (5.17), differentiation of $I_W$ with respect to the mixing ratio for the i-th geophysical parameter is expressed as

$$
\begin{aligned}
\frac{\partial I_W}{\partial p_l} &= \frac{\partial \tau_{w,l}}{\partial p_l}\frac{\partial}{\partial \tau_{w,l}}\left( B_W(t_s)Tr_{w,s} + \sum_{l=1}^{54} B_W(t_l)\Delta Tr_{w,l} \right) \\
&= B_W(t_s)\frac{\partial \tau_{w,l}}{\partial p_l}\frac{\partial Tr_{w,s}}{\partial \tau_{w,l}} + \sum_{l=1}^{54} B_W(t_l)\frac{\partial \tau_{w,l}}{\partial p_l}\frac{\partial \Delta Tr_{w,l}}{\partial \tau_{w,l}}
\end{aligned}
$$

For the temperature, the differential equation is given as

$$
\frac{\partial I_W}{\partial t_l} = \frac{\partial B_W(t_l)}{\partial p_l}\cdot \Delta Tr_{w,l}
$$

## 5.3 IMPLEMENTATION OF RETRIEVAL ALGORITHM

The level 2 outputs have 8 types of geophysical parameters, that is, temperature and 7 kinds of green house gases ($H_2O$, $CO_2$, $O_3$, $N_2O$, CO, $CH_4$, and $HNO_3$), for 54 pressure levels and surface temperature. Each of the pressure levels and corresponding heights are tabulated in Table 5.3.1.

### 5.3.1 CHANNELS AND PARAMETERS

4000 channels and 33 parameters were employed and used for retrieval . They were determined as a result of channel selection and parameter reduction based on the theory in Section 5.1.3.

The Jacobian matrix $\mathbf{A}$ was calculated by the method of numerical differences using the forward model, with all the parameters and channels in band 2 and band 3. The channels in band 1 were not considered because it was assumed that there would be relative noise on the spectra in band 1. Therefore, an N value of above 40000 and an M value of above 400 were entered in Eq. (5.1) at the beginning of channel selection and parameter reduction. The profile for selection was based on the U.S. standard model 1976, and radiative spectra were calculated by the forward model with scanning function rectangle (HWFM: 0.05 $cm^{-1}$ ).

The eigenvalue analysis was performed on matrix $\mathbf{Q}$ instead of matrix $\mathbf{R}^{-1}$ because matrix $\mathbf{S}$ , which is contained in matrix $\mathbf{R}^{-1}$ , was affective to the error estimation and we could not define $\mathbf{S}$ strictly. To consider matrix $\mathbf{Q}$ was to consider the estimation error based on the least squares method.

$\mathbf{E}$ can be written as a diagonal matrix, and each diagonal element was defined as (NESR)**2 + (Stability)**2 .

First, the tolerance errors were set for each geophysical parameter. For the i-th geophysical parameter, the total of diagonal elements of matrix $\mathbf{Q}$ is equal to the total of eigenvalues of matrix $\mathbf{Q}$ .

$$\sum_{l}^{54} diag\{Q\}_i \ge h \Leftrightarrow \sum_{i}^{54} \lambda_{i,l} \ge h \qquad (5.39)$$

Strictly speaking, h=1.0 is sufficient to retrieve the i-th geophysical parameter with 1 parameter using all channels, However, we secured a surplus of channel selections as h=2.0. Some tolerance errors were changed as a result of the investigation, and finally, the tolerance errors were defined as in Table 5.3.1.1.

Second, the analytical parameters were determined, considering both the result of parameter reduction and users' requests. After the parameter reduction, which was based on Section 2.2.3, some parameters were changed because of users' requests. Finally, the unknown parameters were defined as in Table 5.3.1.2 though the result of eigenvalue analysis reveals that one can retrieve with only 1 parameter for $CO_2$ and 2 parameters for CO. These analytical parameters are finally expanded for 54 pressure levels.

Table 5.3.1. Pressure level for L2 data

| No. | Press. | Alt. | No. | Press. | Alt. | No. | Press. | Alt. | No. | Press. | Alt. | No. | Press. | Alt. |
|---|---|---|---|---|---|---|---|---|---|---|---|---|---|---|
| | (hPa) | (km) | | (hPa) | (km) | | (hPa) | (km) | | (hPa) | (km) | | (hPa) | (km) |
| 1 | 1013 | 0.00 | 12 | 666 | 3.40 | 23 | 325 | 8.64 | 34 | 137 | 14.22 | 45 | 30 | 23.94 |
| 2 | 975 | 0.33 | 13 | 632 | 3.81 | 24 | 300 | 9.18 | 35 | 125 | 14.80 | 46 | 25 | 25.13 |
| 3 | 937 | 0.66 | 14 | 600 | 4.21 | 25 | 275 | 9.76 | 36 | 112 | 15.50 | 47 | 20 | 26.57 |
| 4 | 900 | 0.99 | 15 | 566 | 4.65 | 26 | 250 | 10.38 | 37 | 100 | 16.22 | 48 | 15 | 28.54 |
| 5 | 875 | 1.22 | 16 | 532 | 5.12 | 27 | 233 | 10.83 | 38 | 90 | 16.89 | 49 | 10 | 31.07 |
| 6 | 850 | 1.46 | 17 | 500 | 5.58 | 28 | 216 | 11.32 | 39 | 80 | 17.64 | 50 | 7 | 33.47 |
| 7 | 825 | 1.70 | 18 | 465 | 6.11 | 29 | 200 | 11.81 | 40 | 70 | 18.50 | 51 | 5 | 36.11 |
| 8 | 800 | 1.95 | 19 | 432 | 6.65 | 30 | 187 | 12.23 | 41 | 60 | 19.48 | 52 | 3 | 39.69 |
| 9 | 766 | 2.30 | 20 | 400 | 7.19 | 31 | 175 | 12.66 | 42 | 50 | 20.64 | 53 | 1 | 48.19 |
| 10 | 733 | 2.65 | 21 | 375 | 7.65 | 32 | 162 | 13.15 | 43 | 40 | 22.08 | 54 | 0.1 | 65.59 |
| 11 | 700 | 3.01 | 22 | 350 | 8.13 | 33 | 150 | 13.64 | 44 | 35 | 22.94 | | | |

Table 5.3.1.1. tolerance error. For O3, the tolerance error depends on altitude.

| parameter | target error | parameter | target error |
|---|---|---|---|
| Surface Temp | 1 K | $N_2O$ | 10 % |
| Temperature | 1 K | CO | 10 % |
| $H_2O$ | 10 %of satulated water (troposphere)<br>10 % (stratosphere) | $CH_4$ | 10 % |
| $CO_2$ | 2 % | $HNO_3$ | 20 % |
| $O_3$ | 2 - 20 % | | |

Table 5.3.1.2. Analytical parameters

| parameter | | | pressure | | | | | | | | | |
|---|---|---|---|---|---|---|---|---|---|---|---|---|
| Temp | 10 | (Pres.) | 1013 | 850 | 700 | 600 | 500 | 400 | 250 | 150 | 50 | 10 |
| | | (Alt.) | 0.0 | 1.5 | 3.0 | 4.2 | 5.6 | 7.2 | 10.4 | 13.6 | 20.6 | 31.1 |
| | | (LayerNo.) | 1 | 6 | 11 | 14 | 17 | 20 | 26 | 33 | 42 | 49 |
| $H_2O$ | 5 | (Pres.) | 1013 | | 850 | | 700 | | 500 | | | 200 |
| | | (Alt.) | 0.0 | | 1.5 | | 3.0 | | 5.6 | | | 11.8 |
| | | (LayerNo.) | 1 | | 6 | | 11 | | 17 | | | 29 |
| $CO_2$,<br>$N_2O$,<br>CO,$CH_4$ | 3 | (Pres.) | 1013 | | | | 500 | | | | 200 | |
| | | (Alt.) | 0.0 | | | | 5.6 | | | | 11.8 | |
| | | (LayerNo.) | 1 | | | | 17 | | | | 29 | |
| $O_3$ | 3 | (Pres.) | 1013 | | | | 300 | | | | 100 | |
| | | (Alt.) | 0.0 | | | | 9.2 | | | | 16.2 | |
| | | (LayerNo.) | 1 | | | | 24 | | | | 37 | |
| $HNO_3$ | 1 | | | | | | | | | | | |

Next, the channel selection was performed. At the judging step of which channel should be added, computational time for forward calculation was considered as a penalty.

$$\left(\left(\mathbf{a}_j e_j^{-1}\right)^T \cdot \upsilon_m\right)^2 / Time_j \tag{5.40}$$

Actually, 5 eigenvalues remained under 1.0 when 4000 channels were selected, but it was concluded that the extent of the damage was small. The selected channels are shown in Fig 5.3.1.1.

## 5.3.2 INITIAL PROFILE AND ITS COVARIANCE

For climatic parameters such as temperature (15 pressure levels), $H_2O$ (15 pressure levels), surface temperature and surface pressure, ECMWF (European Center for Medium-range Weather Forecasts) 1992 data were used to calculate the covariance of the initial profiles, however, the objective analysis data from the Japan meteorological agency (JMA) were used for the initial guesses of the final retrieval version.

Since, sampling data are 2.5*2.5 meshed in latitude by longitude and are obtained 4 times per day, the number of analysis targets reached is 144*73*4*365. We accomplished 785 classification using eigenvalue analysis.. The mapping keys are

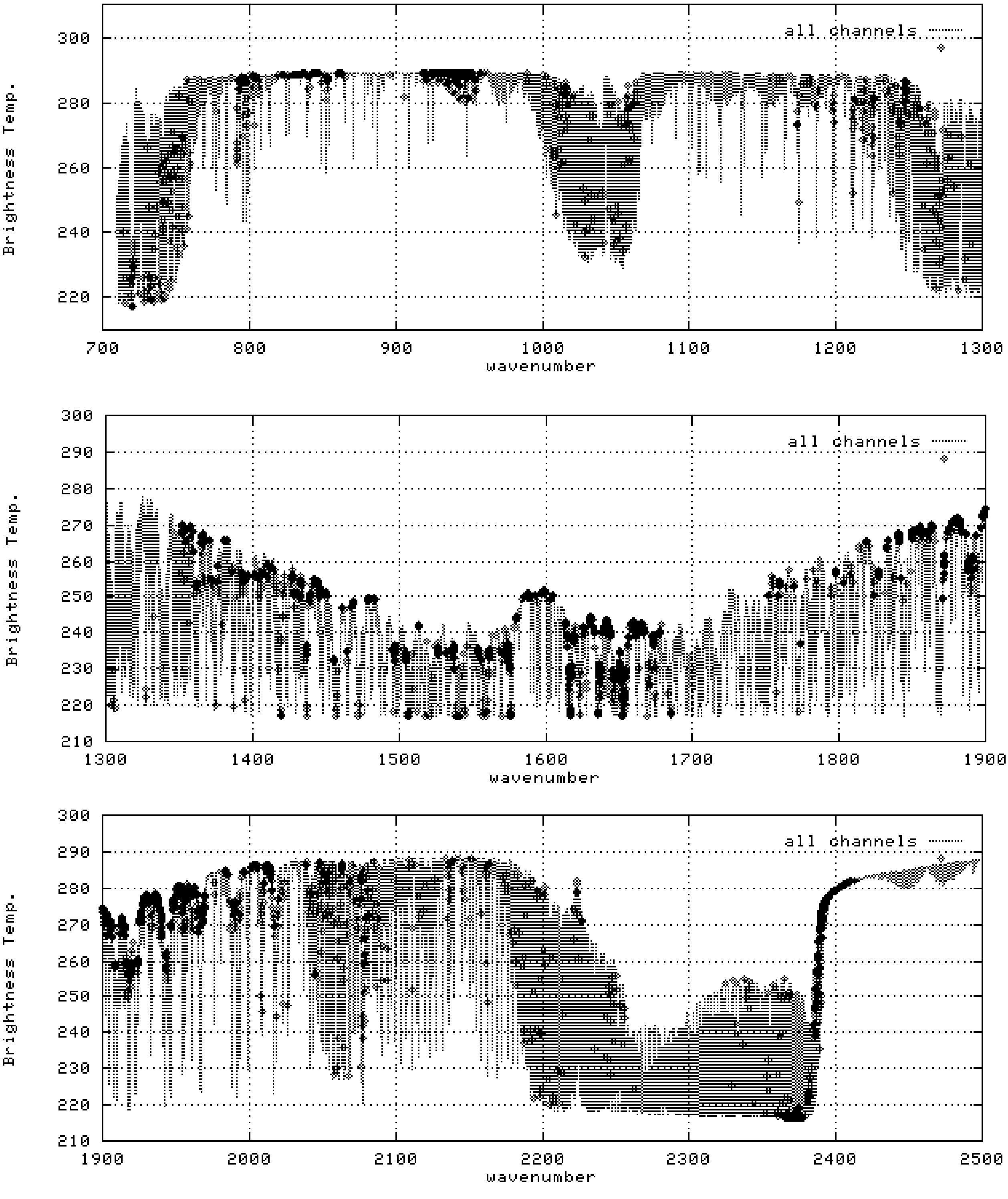

Fig 5.3.1.1. Selected 4000 channels (pointed out on the all channels)

the observed month, time and observed latitude and longitude. For other trace gases, only one profile which was derived from U.S. standard 1976 was used throughout.

Matrix $\mathbf{S}$ is expressed as

$$\mathbf{S} = \begin{bmatrix} \left\{ \mathbf{S}^{\mathbf{ps,ts,temp,H_2O}} \right\}_{k,k=1,785} & \mathbf{0} \\ \mathbf{0} & diag(\mathbf{S}^i) \end{bmatrix} \tag{5.41}$$

where, $\mathbf{S}^{\mathbf{ps,ts,temp,H_2O}}$ is a covariance matrix obtained as a pair of $\mathbf{x}_0$, and $\mathbf{S}^i$ is a covariance matrix for the i-th geophysical parameter excluded temperature, $H_2O$, Ts, and Ps. $\mathbf{S}^i$ is determined as

$$\mathbf{S}^i = diag\{a\} \tag{5.42}$$

where a=10. This means that the volume of the trace gas has a standard deviation of 3 times the tolerance error when entire matrix is normalized by each tolerance error. In order to strengthen the restriction between pressure levels, we improved $\mathbf{S}^i$ as

$$\mathbf{S}^i = \left\{ s^i_{n,m} \right\} = a_i \exp\left( \frac{-(n-m)^2}{b_i} \right) \tag{5.43}$$

in the latter version of the algorithm. Where root of $a_i$ is the standard deviation, and n and m are the numbers for pressure levels. It makes restraint between pressure levels stronger.

The matrix $\mathbf{A}$ and $\mathbf{y_0} = f(\mathbf{x_0})$ could be stored in the database in advance.

### 5.3.3 JACOBIAN MATRIX

Two approaches were attempted to make a Jacobian matrix, the method of differentiation and the method of numerical differences. In the beginning , the latter method was adopted. Its elements are expressed as

$$a_{i,j} = \frac{\partial f_i(\mathbf{x_0})}{\partial \mathbf{x}_j} = f_i(\mathbf{x_0} + \partial \mathbf{x}_j) - f_i(\mathbf{x_0}) \tag{5.44}$$

where, $\partial \mathbf{x}_j$ is the tolerance error of the j-th unknown parameter (Table 5.2.1).

It is difficult to remake the matrix for every iteration because this method needs forward calculation (N+1) times, hence we improved the forward program to obtain the differential semi-analytically, which is explained in Section 2.3.4.

### 5.3.4 ERROR COVARIANCE MATRIX

E matrix is a diagonal matrix, and its diagonal elements are designed as

$$\begin{aligned} diag(\mathrm{E}) &= (NESR)^2 + (stability)^2 \\ &+ (forward - \mathrm{mod}\, el\ error)^2 \\ &+ (water\ nonlinearity)^2 \end{aligned} \tag{5.45}$$

The NESR and Stability values had been announced by the IMG-sensor team, and the values were updated in the retrieval version 3.0, which are the results of testing in orbit after the launch. The radiance error due to the uncertainty in modeling has not been estimated yet, so it is determined by taking the difference in radiance between the calculation using the database which is developed for data-processing and the calculation using a more detailed database (this needs greater computing time). Their values are larger at near 700 $cm^{-1}$ and at the water continuum region.

The radiance error due to nonlinearity is determined by water nonlinearity according to

$$\begin{aligned} &(Water\ NonLinearity)^2 \\ &= \left( \left\{ \mathrm{A}_{water} \cdot \partial \mathrm{x}_{\mathrm{water}} \right\} - \left\{ f(\mathrm{x}_0 + \partial \mathrm{x}_{\mathrm{water}}) - f(\mathrm{x}_0) \right\} \right)^2 \end{aligned} \tag{5.46}$$

where, $\mathbf{A}_{water}$ is Jacobian matrix for water, and $\partial \mathbf{x}_{\mathbf{water}}$ is differential of water .

### 5.3.5 ERROR ANALYSIS

As stated in Section 5.1.2, $\mathbf{R}^{-1}$ shows the covariance matrix of the estimation error. Using the maximum likelihood method, target $\mathbf{x}$ is assumed to distribute with multivariate Gaussian distribution with average $\mathbf{x_0}$, and its covariance $\mathbf{S}$. After observation, the posterior probability distribution of $\mathbf{x}$ is also changed to the Gaussian distribution, of which the average is $\hat{\mathbf{x}}$ and covariance is $\mathbf{R}^{-1}$.

The dimension of $\mathbf{R}^{-1}$ is the number of variable parameters, and the square roots of its diagonal elements can be recognized as 1-sigma of analysis. $\mathbf{R}^{-1}$ is calculated for each Jacobian matrix, so that the same number of $\mathbf{R}^{-1}$ as prepared in the initial profile $\mathbf{x_0}$ is calculated. Table 5.3.5.1 shows their average values.

To satisfy the condition of tolerance error, we performed the channel selection and the number reduction of parameters, however, the error was

Table 5.3.5.1. Analysis error. The error bar unit for temperature is K, and for the othes is %. For $H_2O$, the error bar unit is % of saturated water volume.

| Parameters | Error Bar | Parameters | Error Bar |
|---|---|---|---|
| Ts | 0.03 | $CO_2$ (1000hPa) | 6.03 |
| Temp (1000hPa) | 1.83 | $CO_2$ (500hPa) | 3.93 |
| Temp (850hPa) | 1.27 | $CO_2$ (200hPa) | 3.09 |
| Temp (700hPa) | 0.93 | $O_3$ (1000hPa) | 28.72 |
| Temp (600hPa) | 0.51 | $O_3$ (300hPa) | 3.70 |
| Temp (500hPa) | 0.82 | $O_3$ (100hPa) | 9.51 |
| Temp (400hPa) | 0.94 | $N_2O$ (1000hPa) | 28.59 |
| Temp (250hPa) | 1.23 | $N_2O$ (500hPa) | 14.08 |
| Temp (150hPa) | 1.20 | $N_2O$ (200hPa) | 9.04 |
| Temp (50hPa) | 0.89 | CO (500hPa) | 29.95 |
| Temp (10hPa) | 0.57 | CO (1000hPa) | 16.53 |
| $H_2O$ (1000hPa) | 25.44 | CO (200hPa) | 20.42 |
| $H_2O$ (850hPa) | 18.32 | $CH_4$ (1000hPa) | 30.13 |
| $H_2O$ (700hPa) | 13.91 | $CH_4$ (500hPa) | 14.36 |
| $H_2O$ (500hPa) | 10.37 | $CH_4$ (200hPa) | 11.21 |
| $H_2O$ (200hPa) | 10.26 | $HNO_3$ | 57.78 |

increased. One of the reasons for that could be that the channel selection and parameter reduction were performed for only one profile. It should be noted that the forward model error was not estimated, and, the accuracy of the initial guess was ignored here, also, the effect of iteration should have been included.

## 5.3.6 ALGORITHM OPTIMIZATION AFTER SENSOR EVALUATION

After IMG hardware evaluation, we updated the retrieval process parameters using the results of the evaluated hardware characteristics. The initial guesses were provided using the objective analysis data from the Japan Meteorological Agency. It may be closer to the true target. Other optimizations were introduced as follows:

(1) Spectral resolution:
The spectral resolution of band 3 reveals that the spectral resolution was degraded in proportion to their wavenumber. As previously mentioned, it was caused by the arrangement of detectors. Since a rectangular window was used in the L1-processing, sin(x)/x line shape should be applied for smoothing in the spectral domain. Hence this function requires long wing calculation since the shape is wide-based. We managed to fit by smoothing, using the Gaussian function for the calculated spectra by the forward model. In order to obtain the radiance of one channel with Gaussian smoothing, the radiances of 5 neighboring channels are required. Table 5.3.6.1 shows the smoothing width.

(2) E matrix:
For the E matrix used in the retrieval process, the data source of NESR and stability values are updated to calculate the E matrix.

(3) Jacobian matrix:
The Jacobian matrix was changed from the numerical differential method to the analytical differential method.

(4) Selected channel number:
Since L1-spectra involved some error near 860 cm-1 which was caused by the vibration of the hardware, some spectra with serious error were removed from selected channels, and 3821 channels were used for the retrieval.

(5) Adopting the iteration:
Retrieval is performed according to Eq. (2.1.5). The basic structure of the analysis is shown in Fig. 5.3.2. Two iterations (that is, 3 times of inversion) were performed, and the Jacobian matrix and the radiance were replaced at each iteration.

## 5.4 CLOUD DETECTION USING OCTS

For quality control of the data, we had intended to detect the cloud covered surfaces. As previously mentioned, the cloud information can be obtained from the OCTS (ocean color and temperature sensor, on board the ADEOS as an IMG) or the IMG spectrum itself.

Table 5.3.6.1. Smoothing parameters for the forward model adapting the evaluated IMG wavenumber resolution.

|  | band 3 |  |  |  | band 2 |
|---|---|---|---|---|---|
| wavenumber (cm-1) | ~ 1000 | ~ 1300 | ~ 1600 | ~ 2000 | ~ 2000 |
| 1/e width (cm-1) | 0.077 | 0.098 | 0.121 | 0.147 | 0.050 |

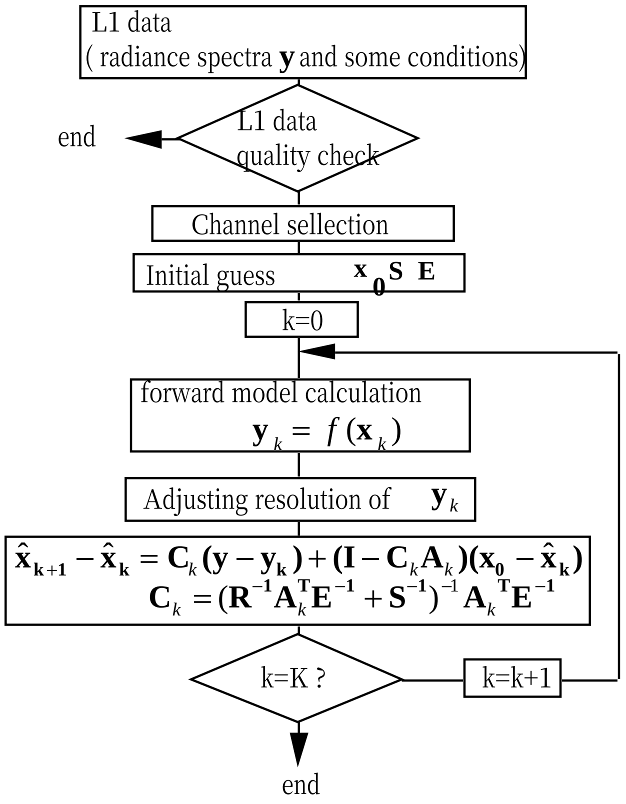

Fig. 5.3.2. Basic structure of analysis.

The OCTS observes the earth surface in the visible-infrared bands via 12 channels detector arrays. Each array consists of 10 pixels, and each cell corresponds to 700 m resolution at the surface, and the swath of the OCTS covers the IMG observation area at the surface simultaneously. The main objective of the OCTS was the observation of ocean color as the name of the sensor indicates, and, the gain setting of the sensor was accommodated to the sea surface layer observations. Because the radiation from the sea surface layer is very weak, and the gain settings of the OCTS was adjusted for the ocean colour monitoring, the observation of the clouds and the land surface introduced the output saturation of the detectors. Our goal was to detect clouds, and to distinguish between clouds and the snow / ice capped surface, however, the saturated data resulted in the deterioration of the developed cloud detection system performance. There was a plan to operate the OCTS in the land mode where the lower gain settings adapted to the land observations. Using the OCTS land mode data, we intended to develop the cloud detection algorithm from the IMG spectra themselves, comparing the output from the cloud detection system with the IMG spectra. Unfortunately, because the ADEOS operation was ceased due to the failure, this plan was aborted.

Table 5.4.1 shows the observation wavelength of the OCTS. The developed cloud detection program used several channels of the OCTS. The last version (ver. 2. 1) used ch 1, 5, 7, 9, 11, and 12. This program was designed to distinguish the observed area between the clouds and the snow, and to distinguish between higher and lower lying clouds. Figure 5.4.1 shows the diagram of the final version cloud discrimination algorithm. The cloud detection program was applied to each of 16 by 16 pixels corresponding to the foot print of the IMG, of 8 by 8 km.

Table 5.4.1. OCTS observation wavelength.

| channel number | center wavelengthor wavelength width($\mu$m) | band width (nm) | S/N, NEDT |
|---|---|---|---|
| 1 | 0.412 | 20 | 450 |
| 2 | 0.443 | 20 | 500 |
| 3 | 0.490 | 20 | 500 |
| 4 | 0.520 | 20 | 500 |
| 5 | 0.565 | 20 | 500 |
| 6 | 0.670 | 20 | 500 |
| 7 | 0.765 | 40 | 500 |
| 8 | 0.865 | 40 | 450 |
| 9 | 3.55 - 3.88 | - | 0.15 K |
| 10 | 8.25 - 8.80 | - | 0.15 K |
| 11 | 10.3 - 11.4 | - | 0.15 K |
| 12 | 11.4 - 12.7 | - | 0.20 K |

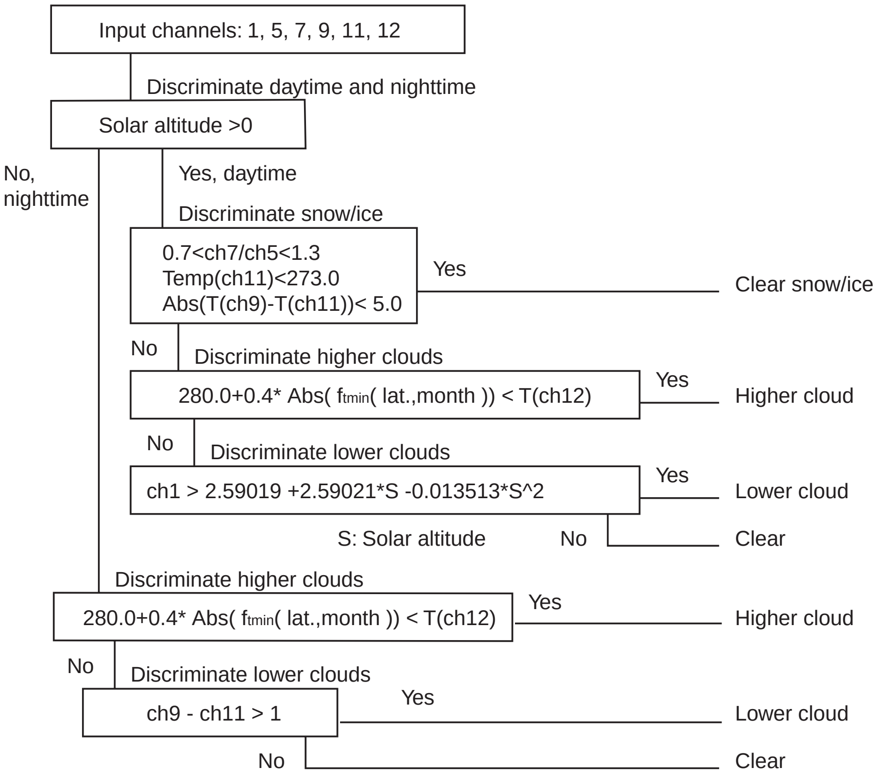

Fig. 5.4.1. Diagram of the cloud discrimination algorithm. In the figure, T indicates the radiance temperature, S the solar altitude, and ftmin a function for estimating the minimum surface temperature using the latitude and the observation month point and date. The radiance temperature of each channel was obtained from the digital-number/temperature tables provided by NASDA.

# 6. GROUND SEGMENT DEVELOPMENT AND OPERATION

The ground design of the IMG data and information system (IMGDIS) was drawn up in December, 1993, and it took three years to begin the operation.

## 6.1 DESIGN POLICY

The objectives of the IMGDIS were to process the IMG data and to distribute the products to users. The system was required not only to analyze the IMG data, but also to accept the reprocessing requirements of the data corresponding to the analysis algorithm enhancement during the IMG operating years. The future requirements of reprocessing are uncertain, and, to prepare a marginal computing resource may not be cost effective, in general.

The IMGDIS was designed as a distributed parallel processing system consisting of thirty UNIX workstations in 1996, and the workstations were connected by a fiber distributed data interface (FDDI) network. Figure 6.1.1 shows the outline of the IMGDIS hardware. The application software installed in the IMGDIS was modularized using the originally developed middle-ware to accomplish a flexible and open-ended software system on this parallel computer cluster. The developed IMGDIS achieved, (1) real time computation power: it could execute, 72 times 130 k-points FFT and the retrieval process for the 2 k-points spectral bins data per 10 seconds in a total of 30 GB data per day, (2) flexibility of computation: the application programs were encapsulated from the computation servers, (3) one-man operation: the IMGDIS was operated automatically and one operator could monitor and control the system including the media exchange.

The IMGDIS was developed based on the server-client model. All the jobs such as the Fourier transform processes and/or retrieval processes are composed of client applications and the job container services (JCS) which are provided by the job container server. Each job reads the input data from a data node service (DNS) and outputs the processed data to another node service, and the jobs are monitored by the execution control function (ECF). The ECF executes the jobs following the IMDIS operation plan defined by the operator. The client applications are distributed to the computer cluster by the distribution control function (DCF). The DCF controls the computer cluster arrangement adapting the characteristics of the job. In the case of the job

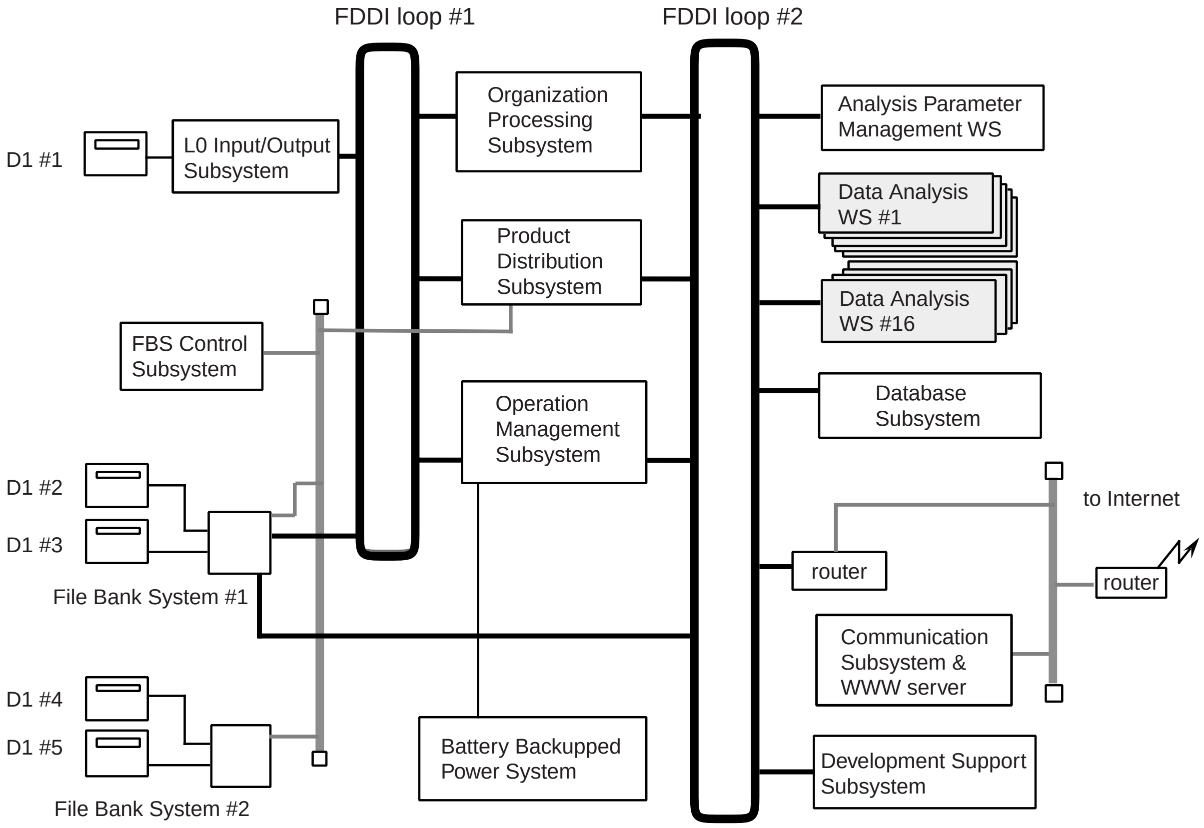

Fig. 6.1.1. IMGDIS hardware configuration.

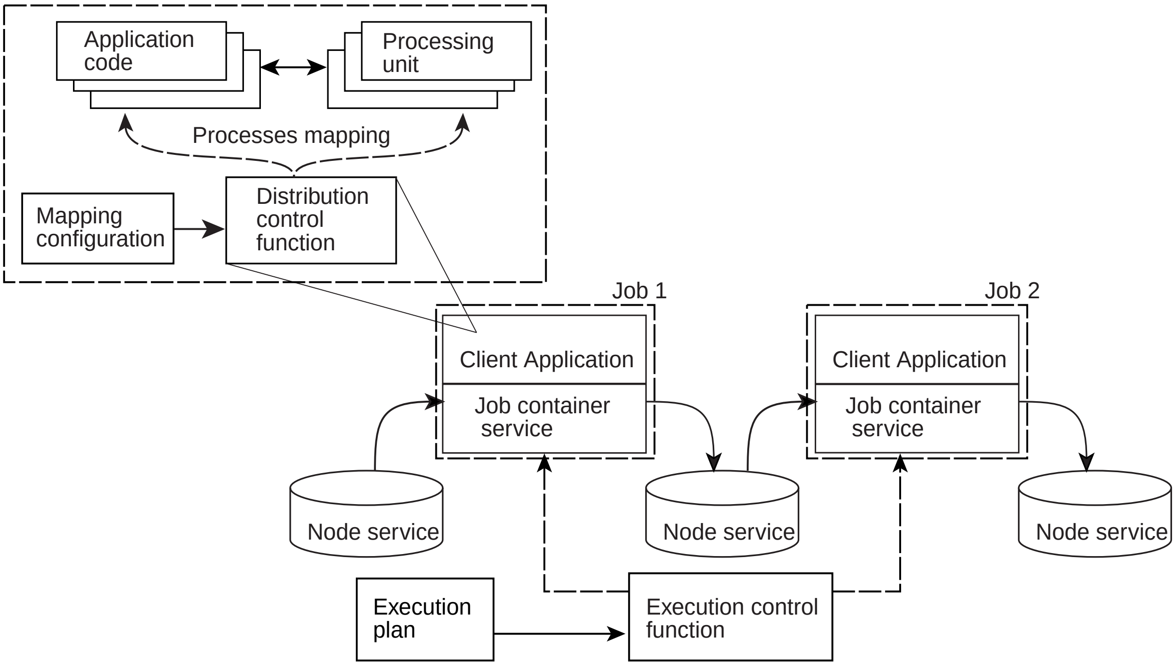

Fig. 6.1.2. IMGDIS job execution model and the services configuration. The process is abstracted as successive jobs by the "job container service" and the "node service" which works as a FIFO (first in first out) data buffer to connect the jobs. The client application is distributed to the computer cluster through the DCF in the case of requirements.

which executes Fourier transforms, the FFT application is copied to multiple FFT applications, and the copies are executed simultaneously on the computer cluster. On the other hand, for the job which executes the retrieval process, the DCF assigns parallel executable application codes to the computer cluster. Figure 6.1.2 shows the job execution model.

## 6.2 DATA ARCHIVING AND DISTRIBUTION

The IMGDIS produced several level products from level-0 (L0: raw sensor data called interferograms). Table 6.2.1 shows the IMG product definition.

| Product name | Definition |
|---|---|
| Level-0 (L0) | raw data received from the NASDA |
| Level-1 (L0A) | interferograms packed with the observation unit |
| Level-1B (L0B) | non-linearity compensated interferograms |
| Level-1A (L1A) | spectra represented by the complex number |
| Level-1B (L1B) | radiometrically calibrated spectra |
| Level-1C (L1C) | L1B with the cloud information |
| Level-1D (L1D) | L1C with the meteorological information |
| Level-2 (L2) | retrieved physical parameters |

Table 6.2.1. IMG product definition

The IMG L0 data were sent from NASDA/EOC to the IMG ground segment by D1M cassette tapes. ADEOS ground stations consist of NASDA/EOC and NASA stations, and some data delivery delay was anticipated. The delivery delay of IMG L0 data was estimated at 12 days by NASDA. But the actual delay in the data received at EOC was 10 to 18 days and that received at NASA stations was between 49 to 53 days. The IMG ground segment, IMG Data and Information System (IMGDIS), processed all the L0 data and produced the L1 and L2 products. As previously shown, the IMG observed deep space and a blackbody for calibration purposes after every six earth observations. The eight observations (110 seconds) are the smallest unit of the IMG products, and are referred to as a single unit. The volume of processed data was measured in terms of these units. We retrieved 46,088 units from the raw transmission data throughout the lifetime of the IMG; 10,642 units satisfied (at least one observation point in the unit) both defined screening conditions (the standard deviation of the alignment sensor output was smaller than 0.0001 degrees, and the maximum digital number of the interferogram was larger than 5,000) simultaneously, and 35,446 units did not satisfy the conditions.

### 6.2.1 DATA QUALITY CONTROL

The data quality was affected by various factors. The archived data set was classified using the two monitoring values of the instrument and one index derived from the L1 processing. The classified units were marked with three type of flags.

1) The first flag represents the interferogram peak value of the blackbody observation.

2) The second flag represents the alignment condition with the standard deviation of the alignment displacement. On the second flag, the unit has a “Good” flag whenever the blackbody and the deep space observation satisfy the flag criterion.

3) The third flag represents the phase differences derived from the Inverse Fourier Transformation of the interferograms per unit. The unit has a “Good” flag when all the phase spectra of the 6 observations satisfy the criterion.

Table 6.2.1.1 shows the summarized result for each classification. “GOOD” means both the interferograms and the alignment conditions are

Table 6.2.1.1. Archived and classified units number for each REQQ

| OPERATION | SYS | REQQ | | | | | | | | |
|---|---|---|---|---|---|---|---|---|---|---|
| | 1 | 1 | 2 | 3 | 4 | 5 | 6 | 7 | 8 | 9 | TOTAL |
| GOOD | 18 | 2 | 437 | 1255 | 1767 | 1132 | 3531 | 1467 | 104 | 929 | 10642 |
| ALIGN | 4 | 5 | 743 | 2247 | 1521 | 1569 | 3220 | 2522 | 55 | 562 | 12448 |
| NG | 234 | 9034 | 3014 | 1019 | 970 | 2491 | 1847 | 1148 | 2487 | 754 | 22928 |
| OTHER | 87 | 8687 | 1390 | 1495 | 1810 | 1019 | 2034 | 738 | 2964 | 666 | 20890 |
| OBSERVED | 343 | 17728 | 5584 | 6016 | 6068 | 6211 | 10632 | 5875 | 5610 | 2911 | 66978 |

good. "ALIGN" denotes those units that have good interferograms and one or more of the observation points satisfying the alignment condition (6 observation points comprise one unit). "OBSERVED" shows the number of units estimated from the time stamp on the raw data from NASDA. The third flag, "NG" indicates that the data have not satisfied the defined conditions.

"OTHER" refers to the estimated number of units that may have been lost in the process of converting the raw data to the L0 data set. It is thought that some valid units can be salvaged from the "OTHER" class.

### 6.2.2 DATA DISTRIBUTION

Following the memorandum between MITI and NASDA, the IMG data are presented to the world scientific community. The copies of the data sets processed by IMGDIS were sent back to NASDA, and all the users can access the IMG data through NASDA. Also, the ERSDAC expressed their wish to continue the WWW server operation for the IMG data after the completion of the IMG project. The public access URL is http://img.ersdac.or.jp, and the URL for researchers is http://img.ersdac.or.jp/forpi/ the access of which requires registration for the ERSDAC. The description of product format and sample programs for reading the products are also presented on the web pages.

## 7. RETRIEVAL PROCESS WITH THE FINAL VERSION

After the satellite failure, the MITI decided to close the IMG project at the end of the fiscal year 1999, and the IMGDIS operation was planned to terminate the job in September 1998. The final version of the retrieval process (version 3) adopted the iteration method and required a large calculation, however, the computational resources were limited and did not satisfy the requirements of this expanded process. We concluded the retrieval process of version 3, reducing the spectral data to produce better qualitative L2 products.

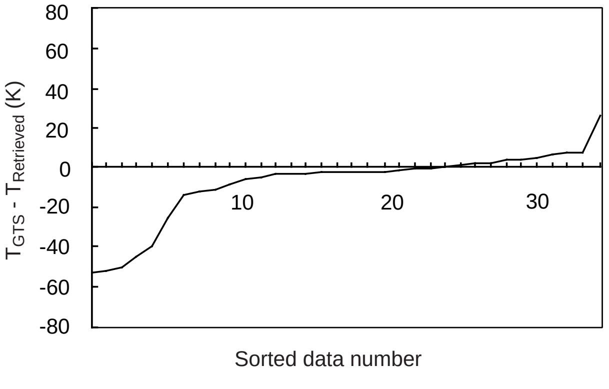

Fig. 7.1.1. Sorted difference between the surface temperature data obtained by the previous version and the in situ temperature data at 1000 hPa derived from the GTS for the REQQ-9 period.

### 7.1 SPECTRAL DATA SCREENING IN THE RETRIEVAL PROCESS

To reduce the number of spectral data for retrieval, first, we selected "GOOD" data as mentioned in Table 6.2.1.1 which satisfied the defined criterion for the interferogram peak size and the radiative calibration represented as the phase.

Second, we screened the data that were "bending" at the window region of the spectrum. The study for this phenomenon is not completed, however, some spectral data were bending and the bending spectra show the regional locality during global observation. We processed the spectral data that had less than 4 K in terms of window region temperature difference.

Third, we screened the data contaminated by clouds. Because the elimination method using OCTS did not work well, we introduced the screening method which compared the retrieved surface temperature prepared by the previous retrieval version with the JMA's objective analysis surface temperature at 1000 hPa. When a large difference exists between the two, we can consider that the observed datum is contaminated by the local clouds or was retrieved improperly. Because the JMA's data are produced by the three-dimensional numerical model through the initialization using worldwide in situ temperature/humidity data, we can consider that the lowest layer temperature values of the model are reflected in the in situ surface temperature averaged in time and space, and the local thick clouds in the view of the IMG represented as the discrepancy from the temperature of the objective analysis data. Figure 7.1.1 shows the difference between the surface temperature data obtained by the previous version and the in situ temperature data at 1000 hPa derived from the global telecommunication system (GTS) for the REQQ-9 period. There are particular areas where the two show large discrepancies. We adopted the criterion for temperature screening. When the difference between the surface temperature of the objective analysis and the temperature of the window region of the spectrum was within 15 K, the retrieval process proceeded.

Table 7.1.1 shows the result of this screening process. We processed 29416 data by the final retrieval version.

Table 7.1.1. Number of screened data and screening process.

| Process order | Screening process | Number of screened data | Number of the data after the screening |
|---|---|---|---|
| 1 | "GOOD" data | | 60330 |
| 2 | spectral "bending" at the window region | 11247 | 40393 |
| 3 | discrepancies from the objective analysis data | 5430 | 29146 |

## 7.2 EXAMPLES OF RETRIEVED PARAMETERS

The following figures are samples of the retrieval results using the final version of the algorithm (ver. 3.0). The raw data picked up for the sample were derived from a unit (Unit no.: 013579-10 observed 1, Date: 19970424 22:18:39, and Location: lat. 59.019 lon. 351.131).

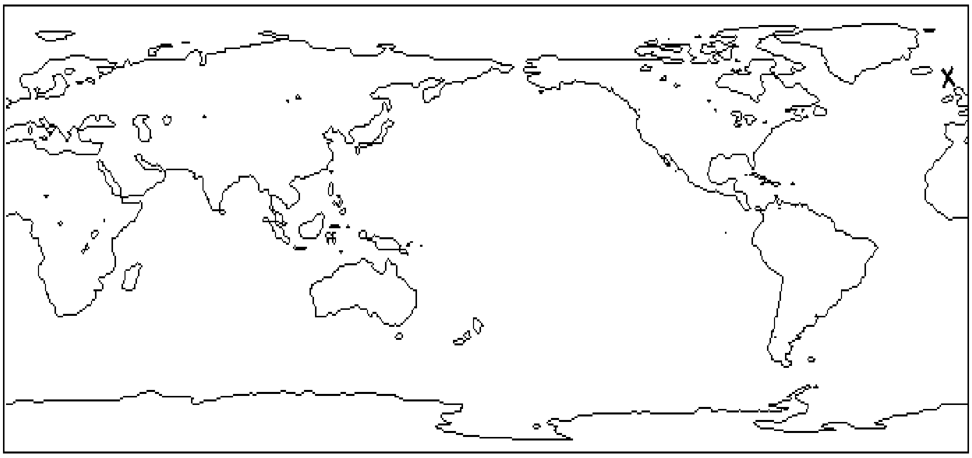

Fig. 7.2.1. Observed point (the cross point)

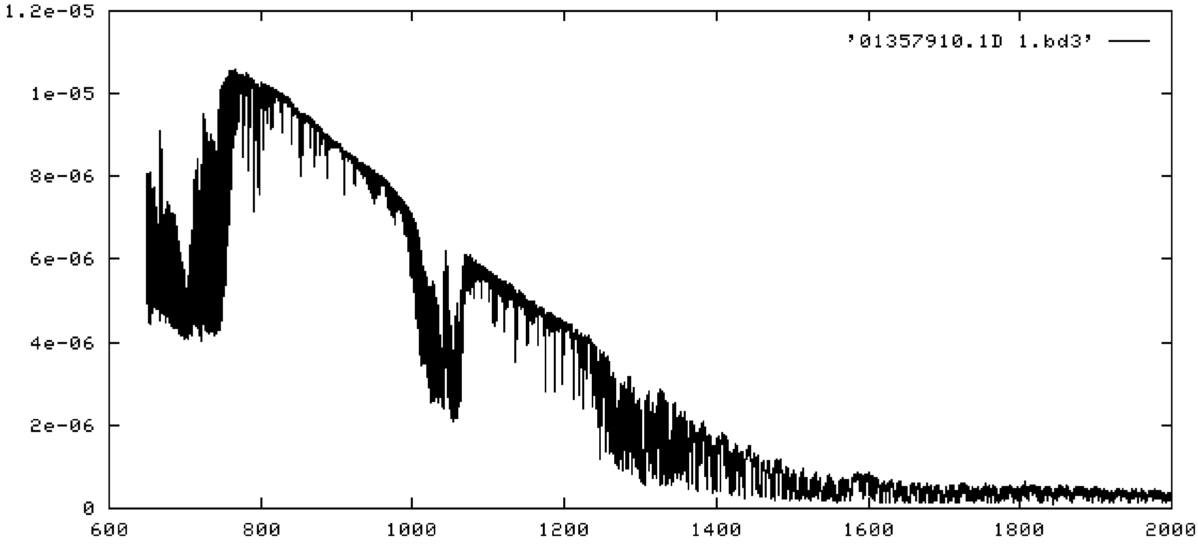

Fig. 7.2.2 Observed spectra

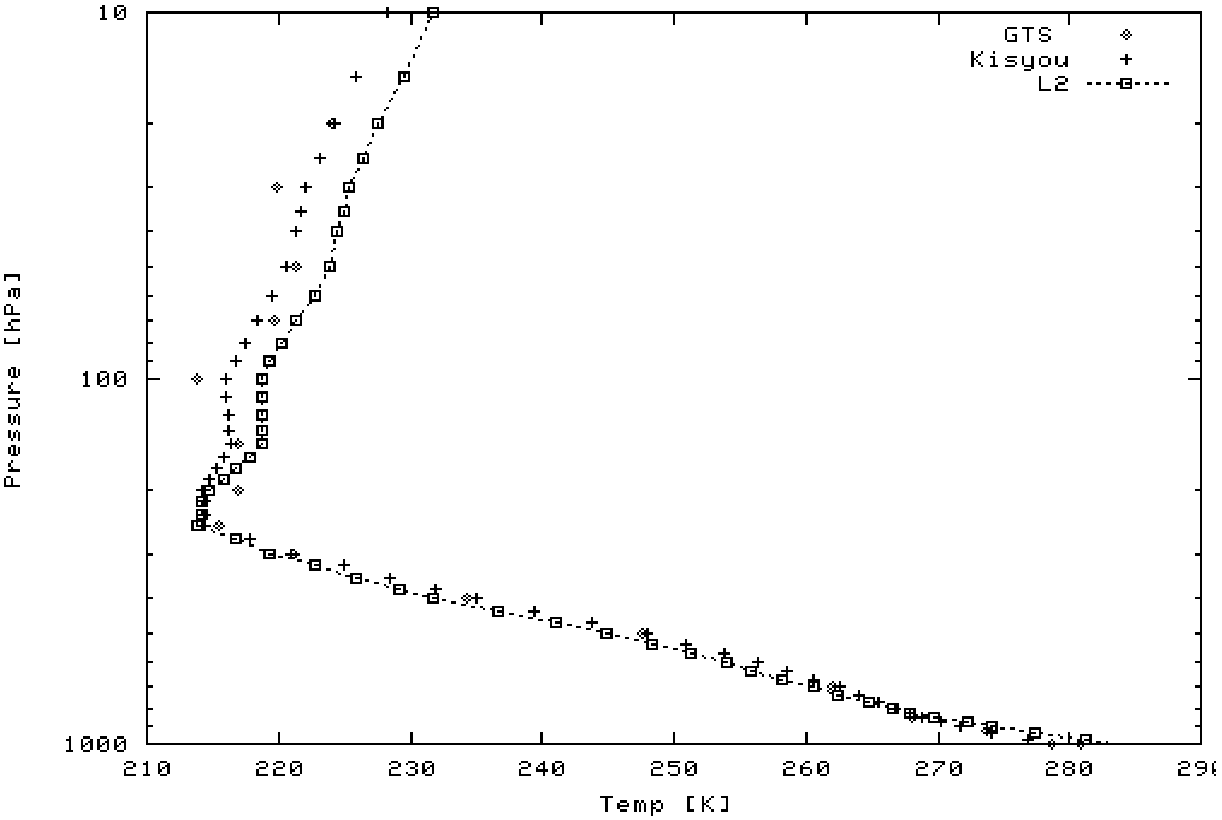

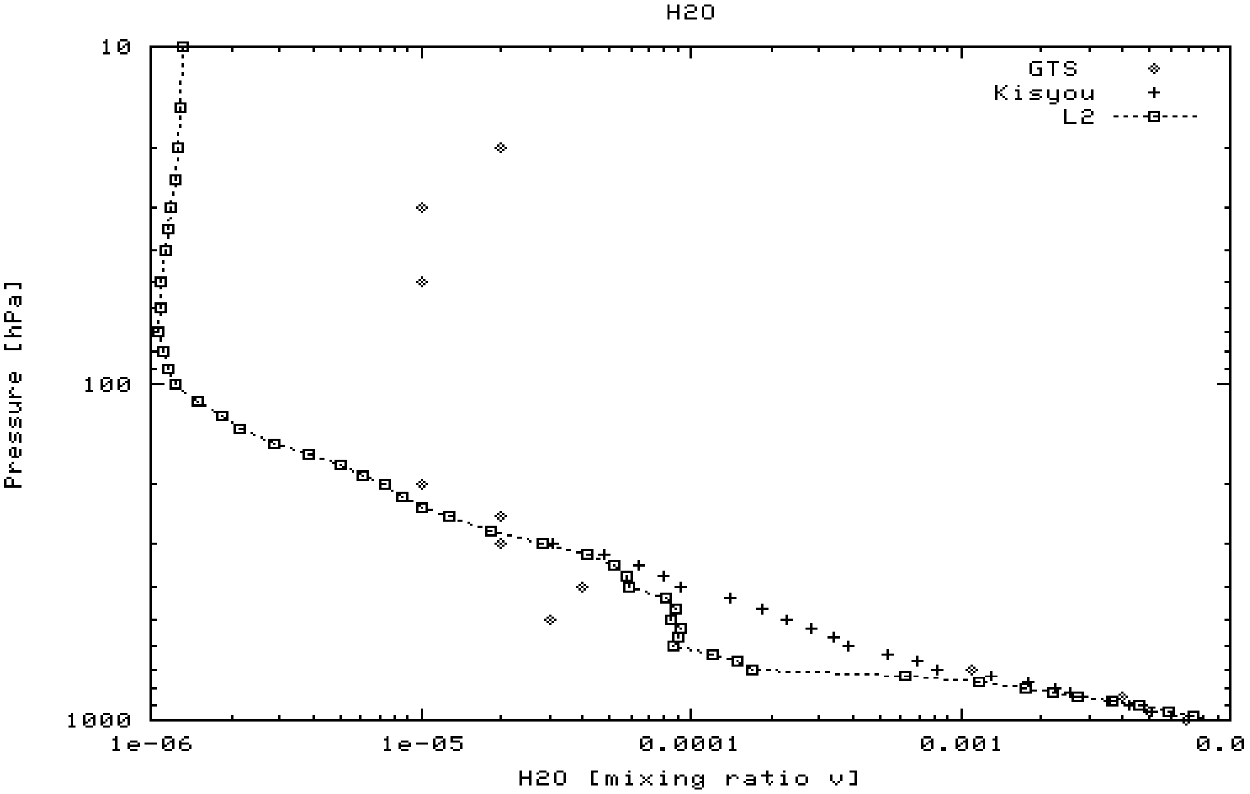

Fig. 7.2.3. Retrieved with algorithm ver. 3.0 (Temperature and $H_2O$). “Kisyou” means the initial profile, and “L2” express the retrieved profile. GTS radiosonde data were shown for comparison. The GTS data were within 3 hours and within 200 km from the IMG observation.

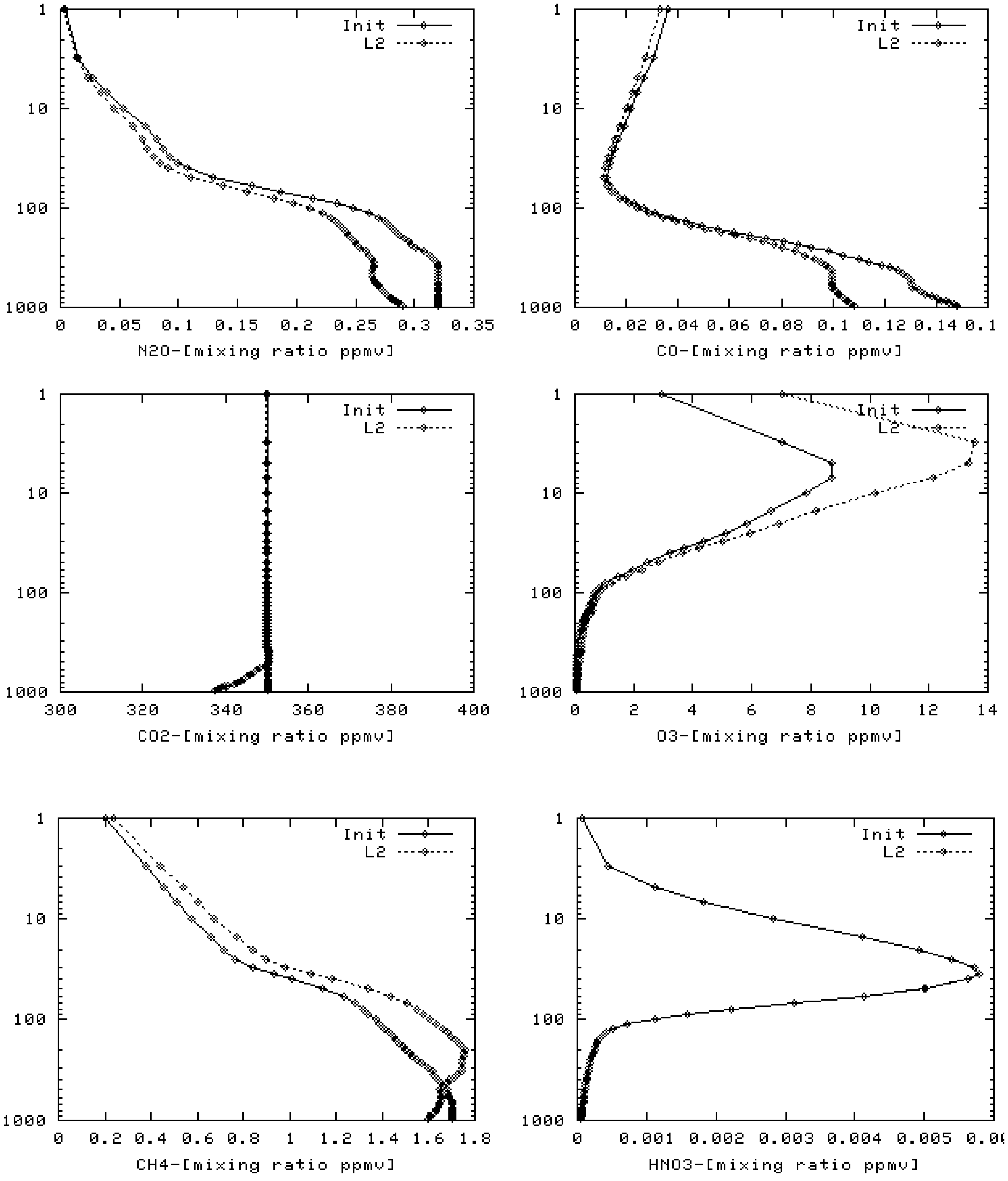

Fig. 7.2.4. Retrieved with algorithm ver.3.0 (Other trace gases). "Init" gives the initial profile, and "L2" expresses the retrieved profile.

# 8. PRELIMINARY EVALUATION OF THE RETRIEVED PARAMETERS

The IMG data processing in the IMGDIS was completed in September, 1998. The evaluation activity of standard products should be carried out by field campaign and/or statistical analysis of in situ data. As previously mentioned, the first campaign was obsolete because of the incident in the IMG instrument, and the second flight campaign planned for July 1997 was canceled by the abrupt cessation of ADEOS operation. Fortunately, some in situ measurements of the atmospheric constituents had been carried out, such as the Kiruna campaign performed by the Improved Limb Atmospheric Spectrometer (ILAS) science team , and, we can continue the evaluation activity, however, the IMGDIS operation has been terminated.

In the following sections, we first introduce the evaluation results of the retrieved temperature and humidity, and second we introduce the map of the greenhouse gases. Because the temperature/humidity and other atmospheric constituents were retrieved simultaneously, we can consider that the retrieval error of the constituents is comparable to that of temperature/humidity.

## 8.1 EVALUATION OF THE RETRIEVED TEMPERATURE AND HUMIDITY

Without in situ measurement, several evaluation methods can be adopted. It is possible to perform the evaluation of the products of L2 temperature and water vapor profiles indirectly, statistically comparing these values with GTS radiosonde data and buoy data. Because the temperature/water vapor profiles are retrieved simultaneously with other target gases, we can expect the retrieval process for gases to be reliable when the retrieved temperature/water vapor values are acceptable. Then, prior to the future validation of the L2 products, some preliminary evaluations are performed. In the following, we discuss the L2 retrieval by the version 3 program.

Through the entire the REQQ, 793 match-up data sets were built. The GTS data are within 3 hours and within 300 km from the IMG observation points. The mean time difference of the data sets was 781 seconds. Comparing the space difference of the data sets, the effect of the time difference was omitted. Next, data sets apparently contaminated by the cloud were screened out by applying the threshold of the temperature difference, -15 to 15 degrees, between GTS (1000 hPa) and L2 data (1013 hPa). We obtained 669 data sets, however, the cloud contamination on the L2 data may still be present, and the selection of a cloud free data set using OCTS picture data is planned. The pressure levels used for the analysis and the mean values of the GTS data are shown in Table 8.1.1.

The match-up data sets were binned by the distance between the L2 and GTS observation points. If there is relationship between the binned distance and the deviation of the match-up data sets, the deviation at a distance-0 point can be estimated. Figure 4 shows the temperature deviations for each pressure level. The figure shows the mean values of the deviation and the 1 and -1 standard deviation values as the error bar. The deviations were calculated as:

Deviation = (GTS temperature - L2 temperature)/ GTS temperature.

At the surface (1013 hPa), the averaged deviation value of the first binned data (distance of 0~100 km) is about 0.005. It means that the averaged difference of the temperature is 1.4 K. The value is slightly greater than the expected retrieval tolerance error ( <1 K ) previously shown in Table 4, however, recognizing the tendency that the relatively higher mean temperature values become small as they approach the 0-distance in Figure 8.1.1, the L2 surface temperature difference may become less than 1.4 degrees. At each pressure level, L2 temperature values are smaller than GTS values. Considering the screened data set ratio (0.84 =669/793), it is obvious that the dominant cause of the result is cloud contamination. We can apply a more accurate data set, screening the retrieved temperature data using higher threshold values.

Figure 8.1.2 shows the water vapor deviations. At the pressure level of 1013 hPa, the averaged value of the deviations for each binned distance is -0.24. This means that the averaged difference of the water vapor mixing ratio is 24 % in terms of the surface level. As shown in Table 4, we estimated the tolerance error to be 10 % for the water vapor. The lower

Table 8.1.1. Analyzed pressure levels and archived GTS mean values

| L2 pressure levels (hPa) | 1013 | 937 | 850 | 500 | 300 | 200 |
|---|---|---|---|---|---|---|
| GTS pressure levels (hPa) | surface | 925 | 850 | 500 | 300 | 200 |
| GTS mean temperature (K) | 280.3 | 271.8 | 269.7 | 248.6 | 224.7 | 216.9 |
| GTS mean water vapor (mixing ratio: ppmv) | 11160 | 6072 | 4623 | 788 | 144 | 92 |

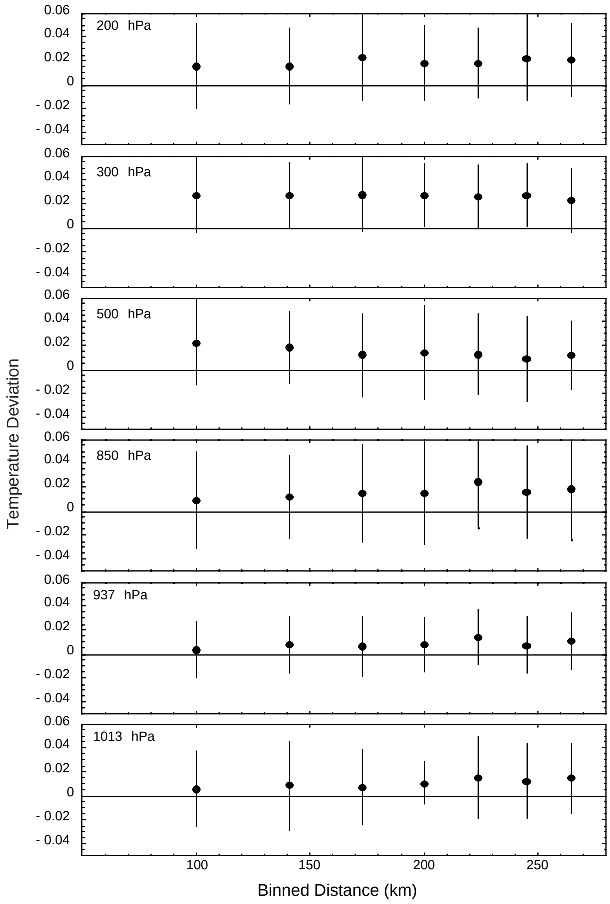

Fig. 8.1.1. Temperature deviations between Level 2 and GTS data

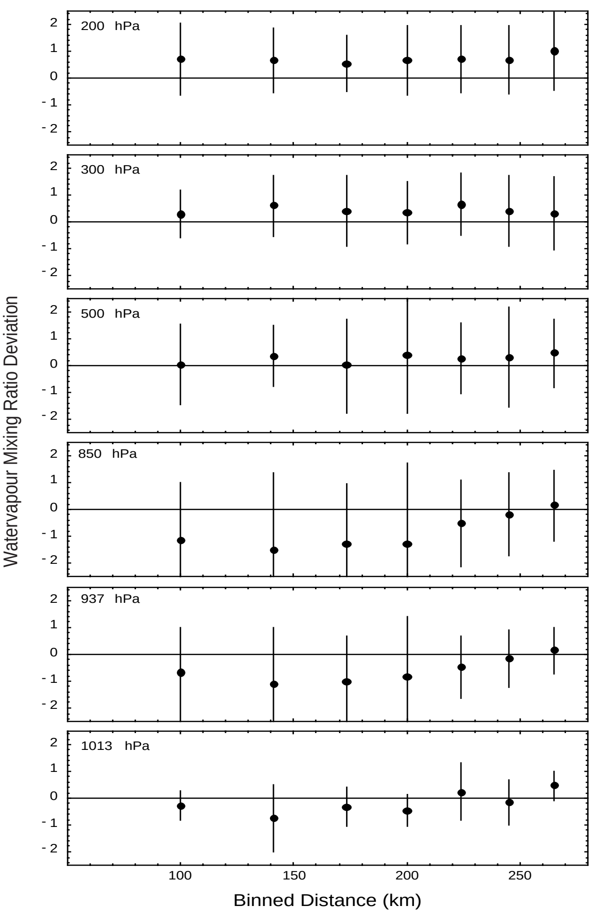

Fig. 8.1.2. Water vapor deviations between Level 2 and GTS data

accuracy may be caused by the cloud contamination as in the case of temperature retrieval, however, as the result of the 850 hPa shows the largest deviations, there are some discrepancies to be clarified by modifying retrieval algorithms.

The preliminary evaluation of temperature and water vapor using the GTS data showed that: (1) data screening is necessary and using surface temperature presented by the GTS or other source will be adequate, (2) water vapor retrieval accuracy does not satisfy the designed tolerance, however, there is a possibility of satisfying the requests applying higher screening thresholds, and (3) an enhancement of the current retrieval algorithm is required.

## 8.2 MAPPING OF GREENHOUSE GASES

It is difficult to evaluate the density of atmospheric constituent gases directly. However, there is a good prospect of obtaining density maps of global gases, which have never been pictured before. Figure 8.2.1 shows the $CH_4$ column density composite data map in the REQQ-3 and REQQ-4 period. The IMG performed observations for 8 days in each REQQ. Prior to making the map, the data sets were screened to ignore cloud contamination, and the daytime (descending orbits) map and the nighttime (ascending orbits) map were compared. There were significant differences between the daytime and nighttime temperature observation maps, but the $CH_4$ density daytime and nighttime maps did not show such significant differences. We can expect that the temperature profiles do not have a large effect on the $CH_4$ profiles, e.g., crosstalk of temperature on the $CH_4$ spectral channel may be negligibly small.

Figure 8.2.2 shows the $N_2O$ column density composite data map in REQQ-3 and REQQ-4. The lifetime of $N_2O$ is very long, over 100 years [1], therefore we can expect a smooth distribution of $N_2O$. From the figure, we can determine that the $N_2O$ column density is almost equal globally, and has a value equivalent to 0.11 mol/m$^2$ estimated from the U.S. standard model ($CH_4$ value is estimated to be 0.59 mol/m$^2$ ). From these results, the $N_2O$ distribution map produced is relatively flat, and we can consider that the $CH_4$ density map texture was

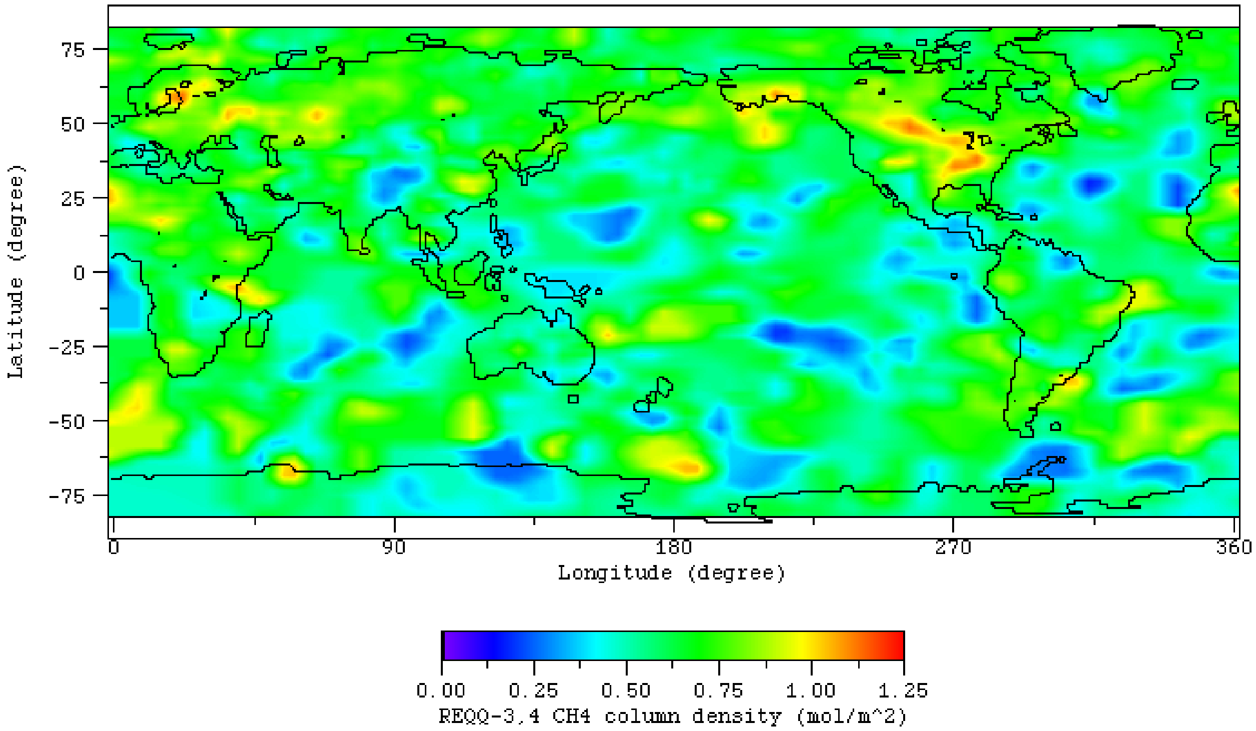

Fig. 8.2.1. CH$_4$ column density map obtained in REQQ-3 and REQQ-4.

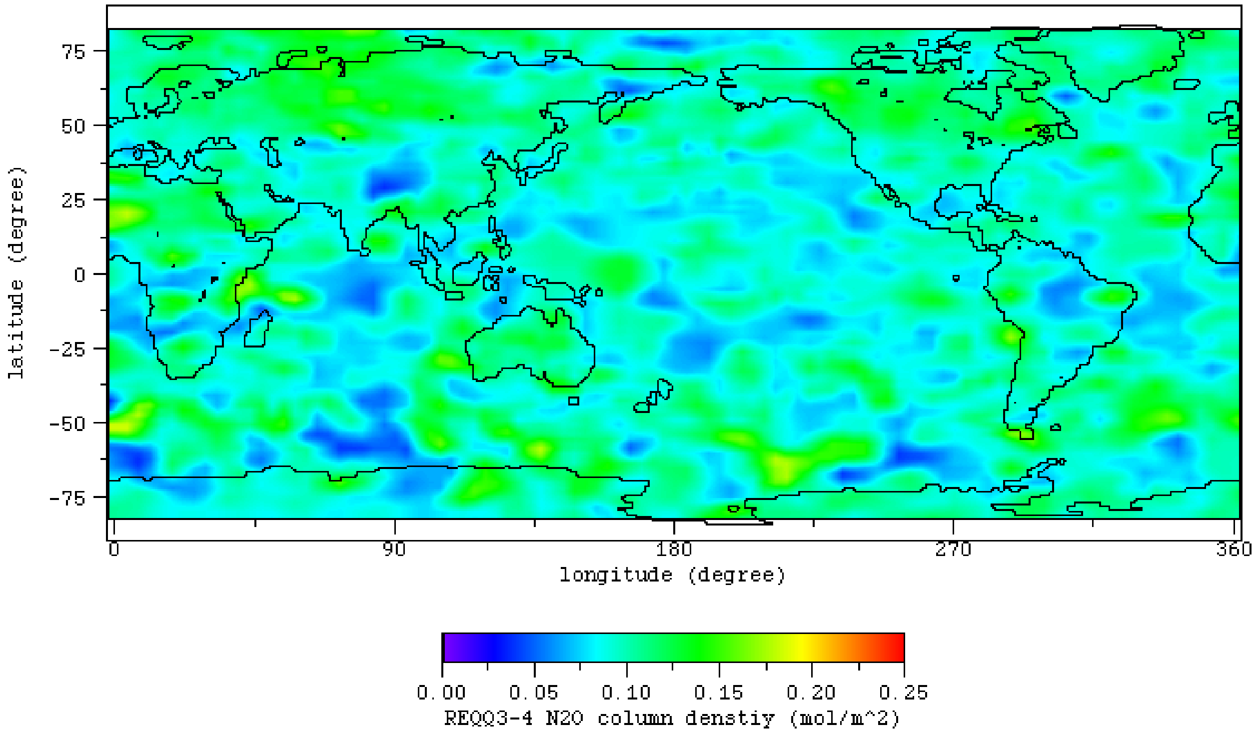

Fig. 8.2.2. N$_2$O column density map obtained in REQQ-3 and REQQ-4.

not produced by an error in retrieval procedures.

The mean $CH_4$ mixing ratio observed by flask sampling is nearly 1.7 ppmv [2], and this figure shows that the mixing ratio over ocean areas is equal to or less than that of the mean data. This tendency is similar to the cross section of latitude composed by ground-based sampling [3]. However, this shows a higher value in locations over the continents, in contrast to a very low density area over the Arctic Ocean.

## 8.3 DEVELOPMENT OF THE FOUR-DIMENSIONAL ASSIMILATION MODEL

The IMG observed the earth's surface successively along the orbit. The observation points mapped on the ground are dispersed over time and space. So, it cannot be said that the composite maps created from the original products, e.g. the methane map mentioned earlier, represent the general behavior of atmospheric constituents. We can analyze the constituent densities in terms of time and space using constructed snapshots from successive retrieved data. The gas density distribution shown in the global snapshot will support the evaluation of the L2 comparing archived data set of the surface station observations.

To obtain a snapshot of the constituents, a four-dimensional assimilation (FDDA) system was developed. The FDDA model is composed of the GHG concentration transport model and the data assimilation model. The threedimensional GHG concentration transport model adopted a semi-Lagrange scheme (SLS). The data assimilation model adopted the intermittent data assimilation cycle and optimal interpolated method (OIM) for interpolation from observation points to mesh points.

The numerical model using SLS allows large time steps without degrading the accuracy [1][2][3]. This advantage introduced the application of the SLS to a threedimensional advection equation [4][5][6]. The SLS calculation consists of a trajectory search and an interpolation. The wind field data, which was used for the present analysis, was at 6 hour intervals. Although SLS is unconditionally stable, we adopted a smaller time step Δt=15 minutes in order to search for the trajectory, because the tracers do not move beyond the grid scale with a typical jet stream, within this time step at mid latitude area.

The SLS has a problem of collapsing mass conservation. For very lengthy simulations, this causes an unacceptable loss of accuracy. In order to solve this problem, we applied a cubic spline for interpolation which has the function of suppressing numerical fluctuation [9]. Furthermore, we introduced the mechanism of restraining the fluctuation on the interpolating value at each grid point restricted to the value of eight neighbouring grid points as,

$$C = \mathrm{Max}(\ \mathrm{Min}(H, C_{MAX})\ ,\ C_{MIN}\ )\ ,$$

where $C_{MAX}$ and $C_{MIN}$ are respectively defined as the largest and smallest value of eight closest points surrounding the departure point.

Before applying the observation data to the assimilation model, some data checks are carried out to exclude unsuitable data for the model. First, checks are carried out for observation and alignment errors. These checks are previously accomplished in obtaining IMG L1 data. Next, gross checks are performed on physical reasonableness of the observed data. While obtaining L2 data, some data are screened by comparing with the retrieved surface temperature of IMG L2 product and lowest layer atmospheric temperature of the objective analysis data of JMA.

The developed FDDA system carries out another data screening which is the check with physical evaluation of IMG $N_2O$ observed data. It is well-known that for the concentration of atmospheric $N_2O$, the spatial distribution is almost universal, and it is not at any time in much transition [7]. So it is to be assumed that $N_2O$ concentration is almost equal globally, and the observed data where the $N_2O$ concentration is very different from the mean value can be excluded.

For IMG observed $N_2O$ concentration( $C_{N2O}$ ), the mean value over time and space( $\overline{C}_{N2O}$ ) is $3.08642\mathrm{x}10^{-7}$, and the standard deviation( $\tilde{C}_{N2O}$ ) is $6.24302\mathrm{x}10^{-8}$ (mixing ratio). The datum that did not satisfy the following expression was omitted.

$$|\ C_{N2O}\ -\ \overline{C}_{N2O}\ |\ <\ \tilde{C}_{N2O}\ /\ 2$$

The Optimal Interpolated Method (OIM) has been adopted for interpolation from observation points to grid points. OIM is the most effective model for data interpolation from observation points to mesh points. At each time step the covariance between physical parameters of observation point i, j is

$$m(i,j) = \exp(-(r(i,j)/r_{max})^2 - (t(i,j)/t_{max})^2\ ),$$

where $r_{max}$ and $t_{max}$ are defined by minimizing the weight function which is given to each observation increment in the analysis at gridpoint.

With the IMG observed L2 products and the objective analysis data, we carry out the FDDA calculation. The term of the calculations is 7.5 months which is the same period of ADEOS operation. Before calculating, FDDA initial distributions of GHG have to be set. In this calculation, we assume the concentration has distribution gained by IMG L2 data. Next, we set some calculation parameters. The essential parameters are the correlation parameters on distance and time. These parameters are closely related to the weight function in statistical interpolation. Some studies were carried out on the correlation distance $r_{max}$ from 0 km to 600 km (supposition by jet-current at convection sphere).

Figure 8.3.1, shows the calculation results for 7.5 months in the case of $r_{max}$=400 km, and the correlation time of 3.0 hours (supposition by a

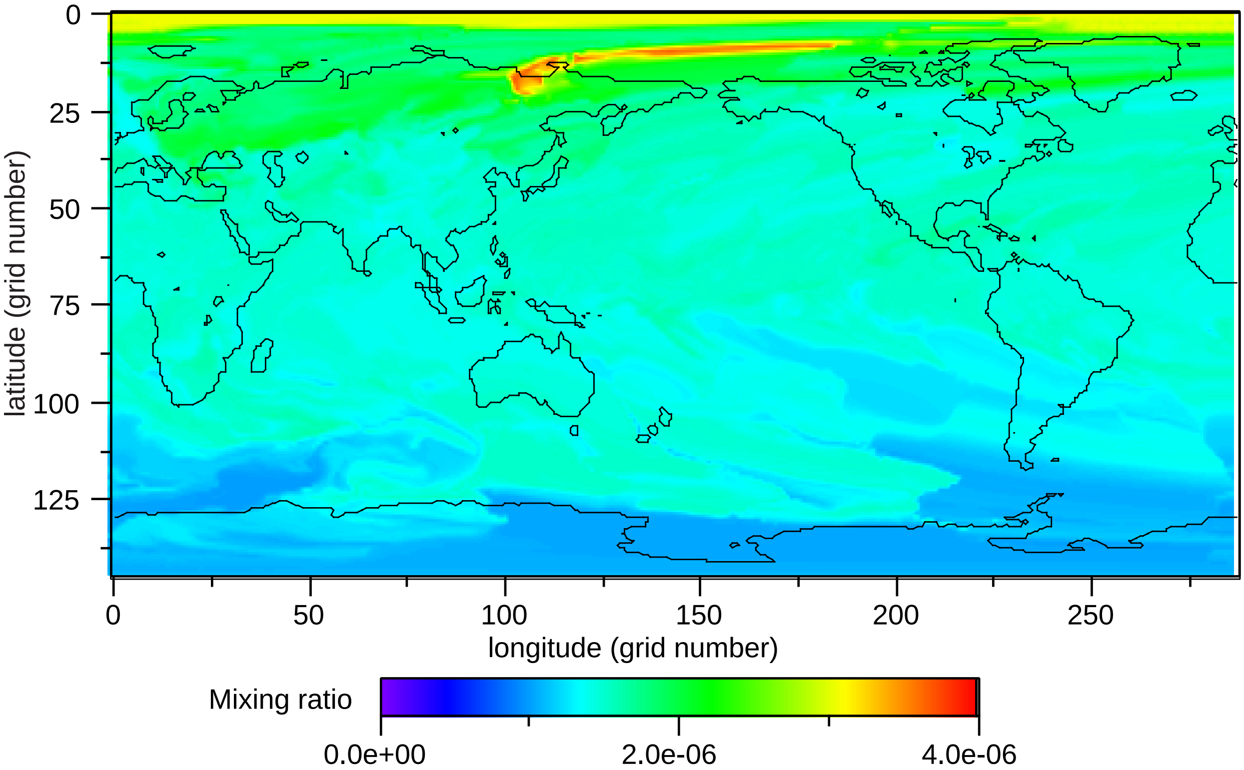

Figure 8.3.1. $CH_4$ mixing ratio snapshot (at 1000 hPa) for 7.5 months

calculation time step $\Delta t = 6.0$ hours). The zonal-mean profiles of $CH_4$ after 7.5 months calculation period is shown in Fig. 8.3.2. The concentration in the southern hemisphere tends to be larger than in the northern hemisphere. Seasonal change cannot be considered because the ADEOS was operated only for 8 months.

Figure 8.3.2 shows the zonal profiles of the data plotted in Figure 8.3.1. It shows that the methane density of the northern hemisphere tends to be greater than that of the southern hemisphere. This tendency agrees with the well-known distributions obtained from the surface global observations and supports the validity of the L2 retrieval algorithm, however, further evaluation of the density values of the L2 should be carried out.

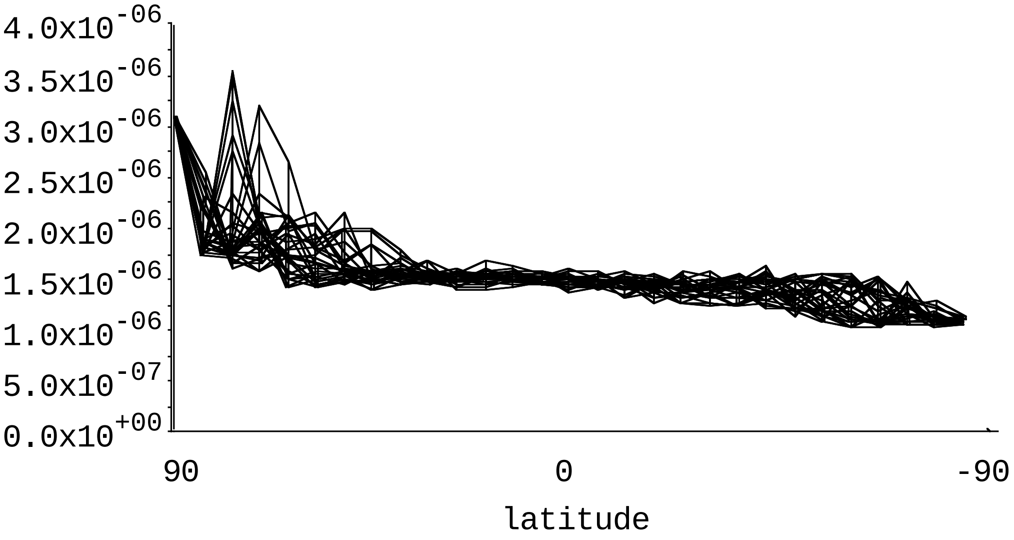

Fig. 8.3.2. Zonal profiles of $CH_4$ . The multiple plot lines are drawn using the longitudinal grid data presented in Fig. 8.3.1.

## 9. CONCLUSION

Using the IMG, we can measure the earth's radiation budget, the surface temperature and atmospheric temperature profiles, and the atmospheric constituents. The operation of the IMG established the validity of the high-resolution, high-throughput interferometer in space. We obtained global maps of the atmospheric constituents, and the results were very impressive. The atmospheric thermal radiation spectra obtained by the IMG show a good correspondence with the anticipated spectra calculated using the atmospheric optical model.

It was highly regrettable that the ADEOS satellite incident interrupted the first comprehensive earth observation from space. Although the IMG operation was unexpectedly aborted due to this incident, it definitely proved that satellite borne FTIR can monitor global greenhouse gases.

The Atmospheric Radiation Spectrometer (ATRAS), which is an IMG follow-on, is now proposed to the NASDA as a candidate sensor for the future earth observation satellites from the science team experienced in the IMG project. The ATRAS project inherits not only technical achievements but also the experiences of the scientific/operational activities. The ATRAS sensor will provide substantial information for atmospheric sciences.

## ACKNOWLEDGEMENT

The IMG project was supported by MITI, Japan. The successful results of the project were obtained with the cooperation of NASDA, JAROS, and TOSHIBA, the IMG committee member scientists, and many other principal investigators of the IMG around the world. We are grateful for the efforts of all our colleagues.

# LIST OF THE RESULTS USING THE IMG DATA

(1) H. Kobayashi, T. Ogawa, H. Shimoda, A. Shimota and S. Kadokura, "The First View of the Global Map of Greenhouse Gases by the Interferometric Monitor for Greenhouse Gases (IMG)," Geocarto International, 12, 4, 1997.

Abstract — The interferometric monitor for greenhouse gases (IMG), was the precursor for the high resolution FTIR boarded on the satellite for Earth observation. The IMG sensor was able to obtain only 8 months of radiation spectra, however, the retrieved greenhouse gases maps have certified that the high resolution spectrometer is very effective tool for the atmospheric science.

(2) H. Kobayashi, "IMG program report," The Third ADEOS Symposium in Sendai on January 26~30, 1998.

Abstract — IMG, Interferometric Monitor for Greenhouse gases, was the precursor of the high resolution FTIR boarded on the satellite for the Earth observation. The IMG sensor operated only 8 months, however, obtained high resolution thermal infrared spectra gave us plentiful information on the global atmospheric phenomenon, and certified that the high resolution spectrometer is a crucial tool for resolving the global warming problem. The IMG presented the first global maps of greenhouse gases retrieved from the spectra.

(3) R. Imasu, "Temperature, Water Vapor, and Minor Constituents as Observed by Interferometric Monitor for Greenhouse gases (IMG) aboard Advanced Earth Observing Satellite (ADEOS)", The third ADEOS Symposium in Sendai, Jan. 27, 1998.

Abstract — Interferometric Monitor for Greenhouse gases (IMG) is a Fourier Transform Spectrometer (FTS) which had been developed for measuring greenhouse gases in the atmosphere, particularly in the troposphere. It had been operated for about 7 months from November 1996 to the end of June 1997. During the operational period IMG had measured over 23000 terrestrial thermal emission spectra of which the signal to nose ratio is sufficient for retrieving atmospheric parameters such as temperature and gas concentrations. As most of the data had been obtained during a few days in each REQQ period which had been performed about two times a month, we obtained about 15 global data sets of the IMG data. The most interesting feature observed in the stratosphere is the relationship between temperature and ozone concentration in the northern hemispheric spring over the arctic region. Water vapor concentration up to the lower stratosphere have also been analyzed. Preliminary analysis for other constituents such as methane shows the latitudinal gradient in concentration in the troposphere. However, cloud contamination is still the most serious problem in retrieving temperature and gas concentrations in the troposphere. We have attempted to improve the cloud screening and correction method such as slicing method by customizing the statistical data used as a priori data or by using OCTS data as the cloud information source in the IMG's instantaneous field of view.

(4) J. Wang, J. Gille, and H. Saji, "Upper Troposphere Water Vapor and Climate Variabilities in the Equatorial Pacific: A Study Using ADEOS/IMG Observations," Water Vapor in the Troposphere and Stratosphere session, Spring AGU, May, 1998.

Abstract — Water vapor is one of the most important greenhouse gases in the atmosphere. Upper troposphere water vapor contributes significantly to the radiative balance of the upper troposphere region and the variability of outgoing longwave radiation. Due to the lack of global measurements with adequate accuracy and resolution, there is still considerable controversy on the roles of water vapor in climate change (e.g. positive feedback versus negative feedback). Recent studies have shown that high resolution interferometer observations from satellite can be used as diagnostic tools for water vapor and climate variability studies. Since its launch on 17 August 1996, the ADEOS/IMG instrument has provided unprecedented high resolution (0.05 - 0.1 $cm^{-1}$) observations of the atmosphere despite the failure of the ADEOS satellite in July 1997. In this paper, we will first present comparisons of ADEOS/IMG observations in the equatorial Pacific with line-by-line model calculations to demonstrate the quality of IMG spectral radiance data. Then the IMG high resolution observations will be used to study the variability of upper troposphere water vapor and its connections to sea surface temperature and outgoing longwave radiation.

(5) R. Imasu, T. Ogawa, and H. Shimoda, "Meridional Distribution Feature of Minor Constituents as Observed by IMG Sensor Aboard ADEOS Satellite," COSPAR 32nd Scientific Assembly in Nagoya on Jul. 13, 1998.

Abstract — Interferometric Monitor for Greenhouse gases (IMG) sensor aboard the Advanced Earth Observing Satellite (ADEOS) is a Fourier Transform type infrared spectrometer (FT-IR) which had been developed aiming to measure the greenhouse gases in the atmosphere, particularly in the troposphere. It was operated for about 7 months from November 1996 up to the end of the life time of the ADEOS on June 1997, and measured over 138000 terrestrial thermal emission spectra which are available for the retrieval analysis. A cloud detection and correction method based on the analysis of the initially retrieved temperature profiles were presented. Using the cloud correction method, meridional distributions of temperature and minor constituents were preliminarily analyzed.

(6) C. Clerbaux, P. Chazette, J. Hadji-Lazaro, G. Megie, J.-F. Muller, and S.A. Clough, "Remote sensing of CO, $CH_4$, and O3 using a spaceborne nadir-viewing interferometer," JGR, 103, D15, 18,999-19,013, August 20, 1998.

Abstract — Within the next 5 years, several instruments launched on polar orbiting satellites will provide high-resolution infrared remote-sensing measurements of CO, $CH_4$, and O3 on a global scale. The upwelling spectral radiances to be recorded by a nadir-looking remote sensor have been simulated using a high-resolution radiative code (line-by-line radiative transfer model (LBLRTM)) coupled to a three-dimensional chemical transport model (intermediate model of the annual and global evolution of species (IMAGES)). The instrumental specifications of the Fourier transform interferometric monitor for greenhouse gases/ Advanced Earth Observing System (IMG/ADEOS) and infrared atmospheric sounding interferometer (IASI/METOP) were used to generate realistic data. Calculations have been performed to assess the sensitivity of the nadir spectral radiances to changes in the gas concentration, temperature profile and to instrumental characteristics. We provide spectral intervals for an efficient retrieval of these species, together with a set of climatological tropospheric standard mixing ration profiles.

(7) A. Shimota, S. Kadokura, H. Kobayashi, The retrieval for the atmospheric concentration of $CH_4$ from the interferometric monitor for greenhouse gases (IMG), 9th CACGP & 5th IGAC, Seattle in USA on Aug. 20-25, 1998.

Abstract — The interferometric monitor for greenhouse gases (IMG) was the precursor for the high resolution FTIR boarded on the ADEOS satellite for the earth observation. The IMG was developed to obtain detailed spectra of thermal infrared radiation from the earth's surface and from the atmosphere. High resolution spectra from the IMG have information on the atmospheric concentration of greenhouse gases, water vapor and also a temperature profile. Unfortunately, ADEOS stopped its operation on June, 1997, so that the IMG sensor was able to obtain the radiation spectra during only 8 months. The IMG radiation spectra were evaluated by the simulated spectra using a line-by-line atmospheric radiative transfer model, FASCODE version 3. There was good agreement between the observed and calculated spectra. Furthermore, the $CH_4$ mixing ratio was tried to retrieve from the radiation spectra observed by IMG. The inclination of the retrieved mixing ratio along latitude was similar to the one from the ground-based sampling.

(8) U. Amato, D. DeCanditiis, I. De Feis, C. Serio and H. Kobayashi, "The CHIARA inversion algorithm for IMG," IGARSS'98 in USA, 1998.

Abstract — The Interferometric Monitor for Greenhouse gases (IMG) sensor is a high resolution Fourier Transform spectrometers which has flown on the ADEOS platform. IMG was developed by Ministry of International Trade Industry (MITI) and it has been the first very high spectral resolution (apodized resolution of 0.1 cm^-1) spectrometers to fly in space to sense temperature and gas constituent profiles through the earth infrared emission spectrum. IMG is mostly intended for water vapor and greenhouse gases mapping on global and regional scale. IMG is the most demanding instrument on board of ADEOS and is posing new and challenging problems in the area of remote sensing of geophysical parameters from infrared radiances. No consolidated and validated methodology exists at present which exploits all potential information contained in IMG spectra. The main aim of this paper is to present the inversion algorithm we have developed for IMG and discuss preliminary results obtained by inverting IMG spectra. The Convolution of High-Resolution Interferograms and Advanced Retrieval in the Atmosphere (CHIARA) we have developed is a complete tool which allows us: 1) to generate synthetic IMG radiances and to invert IMG spectra for temperature profile and the main greenhouse gases (profiles or global amount). The main features of CHIARA are 1) - fast computation of IMG synthetic radiances; 2) - analytical computation of Jacobian for temperature and any gases; 3) - an inversion algorithm which relies on Tikhonov regularization with a second derivative smoothing constraint. Unlike statistical regularization and conventional mathematical regularization, CHIARA is capable to optimally control the size and direction of the iteration step. This is achieved through the so-called L-curve criterion. The result is a very fast convergent inversion algorithm capable of finding an optimal (in the Least Square sense) solution even at the first step of iteration. Application of CHIARA to both simulated and real IMG spectra will be presented and discussed.

(9) H. Kobayashi, "IMG: precursor of the high-resolution FTIR on the satellite," International Symposium on Remote Sensing of the Atmosphere, Environment, and Space in Beijing on Sep. 14-17 1998.

Abstract — IMG, Interferometric Monitor for Greenhouse gases, was the precursor of the high resolution FTIR boarded on the satellite for the Earth observation. The IMG sensor operated only 8 months, however, obtained high resolution thermal infrared spectra gave us plentiful information on the global atmospheric phenomenon, and certified that the high resolution spectrometer is a crucial tool for resolving the global warming problem. The IMG presented the first global maps of greenhouse gases retrieved from the spectra. Standard products of IMG processed by the ground segment are defined as Level-1 and Level-2 products. Level-1 products are spectra radiometrically calibrated using the IMG on board black body and deep-space radiation. Defined Level-2 products retrieved from Level-1 are Temperature profile (including SST), $H_2O$ profile, $CO_2$ profile, $CH_4$ profile, $N_2O$ profile, CO profile, total Ozone, and total $HNO_3$. Standard products of the IMG require to be evaluated. The radiometric characteristics and stability of measurement were evaluated using mission data and housekeeping data of the IMG. Comparing with the theoretically calculated results, the wave number resolution and the accuracy were evaluated. The global maps for the atmospheric constituents shown the significant results on the gases global distribution. The evaluation of the Level-2 products using in situ temperature/humidity data were carried out. To obtain the snap shot and to study the global behavior of the constituents, four dimensional assimilation system was developed.

(10) R. Imasu, T. Ogawa, and H. Shimoda, "Latitudinal distribution of methane as observed by IMG sensor aboard ADEOS satellite," International Symposium on Remote Sensing of the Atmosphere, Environment, and Space in Beijing on Sep. 15, 1998.

Abstract — Interferometric Monitor for Greenhouse gases (IMG) aboard Advanced Earth Observing Satellite (ADEOS) is a Fourier Transform type spectrometer (FT-IR) which had been developed for measuring greenhouse gases in the atmosphere, particularly in the troposphere. It had been operated for about 7 months from November 1996 up to the end of the life time of the ADEOS on June 1997. During the operational period IMG had measured over 138000 terrestrial thermal emission spectra of which the signal to nose ratio is sufficient for retrieving atmospheric parameters such as temperature and gas concentrations. As most of the data had been obtained during the 4-days operational period which had been scheduled twice in each system request period (REQQ), we have obtained about 15 global data sets of the IMG data during the whole IMG operational period. A cloud detection and correction method which was based on the analysis of the initially retrieved temperature profiles were presented. Using the cloud correction method, latitudinal distribution of methane was preliminarily analyzed and an example of the results was shown.

(11) J. Wang, J.C. Gille, and H. Saji, "Analysis of Spectral Radiance Measurements by IMG on ADEOS," Optical Remote Sensing of the Atmosphere and Clouds conference to be held in Beijing, China, Sept. 14-17, 1998.

Abstract — The Interferometric Monitor for Greenhouse Gases (IMG) uses Fourier transform spectrometry to measure the top of the atmosphere spectral radiance between 3.3 =B5m and 14 =B5m in 3 separate bands (Ogawa et al. 1994). It was launched on board the Japanese ADEOS satellite launched in August, 1996, and has an unapodized spectral resolution of 0.07 $cm^{-1}$. In this paper, the results of intercomparisons between IMG observations over different geographical regions with radiative transfer model calculations will be presented and discussed first. Good agreement between measurement and line-by-line model calculation allows further analysis of IMG high resolution spectral radiance with confidence. IMG observations over the equatorial Pacific and Atlantic oceans are used to study the variability of tropospheric water vapor and connections to sea surface temperature and outgoing longwave radiation.

(12) A. Shimota, S. Kadokura, and H. Kobayashi, "The evaluation of the IMG Level-2 products using the GTS data," ASSFTS8 in Toulouse on Nov. 16, 1998.

Abstract — IMG, Interferometric Monitor for Greenhouse gases, was the precursor of the high resolution FTIR boarded on the satellite for the Earth observation. The IMG sensor operated only 8 months, however, obtained high resolution thermal infrared spectra gave us plentiful information on the global atmospheric phenomenon, and certified that the high resolution spectrometer is a crucial tool for resolving the global warming problem. Standard products of IMG processed by the ground segment are defined as Level-1 and Level-2 products. Level-1 products are spectra radiometrically calibrated using the IMG on board black body and deep-space radiation. Defined Level-2 products retrieved from Level-1 are Temperature profile (including SST), water vapor profile, and gases profiles. Standard products of the IMG require to be evaluated. Comparing with the theoretically calculated results, the wave number resolution and the accuracy were evaluated. The evaluation of the Level-2 products using the Global Telecommunication System (GTS) data were carried out.

(13) R. Imasu, "Global distribution feature of methane and carbon monoxide as observed by ADEOS/IMG sensor," ASSFTS8 in Toulouse on Nov. 16, 1998.

Abstract — Interferometric Monitor for Greenhouse gases (IMG) is a Fourier Transform Spectrometer (FTS) which has been developed for measuring greenhouse gases in the atmosphere, particularly in the troposphere. It was operated for about 7 months from November 1996 to the end of June 1997. During the operational period IMG measured over 23000 terrestrial thermal emission spectra of which the signal to nose ratio was sufficient for retrieving atmospheric parameters such as temperature and gas concentrations. The most serious problem in measuring tropospheric gases using an infrared spectrometer is the cloud contamination. We used a cloud detection and correction (screening) method which was based on the analysis of the initially retrieved temperature profiles for retrieving temperature and gas profiles. Preliminary results on global distribution of methane and carbon monoxide were obtained using the cloud detection method. However the results were seemed to be contaminated with clouds even after the cloud correction (screening) process particularly in the polar regions. We need more effective cloud detection method using visible and near-infrared imagery that was simultaneously obtained with IMG data such as those from OCTS (Ocean Color and Temperature Scanner) for raising the accuracy of the retrieval.

(14) K.G. Gribanov, V.I. Zakharov, S.A. Tashkun, and V.G. Tyuterev, "A New Generation User - Friendly Software for Infrared Atmospheric Remote Sensing from Space," ASSFTS8 Workshop at Meteo France in Toulouse, 16-18 November, 1998.

Abstract — FIRE-ARMS ( Fine Infrared Explorer for Atmospheric Radiation Measurements ), a new user-friendly software system for atmospheric calculations has been recently created. This software includes forward simulation of atmospheric spectra, weighting function analysis and retrieval algorithm based on nonlinear least squares method using the spectroscopic line parameters available in standard databases such as HITRAN, GEISA or other experimental/theoretical spectroscopic compilations . The models and algorithms built in this software were examined with IR spectra with resolution of approximately 0.1 $cm^{-1}$ observed from space in the 600-2000 $cm^{-1}$ spectral region by IMG on board of ADEOS mission during first half of 1997. Weighting function analysis allows the user to select optimal set of spectral intervals for accurate temperature and gases profiles retrieval. Temperature and $H_2O$ profiles retrieved from IMG band 3 spectra in the range of 680-1400 $cm^{-1}$ are presented. The retrieved profiles are weakly dependent on reference profiles chosen. The accurate retrieval of the temperature profile allows to evaluate the cloud conditions and top level of clouds. Using FIRE-ARMS software we identified 12C16O18O,$13CO_2$ and HDO signals in IMG spectra. The application of FIRE-ARMS for creative processing of IMG/ADEOS data and in future space missions such as IASI etc. is discussed.

(15) H. Shimoda and T. Ogawa, "Characterization of IMG," ASSFTS8 Workshop at Meteo France in Toulouse, 16-18 November, 1998.

Abstract — A satellite borne FTS called IMG (Interferometric Monitor for Greenhouse Gases) was developed by JAROS (Japan Resources Observation System Organization) deputed by MITI (Ministry of International Trade and Industry). It was installed on ADEOS (Advanced Earth Observing Satellite) which was launched on Aug. 1966 by NASDA (National Space Development Agency of Japan). IMG is a very high spectral resolution (0.1 $cm^{-1}$) spectrometer that covers a wide range of infrared spectrum (3.3 - 14 $\mu$m). With these features, IMG is able to detect and monitor spatial and vertical distribution of greenhouse gases such as $CO_2$, $CH_4$, $O_3$, etc. as well as to measure vertical profile of temperature and water vapor over the entire Earth. Unfortunately, ADEOS stopped its operation on 30, June 1997, but about 8 months of data have been collected. IMG sensor characteristics obtained after launch showed almost the same characteristics obtained in the pre-launch tests except radiometric stability and absolute wavelength. Initial validation results for temperature and water vapor show good agreement with *in-situ* measurements and objective analysis data.

(16) A.M. Lubrano, F.Romano, C. Serio, and H. Kobayashi, "Recent CHIARA results for the inversion of clear-sky IMG spectra," ASSFTS8 Workshop at Meteo France in Toulouse, 16-18 November, 1998.

Abstract — Earth's infrared spectra observed by the Interferometric Monitor for Greenhouse gases sounder have been used to retrieve temperature, water vapour and ozone profiles. It is shown that the sounder allows us to simultaneously retrieve stable solutions for temperature and water vapour and ozone. Comparison with GTS data is provided for temperature and water vapor. Total ozone derived from IMG has been compared to ADEOS TOMS retrieval and fairly good agreement has been found. Comparison among calculated and observed radiances shows good agreement in several parts of the thermal band, which is sensed by the sounder. A slight discrepancy is observed in the wing region of the 720 $cm^{-1}$ $CO_2$ Q-branch, whereas the most severe form of disagreement is seen in the 6.7-micron vibrational $H_2O$ absorption band. Nevertheless, suitable spectral ranges may be identified which yield accurate and stable inversions for temperature, water vapour and ozone.

(17) S. Payan, C. Camy-Peyret, and P. Jeseck, "IMG instrument spectral response function and retrieval of CO and OCS," ASSFTS8 Workshop at Meteo France in Toulouse, 16-18 November, 1998.

Abstract — Earth's nadir-viewing infrared emission spectra recorded by the Interferometric Monitor for Greenhouse gases sounder (IMG) have been used to retrieve the vertical column amounts of CO and OCS. The LPMA retrieval algorithm includes of an accurate radiative transfer model and an efficient minimization algorithm. A global fit method is used, allowing simultaneous retrieval of the column amounts of more than 8 species, ground temperature, ground emissivity, and providing a tool to derive the instrument spectral response function (ISRF) from IMG spectra. The ISRF used is a parametric function involving the usual sinc function together with a Lorenzian-Gaussian function shifted from the peak of the sing in order to model a possible asymmetry. The corresponding parameters can be adjusted simultaneously with the other geophysical parameters. In addition, a possible wavenumber shift of the IMG spectra is taken into account in the parametric instrument spectral response function. The derived ISRF will be presented together with results on the retrieved CO and OCS column amounts.

(18) C. Clerbaux, J. Hadji-Lazaro, S. Payan, C.C. Peyret, nad J. Wang, "Intercomparison of inversion algorithms for the retrieval of CO from IMG/IASI spectra," ASSFTS8 Workshop at Meteo France in Toulouse, 16-18 November, 1998.

Abstract — Within the next 5 years, several nadir-looking instruments launched on polar orbiting satellites will provide tropospheric measurements of trace gases on the global scale (IMG, MOPITT, SCIAMCHY, AIRS, IASI, TES). In order to prepare these missions, fast forward radiative codes nad efficient algorithms for the retrieval of trace gases from measured nadir radiances are under development. This paper aims to compare three different inversion algorithms (global fit/IASI, Digital Gas Correlation/MOPITT and Neural Network/IASI) that will be used for the retrieval of CO from atmospheric spectra. We will discuss the results obtained using a set of simulated spectra and compare the CO columns as retrieved from selected spectra recorded by the IMG/ADEOS instrument. This study highlight the need for complementary information (temperature, emissivity, instrumental function and cloud content) to retrieve accurate CO vertical columns.

(19) V.P. Walde, H.E. Revercomb, and D.C. Tobin, "Calibration and validataion studies using IMG data," ASSFTS8 Workshop at Meteo France in Toulouse, 16-18 November, 1998.

Abstract — Data from the Interferometric Monitor of Greehouse gases (IMG) are valuable for studying earth's energy balance and for trace gas retrieval studies. A calibration procedure is presented here that properly accounts for phase ambiguities between individual measurements within a calibration sequence. Examples of IMG data validation are presented from comparisons with the High-resolution Interferometer Sounder (HIS) during the Winter Cloud Experiment (WINCE) in February 1997 and with ling-by-line radiative transfer calculations using data from Pt. Barrow, Alaska as input. Data from the HIS are presented from the Arctic Loud Experiment in May/June of 1998 to illustrate the potential usefulness of analyzing interferometric data over the Arctic.

(20) A. Shimota H. Kobayashi,and S. Kadokura, “Radiometric calibration for the airborne IMG simulator,” Appl. Optics, 38, 571-576, 1999.

Abstract — The earth observation satellite ADEOS launched in 1996 summer is carrying a space borne high-resolution FTIR, IMG. IMG has realized 0.1 cm$^{-1}$ high spectral resolution purposing to retrieve greenhouse gases profile map of the earth. To fulfill the requirements from the retrieval algorithms for greenhouse gases profile, atmospheric emission spectra must be calibrated better than 1 K accuracy. Prior to the launch ADEOS/IMG, we developed airborne simulator named Tropospheric Infrared Interferometric Sounder (TIIS). TIIS was equipped with ambient temperature and LN$_2$ cooled blackbodies for radiometric calibration. Double-side optical path difference scanning was adopted taking into consideration of a phase correction. The calibration for measured radiance from ice cooled blackbody, which the magnitude spectra calculated from a complex Fourier transformation were used, revealed large errors in brightness temperature. These errors seems to cause by abnormal phase response in background emission. Therefore we needed to apply a method which deal with complex spectra in the process of calibration. In case of applying this method, sampling points sampled at a same optical path difference on each interferogram have to be decided. Unfortunately TIIS was not equipped with any function like a white light to identify the optical path difference. In this paper we showed the method to decide the positions of interferograms for complex Fourier transformation using retained phase term on calibrated spectrum. The spectra obtained from IMG not only TIIS were well calibrated with this algorithm.

(21) J. Wang, J.C. Gille, P.L. Bailey, L. Pan, and D. Edwards, “Retrieval of Tropospheric Carbon Monoxide Profiles from High-Resolution Interferometer Observations: A New Digital Gas Correlation (DGC) Method and Applications,” J. Atmos. Sci, 56, 219-232, 1999.

Abstract — Global tropospheric monoxide (CO) distributions can be retrieved from observations by spaceborne gas correlation radiometers and high-resolution interferometers. The Measurement of Pollution in the Troposphere (MOPITT) is a gas correlation radiometer designed for tropospheric CO and CH$_4$ remote sensing. It is being developed at the University of Toronto and the National Center for Atmospheric Research for launch on the EOS/AM-1 platform in 1999. Spaceborne high-resolution interferometers with troposphere CO remote sensing capability include the interferometric Monitor for Greenhouse gases(IMG) instrument and the Troposphere Emission Spectrometer (TES). IMG was developed by the Ministry of International Trade and Industry (MITI) of Japan. It was on the ADEOS-1 spacecraft launched in October 1996. TES is being developed by the Jet Propulsion Laboratory for launch on the EOS/CHEM-1 platform in 2002. For the purpose of testing the MOPITT data processing algorithm before launch, a new digital gas correlation (DGC) method was developed. This DGC method also allows the retrieval of global troposphere CO from MOPITT, IMG, and TES observations with a consistent algorithm. The retrieved CO profiles can be intercompared, and a consistent long time series of tropospheric CO measurements can be created. In this paper, the DGC method is described. The procedures for using the DGC method to retrieve atmospheric trace species profiles are discussed. As an example, CO profiles from IMG observations have been retrieved with the DGC method as a demonstration of its feasibility and application in MOPITT retrieval algorithm validation.

(22) H. Kobayashi, A. Shimota, C. Yoshigahara, I. Yoshida, Y. Uehara, K. Kondo, “Satellite Borne High Resolution FTIR for Lower Atmosphere Sounding and Its Evaluation,” IEEE Trans. Geos. Remote Sensing, 1999, in print.

Abstract — IMG, Interferometric Monitor for Greenhouse gases, was the precursor of the high-resolution FTIR boarded on the satellite for the Earth observation. The IMG sensor operated for only 8 months, however, the high-resolution thermal infrared spectra obtained gave us plentiful information on global atmospheric phenomena, and demonstrated that the high resolution spectrometer is a crucial tool for resolving the global warming problem. The IMG enabled the first global maps of greenhouse gases retrieved from the spectra.

# REFERENCES

## SECTION 2. BEGINNING OF THE IMG PROJECT

(1) T. Ogawa, "The way of the IMG," Kikai-Shinko, 25, 9, 42-49, 1992 (in Japanese).

(2) T. Ogawa, H. Shimod, M. Hayashi, R. Imasu, A. Ono, S. Nishinomiya, and H. Kobayashi, "IMG, interferometric measuremetn of greenhouse gases from space," Adv. Space Res., 14, 1, 25-28, 1994.

(3). W.L. Smith, H.M. Woolf, and H.E. Revercomb, "Linear simultaneous solution for temperature and absorbing constituents profiles from radiance spectra," Appl. Opt. 30, 1117-1123, 1991.

(4) G. Wetzel, H. Fischer, and H. Oelhaf, "Remote sensing of trace gases in the midinfrared spectral region from a nadir view," Appl. Opt. 34, 467-479,1995.

(5) C. Clerbaux, P .Chazette, J. Hadji-Lazaro, G. Megie, J.-F. Muller, and S. A. Clough, "Remote sensing of CO, $CH_4$, and O3 using a spaceborne nadir-viewing interferometer," JGR, 103D, 18999-19103, 1998.

(6) G.P. Anderson and J. H. Chetwynd,"FASCOD3P User Guide ", U.S. Air Force Philips Laboratory, Hansom Air Force Base, MA., 1992.

## SECTION 4. SPECTRAL CALIBRATION ALGORITHM

(1) S.H.S. Wilson, N.C. Atkinson, P.J. Rayer, j. Smith, and D.R. Pick, "ARIES-A Simulator for the Next Generation of Spaceborne IR Meteorological Sounders", Proc. of IEEE-IGARSS'97, Singapore, August 3-8, 1997.

(2) A. Shimota, H. Kobayashi, and S. Kadokura, "Radiometric calibration for the airborne IMG simulator," Appl. Optics, 38, 571-576, 1999.

(3) C. Weddigen, C. Eesge, and M. Hopfner, "Phase correction for the emission sounder MIPAS-FT," Appl. Opt., 32, 4586-4589, 1993.

(4) P.R. Griffiths and J. A. de Haseth, Fourier transform infrared spectrometry, John Wiley & Sons, Inc., New York, pp48-54, 1986.

(5) J. Schreiber, T. Blumenstock and H. Fischer, "Effects of the self-emission of an IR Fourier-transform spectrometer on measured absorption spectra," Appl. Opt.,35, 6203-6209, 1996.

(6) H.E. Revercomb, H. Buijs, H.B. Howell, D.D. Laporte, W.L. Smith, and L.A. Sromovsky, "Radiometric calibration of IR Fourier transform spectrometers: solution to a problem with the High-Resolution Interferometer Sounder," Appl. Opt. 27, 3210-3218, 1988.

## SECTION 5. RETRIEVAL ALGORITHM OF THE PHYSICAL PARAMETERS

(1) S. Twomey, "Comparison of Constrained Linear Inversion and Iterative Nonlinear Algorithm Applied to the Indirect Estimation of Particle Size Distributions," J. Computational Physics 18, 188-200, 1975

(2) C.D. Rodgers, "Retrieval of Atmospheric Temperature and Composition From Remote Measurements of Thermal Radiation," Rev. Geophysics and Space Physics, 14, 609-624, 1976.

(3) C.D, Rodgers, "The Vertical Resolution of Remotely Sounded Temperature Profiles with a priori Statistics," J. Atmos. Sci., 33, .4, 1976

(4) A. Chedine, N.A. Scott, C. Wahihe, P. Moulinier, "The Improved Initialization Inversion method: a high resolution physical method for temperature retievals from th TIROS-N series," J. Clim. Appl. Meteor., 24, 128-148, 1985.

(5) A.H.L. Huang, "An Analysis of the Characteristics of Atmospheric Profiles obtainedwith the High-resolution Interferometer Sounder (HIS)," a doctorial thesis, University of Wisconsin-Madison, 1989.

(6) W. Menke, "Geophysical Data Analysis: Discrete Inverse Theory revised edition," Academic Press, Inc. 1989

(7) W.L. Smith, H.M. Woolf, and H.E. Revercomb, "Linear simultaneous solution for temperature and absorbing consistent from radiance spectra," Appl. Opt., 30, 9, 1991

(8) L.S. Rothman, et al , "The HITRAN Molecular Database: Editions of 1991 and 1992," JQSRT, 48, 469-507, 1992

(9) F. Cheruy, N.A. Scott, J. Escobar and A. Chedin, "Retrieval of Temperature and water vapor profiles from high spectral resolution data in the infrared : Methodology Developed at LMD," 8th. symposium on Meteorological Observations and Instrumentation , Special Session on Water Vapor and Ultraviolet Measurements, 1993

(10) Jinxue Wang, Gail P. Anderson, Henry E. Revercomb, and Robert O. Knuteson, "Validation of FASCOD3 and MODTRAN3: comparison of model calculations with ground-based and airborne interferometer observations under clear-sky conditions," Appl. Opt., 35, 6028-6040, 1996

(11) S.A. Clough, C.P. Rinsland, P.D. Brown, "Retrieval of tropospheric ozone from simulations of nadir spectral radiances as observed from space," JGR, 100, 16579-16593, 1995

## SECTION 5.4. CLOUD DETECTION USING OCTS

(1) M. Tanaka and T. Nakajima, "Effects of oceanic turbidity and index of refraction of hydrosols on the flux of solar radiation in the atmosphere-ocean system," JQSRT, 18, 93-111, 1977.

(2) T. Nakajima and M. Tanaka, "Effect of wind-generated waves on the transfer of solar radiation in the atmosphere-ocean system," JQSRT, 29, 521-537, 1983.

(3) R.W. Saunders, "An automated scheme for the removal of cloud contamination from AVHRR radiance over western Europe," Int. J. Remote Sensing,7,867-886, 1986.

(4) T. Nakajima and M. Tanaka, "Matrix formulations for the transfer of solar radiation in a plane-parallel scattering atmosphere," JQSRT, 35, 13-21, 1986.

(5) R.W. Saunders and K.T.Kriebel, "An improved method for detecting clear sky and cloudy radiances from AVHRR data," Int. J. Remote Sens., 9,123-150, 1987.

(6) T. Nakajima and M. Tanaka, "Algorithms for radiative intensity calculations in moderately thick atmospheres using a truncation approximation," JQSRT, 40, 51-69, 1988.

(7) R.W. Saunders and K.T. Kriebel, "An improved method for detecting clear sky and cloudy radiances from AVHRR data," Int. J. Remote Sensing, 9, 123-150,1988.

(8) V. Thiermann and E. RUPRECHT, "A method for the detection of clouds using AVHRR infrared observations.International Jornal of Remote Sensing,"13,1829-1841,1992.

(9) T. Nakajima and M. D. King, "Asymptotic theory for optically thick layers: Application to the discrete ordinates method," Appl. Opt., 31, 7669-7683, 1992.

(10) M. Derrien, B. Farki, L. Harang, H. Legleau, and A. Noyalet, "Automatic cloud Detection applied to NOAA-11/AVHRR imagery," Remote Sens. Environ., 46, 246-267,1993.

(11) S.C. Ou, K.N. Liou, W.M. Gooch, and Y. Takano, "Remote sensing of cirrus cloud parameters using advanced very-high-resolution radiometer 3.7-and10.9-um channels," Appl. Opt., 32, 12, 2171-2180, 1993.

(12) A. Ruggaber, R. Dlugi, and T. Nakajima, "Modelling of radiation quantities and photolysis frequencies in

the troposphere," Accepted by J. of Atmos. Chem, 1994.

(13) J.D. Spinhirne and T. Nakajima, "The glory of clouds in the near infrared,"Accepted by Applied. Optics, 1994.

(14) G.B. Franca, and A.P. Cracknell, "A simple cloud masking approach using NOAA AVHRR daytime data for toropipcal areas," Int. J. Remote Sensing,16,9,1697-1705,1995.

## SECTION 8. PRELIMINARY EVALUATION OF THE RETRIEVED PARAMETERS

(1) A.F. Bouwman, K.W. Van der Hoeck, and J.G.J. Oliver, "Uncertainties in the global source distribution of nitrous oxide," JGR, 100, 1785-2800, 1995.

(2) J. A. Lakeman, IPCC Climate Change 1994, Radiative Forcing of Climate Change. Working Group I. Summary from Policymakers. Intergovernmental Panel on Climate Change, Cambridge, 13-49, 1995.

(3) E.J. Dlugokencky, L. P. Steele, P.M. Lang, and K.A. Masarie, "The growth rate and distribution of atmospheric $CH_4$," JGR, 99, 17021-17403, 1994.

## SECTION 8.3 DEVELOPMENT OF THE FOUR-DIMENSIONAL ASSIMILATION MODEL

(1) S. Staniforth, and J.Cote, "Semi-Lagranngian Integration Schemes for Atmospheric Models-A Review," American Meterol.Soc., 2, 2206-2223, 1991.

(2) S. Gravel, and A. Staniforth, "A Mass-Conserving Semi-Lagrangian Scheme for the Shallow-Water Equations.," Mon. Wea. Rev., 122, 243-248, 1994.

(3) A. McDonald, "A semi-Lagrangian and semi-Implicit Two Time-Level Integration Scheme.," Mon. Wea. Rev., 114, 824-830, 1986.

(4) S. Taguchi, "Inter-hemispheric exchange in the troposphere by an atmospheric transport model based on Observed winds," J.Meterol.Soc.Jpn, 71,123-135, 1993.

(5) S. Taguchi, and J. Taylor, "A simulation of methane and methyl chloroform using the NIRE global three-dimensional tracer transport model," JMS Proceedings for Sendai meeting, 1994

(6) K. Yamazaki, and M.Chiba, "A 3-D global simulation of the advective transport of passive tracers from various northern hemisphere sources," Tellus, 45B, 160-178, 1993

(7) A.F. Bouwman, K.W.Van der Hoeck, and J.G.J.Oliver, "Uncertainties in the global source distribution of nitrous oxige," JGR, 100, 1785-2800, 1995.

(8) L.P. Steele, et al., "The Global Distribution of Methane in the Troposphere," J. Atmos. Chem., 5, 125-171, 1987.

(9) Y.Uehara, H.Kobayashi, "Development of the GHG transport model based on a semi-Lagrange scheme with cubic spline interpolation," J.Met.Soc.Japan, submitted.